UNIVERSITÀ DEGLI STUDI DI CAGLIARI

Facoltà di Scienze Matematiche, Fisiche e Naturali

Dipartimento di Fisica

Ph. D. Thesis

A triple-GEM detector for the muon system of the LHCb experiment

Davide Pinci

Advisors:
Prof. Biagio Saitta

Dr. Alessandro Cardini

XV Ciclo (1999-2002)

Following the ancient tradition,
people take refuge in the Triple Gem.
(Anguttara Nikaya XI.12)

Contents

Chapter 1

The B physics at LHC

The exploration of physics with b flavoured hadrons offers a very fertile testing ground for the Standard Model (SM) description of electroweak interactions. One of the key problems to be studied is the phenomenon of CP violation which was first discovered in 1964 by Christenson et al. in the neutral kaon system [1].

Of particular interest is the study of rare b decays induced by the flavour changing neutral current transition $b \to s, d$ which are loop suppressed in the SM and thus very sensitive to new-physics effects.

During the past few years, B physics has received a great deal of attention, both from theorists and experimentalists, and data are being accumulated at several B factories (BaBar at SLAC and BELLE at KEK). Although the physics potential of these experiments is very promising, it may be that the "definite" answer in the search for new physics in B decays will be given by the LHC experiments ATLAS, CMS and particularly LHCb.

1.1 CP violation and CKM matrix

The violation of the CP symmetry is one of the most interesting aspects and unsolved mysteries of modern particle physics. Studies on this subject are particularly exciting, as they may open a window to physics beyond the SM. There are many different ways to explore CP violation, for instance through the study of certain rare decays of K mesons. However, for testing the SM description of CP violation in a quantitative way, the B system appears to be most promising [2, 3].

1.1.1 The SM description of CP violation

Within the framework of the SM, CP violation is closely related to the Cabibbo-Kobayashi-Maskawa matrix [4, 5], connecting the electroweak eigenstates (d', s', b') of the *down*, *strange* and *bottom* quarks with their mass eigenstates (d, s, b) through the following unitary tranformation:

$$\begin{pmatrix} d' \\ s' \\ b' \end{pmatrix} = \begin{pmatrix} V_{ud} & V_{us} & V_{ub} \\ V_{cd} & V_{cs} & V_{cb} \\ V_{td} & V_{ts} & V_{tb} \end{pmatrix} \cdot \begin{pmatrix} d \\ s \\ b \end{pmatrix} \equiv V_{CKM} \cdot \begin{pmatrix} d \\ s \\ b \end{pmatrix} \tag{1.1}$$

The elements of the CKM matrix describe charged-current couplings, as can be easily seen by expressing the non-leptonic charged-current interaction Lagrangian in terms of electroweak eigenstates:

$$L_{int}^{CC} = -\frac{g}{\sqrt{2}} (\bar{u}_l, \bar{c}_l, \bar{t}_l) \gamma^\mu \; V_{CKM} \begin{pmatrix} d \\ s \\ b \end{pmatrix} W_\mu^+ + h.c. \tag{1.2}$$

In the case of three generations, three generalized Cabibbo-type angles [4] and a single *complex phase* [5] are needed in order to parametrize the CKM matrix. This complex phase allows to accommodate CP violation in the SM. Among various parametrizations, the most convenient is the one proposed by Wolfenstein [6], which corresponds to a phenomenological expansion up to the third order of the small quantity $\lambda \equiv |V_{us}| = \sin \theta_C \simeq 0.22$ where θ_C is the Cabibbo angle:

$$\begin{pmatrix} 1 - \lambda^2/2 & \lambda & A\lambda^3(\rho + i\eta) \\ -\lambda & 1 - \lambda^2/2 & A\lambda^2 \\ A\lambda^3(1 - \rho - i\eta) & -A\lambda^2 & 1 \end{pmatrix} \tag{1.3}$$

Higher order terms can be taken into account systematically for particular applications.

1.2 The unitarity triangles of the CKM matrix

To test the SM picture of the violation of CP, the *unitarity triangles* derived from the unitarity of the CKM mixing matrix are typically used. The relation $V_{CKM}^+ \cdot V_{CKM} = 1$ leads to a set of twelve equations, consisting of six

normalization and six orthogonality relations. The latter can be represented as six triangles in the complex plane, all having the same area [7]. However, in only two of them all sides are of comparable magnitude $\mathcal{O}(\lambda^3)$, while in the remaining, one side is suppressed relatively to the others by $\mathcal{O}(\lambda^2)$ or $\mathcal{O}(\lambda^4)$. The orthogonality relations describing the triangles with sides of comparable length, are:

$$V_{ud}V_{ub}^* + V_{cd}V_{cb}^* + V_{td}V_{tb}^* = 0 \tag{1.4}$$

$$V_{ud}V_{td}^* + V_{us}V_{ts}^* + V_{ub}V_{tb}^* = 0 \tag{1.5}$$

As it can easily seen from the CKM matrix in equation (1.3), these two triangles are identical up to order $\mathcal{O}(\lambda^3)$. In the LHC era, the high experimental accuracy achievable will allow to distinguish between the two triangles (as illustrated in Fig. 1.1) and for this reason the higer orders have to be taken into account.

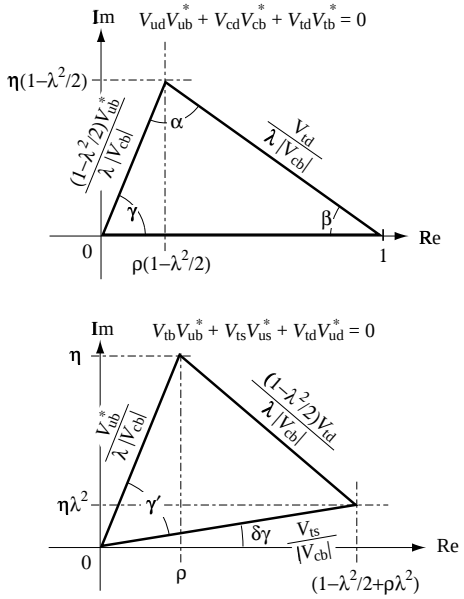

Figure 1.1: Two unitarity triangles in the Wolfenstein parametrization with up to the order $\mathcal{O}(\lambda^5)$.

The physics of bottom hadrons will provide a wide possibility to study and measure the parameters of the unitarity triangles. The angles can be extracted either indirectly by measuring the lengths of the sides, or, within the Standard Model, directly from CP asymmetries. If the angles extracted by two different methods disagree, this would be an indication of new physics.

1.3 General formalism for B physics

Given a neutral B^0 meson (which can be $B_d^0 \equiv \bar{b}d$ or $B_s^0 \equiv \bar{b}s$) and its antiparticle $\bar{B}^0$, an arbitrary neutral B-meson state,

$$a|B_0> + b|\bar{B}_0>$$

is governed by the time dipendent Schrodinger equation:

$$i\frac{d}{dt}\begin{pmatrix} a \\ b \end{pmatrix} = \begin{pmatrix} M - \frac{i}{2}\Gamma & M_{12} - \frac{i}{2}\Gamma_{12} \\ M_{12}^* - \frac{i}{2}\Gamma_{12}^* & M - \frac{i}{2}\Gamma \end{pmatrix}\begin{pmatrix} a \\ b \end{pmatrix} \tag{1.6}$$

The diagonal terms describe the decay of neutral B meson with M being the mass of the flavour eigenstates B^0 and $\bar{B}^0$ and Γ their width. The off-diagonal terms are responsible for B^0-$\bar{B}^0$ transitions. M_{12} and Γ_{12} can be determined from the theory by evaluating the box-diagrams in Fig. 1.2:

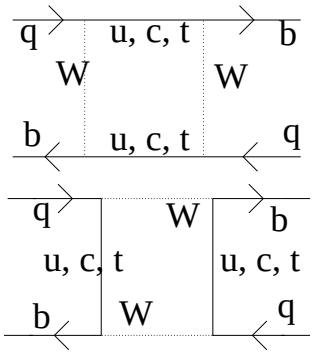

Figure 1.2: Box diagrams responsible for $B - \bar{B}$ mixing.

- M_{12} corresponds to virtual B^0-$\bar{B}^0$ transitions;
- Γ_{12} describes the real transitions due to decay modes common to both states, such as, $\pi^+\pi^-$ or D^+D^-.

These common decay modes are Cabibbo suppressed and therefore represent only a very small fraction of the total B decay rate. The term Γ_{12} in the B^0-$\bar{B}^0$ system can therefore be neglected.

The mass eigenstates will be:

$$B_l = pB^0 + q\bar{B}^0 \quad (1.7)$$

$$B_h = pB^0 - q\bar{B}^0 \quad (1.8)$$

$$\frac{q}{p} = \frac{\sqrt{M_{12}^* - \frac{i}{2}\Gamma_{12}^*}}{\sqrt{M_{12} - \frac{i}{2}\Gamma_{12}}} \quad (1.9)$$

where $q \neq p$ would indicate the presence of the so called *indirect* CP violation. In fact, there are two ways to give rise to CP violation:

- *direct*: $B_1 = (1/\sqrt{2})(B^0 + \bar{B}^0)$ and $B_2 = (1/\sqrt{2})\,(B^0 - \bar{B}^0)$, CP eigenstates, decay without conserving the CP symmetry;
- *indirect*: the B_2 (B_1) part of B_l (B_h) decays conserving CP and the CP violation resides in the fact that the electroweak eigenstates B_h and B_l are compounds of B_1 and B_2.

It is possible to define the parameters $\Delta M_B = M_{B_h} - M_{B_l}$ and $\Delta\Gamma_B = \Gamma_{B_h} - \Gamma_{B_l}$ related to the mixing matrix elements by:

$$(\Delta M_B)^2 - \frac{1}{4}(\Delta\Gamma_B)^2 = 4|M_{12}|^2 - |\Gamma_{12}|^2 \quad (1.10)$$

$$(\Delta M_B)(\Delta\Gamma_B) = 4Re(M_{12}) \quad (1.11)$$

The mass difference ΔM_B was measured, through B^0 and $\bar{B}^0$ oscillations (see following sections) to be:

$$0.467 \pm 0.017\ (\text{ps})^{-1} = (3.07 \pm 0.11) \times 10^{-4}\ \text{eV}$$

From the equation (1.11), once ΔM_B is known, $\Gamma_{12} \ll M_{12}$ implies that $|\Delta\Gamma_B| \ll \Delta M_B$. The lifetime difference $\Delta\Gamma_B$ was found to be tiny and impossible to measure. Therefore B_h and B_l have almost the same lifetime:

$$\tau_{B^0} \simeq (1.549 \pm 0.020)\ \text{ps}$$

From $\Gamma_{12} \ll M_{12}$ it also follows:

$$\left(\frac{q}{p}\right) \simeq \frac{-M_{12}^*}{|M_{12}|}\left(1 - \frac{1}{2}Im\left[\frac{\Gamma_{12}}{M_{12}}\right]\right) \quad (1.12)$$

$$\left|\frac{q}{p}\right| \simeq 1 - \mathcal{O}(10^{-3}) \quad (1.13)$$

Therefore, indirect CP violation in the $\Delta B = 2$ transition through B^0-$\bar{B}^0$ mixing must be a very small effect, as in the K system.

1.3.1 The system time-evolution

Once the neutral B mesons are produced in pairs, their semileptonic decays (inclusive and exclusive) provide an excellent method to measure the B^0 - $\bar{B}^0$ mixing. Because of their respective quark contents, B^0 decays into a positive charged lepton l^+ while $\bar{B}^0$ goes into a negative l^-. If B^0 and $\bar{B}^0$ do not mix, a produced pair B^0 + $\bar{B}^0$ would have a distinctive signature of a dilepton with opposite signs. Therefore, a fully reconstructed $\mu^+ + \mu^+$ event would unambiguously demonstrate the conversion of a $\bar{B}^0$ into a B^0. This event was found [8] and shows that mixing must exist.

The mass difference is a measurement of the oscillation frequency from $\bar{B}^0$ into a B^0 or viceversa. This process is reflected either in the time-dependent oscillations or in the time integrated rates corresponding to the dilepton events having the same sign.

The time evolutions of the mass eigenstates $B_h(t)$ and $B_l(t)$ are given by

$$|B_h(t)> = \left[e^{-t\Gamma_B/2}\right]\left(e^{-iM_Bt}\right)e^{-it\Delta M_B/2}|B_h(0)> \quad (1.14)$$

$$|B_l(t)> = \left[e^{-t\Gamma_B/2}\right]\left(e^{-iM_Bt}\right)e^{+it\Delta M_B/2}|B_l(0)> \quad (1.15)$$

The equations (1.14) and (1.15) when combined with the equations (1.8) and (1.9) give the time evolutions of $B^0(t)$ and $\bar{B}^0(t)$:

$$|B^0(t)> = h_+(t)|B^0(0)> + \frac{q}{p}h_-(t)|\bar{B}^0(0)> \quad (1.16)$$

$$|\bar{B}^0(t)> = \frac{p}{q}h_-(t)|B^0(0)> + h_+(t)|\bar{B}^0(0)> \quad (1.17)$$

where

$$h_+(t) = \left[e^{-t\Gamma_B/2}\right]\left(e^{-iM_Bt}\right)\cos(t\Delta M_B/2) \quad (1.18)$$

$$h_-(t) = i\left[e^{-t\Gamma_B/2}\right]\left(e^{-iM_Bt}\right)\sin(t\Delta M_B/2) \quad (1.19)$$

Therefore, starting at time $t = 0$ with an initially pure B^0 state the probability to find a B^0 ($\bar{B}^0$) at time $t \neq 0$ is given by $|h_+(t)|^2$ ($|h_-(t)|^2$). Taking from the equation (1.13) $|q/p| = 1$, one obtains:

$$|h_\pm|^2 = \frac{1}{2}e^{-\Gamma_B t}[1 \pm \cos(\Delta M_B t)] \quad (1.20)$$

1.3.2 CP asymmetries in neutral B meson decays

The most promising method of measuring CP violation is to look for an asymmetry between the $\Gamma(B^0 \to f_{cp})$ and $\Gamma(\bar{B}^0 \to \bar{f}_{cp})$ where f_{cp} is a final hadronic state having a well-defined CP eigenvalue ± 1. Some example of CP eigenstates are the two-particles systems as: $\psi + K_S$ (CP = -1), $\pi^+ + \pi^-$ (CP = +1) and $\rho + K_S$ (CP = -1). If one defines:

$$A \equiv < f_{cp}|H_W|B^0 >, \quad \bar{A} \equiv < \bar{f}_{cp}|H_W|\bar{B}^0 >, \quad \xi \equiv \frac{q}{p}\frac{\bar{A}}{A} \tag{1.21}$$

the time evolution of the decays can be written as:

$$< f_{cp}|H_W|B^0(t) > \;=\; A[h_+(t) + \xi h_-(t)] \tag{1.22}$$

$$< \bar{f}_{cp}|H_W|\bar{B}^0(t) > \;=\; \frac{p}{q}A[h_-(t) + \xi h_+(t)] \tag{1.23}$$

The time-dipendent CP asymmetry defined as:

$$a(t) = \frac{\Gamma(B^0 \to f_{cp}) - \Gamma(\bar{B}^0 \to \bar{f}_{cp})}{\Gamma(B^0 \to f_{cp}) + \Gamma(\bar{B}^0 \to \bar{f}_{cp})} \tag{1.24}$$

can be derived from the eqauation (1.17). From the equation (1.13), if $|\bar{A}/A|$ = 1 so that $|\xi| = 1$, the asymmetry $a(t)$ simplifies considerably:

$$a(t) = -Im(\xi)\sin(\Delta M_B t) \tag{1.25}$$

In general the amplitudes of B^0 and $\bar{B}^0$ decaying into an arbitrary final state can be written as the sum of various contributions:

$$A = \sum_k A_k e^{i\delta_k} e^{i\phi_k} \text{ and } \bar{A} = \sum_k A_k e^{i\delta_k} e^{-i\phi_k} \tag{1.26}$$

where:

- ϕ_k is the weak interaction CKM phase which represents CP violation;
- δ_k is the strong interaction phase-shift due to rescattering effects among the hadrons in the final state and enters A and $\bar{A}$ without changing sign since strong interactions conserve CP.

Thus, $|A| = |\bar{A}|$ if the various contributions A_k have the same CKM phase, or in particular, if there is only one dominant contribution.

Generally $|\bar{A}|/|A| \neq 1$ since non-leptonic decays in the equation (1.26) receive contributions from both the "tree" and "penguin" amplitudes which in general have different CKM phases as the example in fig 1.3.

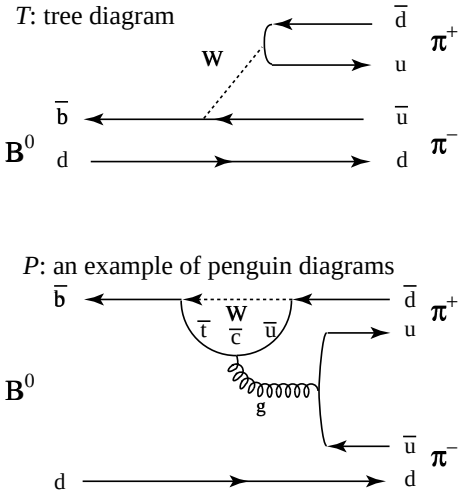

Figure 1.3: The tree and penguin (gluonic) diagram generating $B_d^0 \to \pi^+\pi^-$.

Fortunately, few cases where $|A|/|\bar{A}| = 1$ exist. An example is the channel $b \to s + c + \bar{c}$ responsible for the decay $B \to J/\psi + K$. The final state is a CP eigenstate and it is generated dominantly by the $b \to c$ tree diagram. The decay $B \to J/\psi + K$ is governed at the quark level by $b \to c + s + \bar{c}$ for which the amplitude of the tree diagram is proportional to $V_{cb}V_{cs}^*$. The penguin amplitude for the same reaction has the $V_{tb}V_{ts}^*$ factor which has the same phase as the tree amplitude. So even with the sum of tree and penguin amplitudes, in equation (1.26) one has:

$$\frac{\bar{A}}{A} = \frac{V_{cb}V_{cs}^*}{V_{cb}^*V_{cs}} = e^{-2i\beta} \tag{1.27}$$

and in particular the CP asymmetry is given by:

$$a_{J/\psi K_S}(t) = -\sin 2\beta \sin \Delta M t \tag{1.28}$$

which allows to extract the angle β of the unitarity triangle. The interesting $B \to J/\psi + K$, free from hadronic uncertainties in the evaluation of decay

amplitude, is often called *gold plated channel*. Its experimental study can be used as a consistency check of the CKM mechanism.

1.4 The CKM parameter measurements

The value of $\lambda = sin\theta_C$ is known to be 0.2196 ± 0.0023 from the kaon and hyperons decays [10]. Thus, the two triangles are completely determined by ρ and η, which can be derived from $|V_{\rm cb}|$, $|V_{\rm ub}|$ and $|V_{\rm td}|$, as seen from Fig. 1.1 [1].

Values of $|V_{\rm cb}|$ and $|V_{\rm ub}|$ are extracted from various B-meson decays, based on $b \to cl\nu$ and $b \to ul\nu$ processes, and are currently known to be 0.0402 ± 0.0019 and 0.0033 ± 0.0009 [10], respectively. The value of $|V_{\rm td}|$ is determined from the frequency of $B_d^0 - \bar{B}_d^0$ oscillations.

The situation can be improved once $|V_{\rm ts}|$ is extracted from the frequency of $\rm B_s^0$-$\overline{\rm B}_s^0$ oscillations and $|V_{\rm td}/V_{\rm ts}|$ is used instead of $|V_{\rm td}|$, since the Standard Model calculation of this ratio has a much reduced hadronic uncertainty.

Once ρ and η are derived from $|V_{\rm cb}|$, $|V_{\rm ub}|$ and $|V_{\rm td}|$, the angles α, β, γ can be *indirectly* calculated.

In the Standard Model, *direct* measurements can be made of the angles α, β, γ and $\delta\gamma$, or their combinations, from CP asymmetries in different final states of B-meson decays. Examples are [15]:

1. α from $\rm B_d^0 \to \pi^+\pi^-$;
2. β from $\rm B_d^0 \to J/\psi K_S$;
3. $\gamma - 2\delta\gamma$ from $\rm B_s^0 \to D_s^{\pm} K^{\mp}$;
4. $\delta\gamma$ from $\rm B_s^0 \to J/\psi\phi$;
5. γ from $\rm B_s^0 \to \rho K_s$;
6. $\gamma + 2\beta$ from $\rm B_d^0 \to D^*\pi$.

By studying the channels 2, 3 and 5 very precise measurements of the angles can be performed due to the little theoretical uncertainties. New physics would introduce additional flavour changing neutral currents which would effect the $B_d^0 - \bar{B}_d^0$ and $B_s^0 - \bar{B}_s^0$ oscillations. For such a case, the values of $|V_{\rm td}|$ and $|V_{\rm ts}|$ experimentally extracted from $B - \bar{B}$ oscillations no longer correspond to their real values. The angles $\beta+\gamma$, β, $\gamma-2\delta\gamma$ and $\delta\gamma$, extracted

[1] The parameter A is extracted from measurements of $|V_{\rm cb}|$ and λ.

from the decay channels 1–6, are also affected. These angles, measured in the two ways explained above, will no longer agree.

New physics could be detected from precise measurements of CP violation in various B-meson decays, combined with ρ and η determined from other B-meson decays.

Another way to search for physics beyond the Standard Model is to study B-meson decays that are rare or even forbidden in the Standard Model as $B \to K\bar{K}$ or $B \to Kl^+l^-$. There are many ways to look for a sign of new physics. In all cases, large numbers of both B_s^0 and B_d^0 mesons are required, and many different decay modes have to be reconstructed. Thus, experiments measuring different CP asimmetries with high precision are needed so that a real consinstency check can be done.

1.5 Current experimental situation

Today the B physics is investigated in many experiments. Two B-mesons factories are running: KEK-B at Tsukuba (Japan) and PEP-II at Stanford (USA). Two beams (e^+ and e^-) with moderately different energies collide in both machines producing a boosted $Y(4\mathrm{S})$ which decays in a $B^0 - \bar{B}^0$ pair. Only B_u and B_d mesons can be produced. At these energies the ratio $\sigma_{b\bar{b}}/\sigma_{inel.}$ is about 0.2. The boost is crucial for CP violation study highlighting the presence of secondary vertices and allowing to measure the difference in the decay-time of the two B-mesons.

The main results achieved by these two experiment is the measure of the β angle with a high accuracy. After more than $80{\cdot}10^6$ $B\bar{B}$ reconstructed pairs the results are:

- Babar: $sin(2\beta) = 0.75 \pm 0.09(\mathrm{stat.}) \pm 0.04(\mathrm{syst.})$ [12]
- BELLE: $sin(2\beta) = 0.82 \pm 0.12(\mathrm{stat.}) \pm 0.05(\mathrm{syst.})$ [13]

On the other hand, measurements of α show very large uncertainties and do not allow any conclusion.

CDF and D0 experiments are working on the Tevatron accelerator: a $p-\bar{p}$ machine, with an 1.8 TeV centre of mass energy with all kind of B-mesons produced: B_u, B_d, B_s and B_c. The measure of the β angle performed by CDF gives:

$$sin(2\beta) = 0.91 \pm 0.32(\mathrm{stat.}) \pm 0.18(\mathrm{syst.})\ [14]$$

Taking into account these results, the latest world average is:

$$sin(2\beta) = 0.78 \pm 0.08.$$

Although a good precision in the measurement of β is achieved, nothing can be concluded, up to now, on α and γ. In order to make precise measurements of these two parameters, high performance experiments studying a huge number of B-meson decays are needed.

1.6 B production at LHC

Compared to other operating or under-construction machines, the Large Hadron Collider will be the most copious source of B mesons. It will be a $p-p$ collider with a centre of mass energy of 14 TeV, a bunch crossing frequency of 40 MHz and a project Luminosity of 1×10^{34} cm^{-2} s^{-1}. The main cross section values expected for $p-p$ reaction at such $\sqrt{s}$ are shown in table 1.1.

$\sigma_{tot.}$	100 mb
$\sigma_{inel.}$	80 mb
$\sigma_{inel.} - \sigma_{diffr.}$	55 mb
$\sigma_{b\bar{b}}$	500 μb
$\sigma_{c\bar{c}}$	1.5 μb

Table 1.1: Expected cross section calculated with Pythia.

With a large bottom production cross-section ($\sigma_{b\bar{b}} = 500$ μb), also at moderate *Luminosity* $= 2 \times 10^{32}$ cm^{-2}s^{-1} a huge number of $b\bar{b}$ pairs will be produced in one year (10^{12} pairs/10^7 s). All the B hadrons will be produced: B_u (40%), B_d (10%), B_s (10%) and B_c and other (10%).

The b-quark production will be peaked in forward region and b and $\bar{b}$ will fly in the same direction (Fig. 1.4). The B-hadrons produced in the forward direction have an average momentum of 80 GeV/c. This corresponds to a mean decay length of about 7 mm. Therefore, LHC represents a very useful machine to study in details the B physics.

The b events will be a small part of the total production:

$$\frac{\sigma_{b\bar{b}}}{\sigma_{inel.}} = 0.6\%$$

Therefore, in order to study the b physics at LHC, a very fast and robust trigger system is required for an efficient selection of the interesting events ($pp \rightarrow b\bar{b}$) among the huge number of the ones produced.

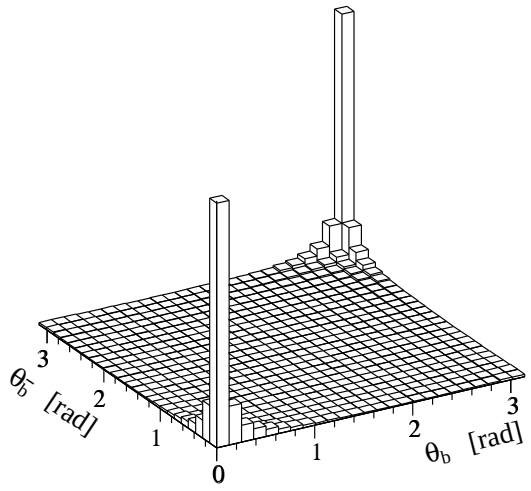

Figure 1.4: Polar angles of the b and $\bar{b}$-hadrons calculated by the PYTHIA event generator.

1.7 The LHCb experiment

The LHCb experiment is a single-arm spectrometer (Fig 1.5) which proposes to study the b physics at LHC. With an angular coverage from 10 mrad to 300 mrad it will detect the decay products of both b-hadrons for about 20 % of the $b\bar{b}$ events. Because of the high rapidity coverage, LHCb plans to operate with an average $Luminosity = 2 \times 10^{32}$ cm^{-2}s^{-1} reduced with respect to the other experiments in LHC for several reasons:

- low detector occupancy;
- reduced radiation damage;
- events dominated by single pp interactions and easier to analyze.

1.8 The LHCb apparatus

The experimental apparatus consists of 5 main subsystems:

- Vertex locator detector;
- Precision tracking system;
- Ring Imaging Cherencov detectors;

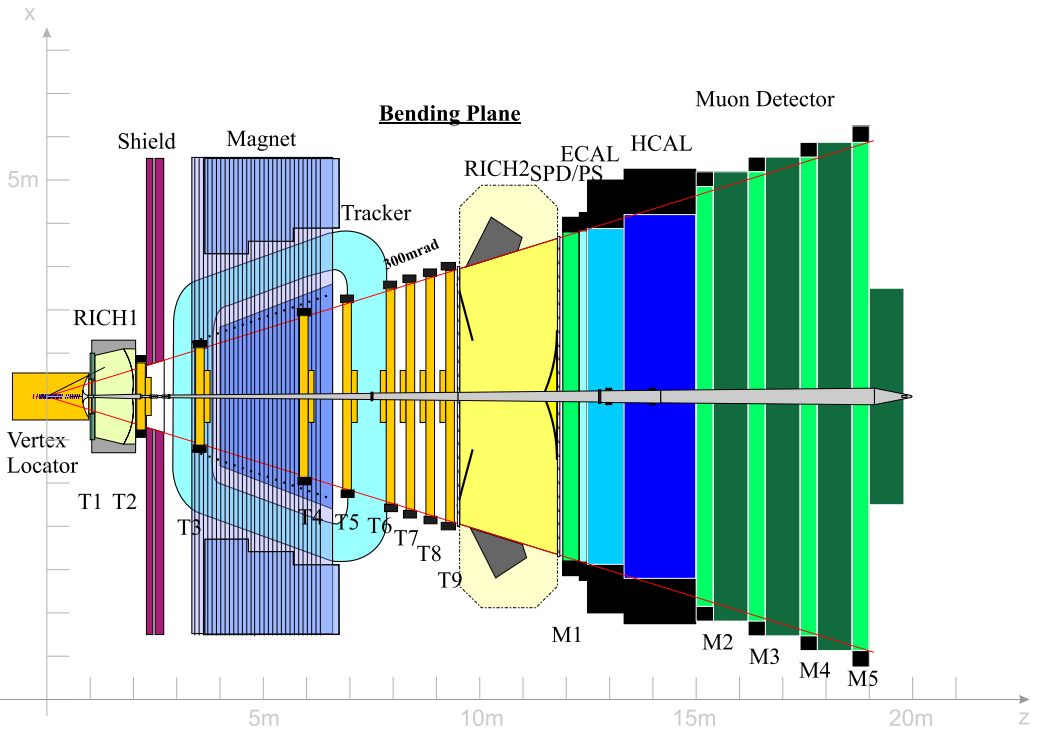

Figure 1.5: Cross section of the LHCb spectrometer (bending plane).

- Electromagnetic and Hadronic calorimeters;

- Muon system.

A magnet providing a dipole magnetic field will be present along the beam line (see Fig. 1.5) down stream of the vertex locator and the first RICH detector. The bending power will be of 4 Tm with a non-uniformity below ± 5 % on an acceptance of $\pm$ 300 mrad in the bending plane and $\pm$ 250 mrad in the non-bending plane. Studies are now undergoing in order to optimize some parts of the LHCb apparatus with respect to the Technical Proposal design, in order to achieve a better physics performance. In this chapter I will describe the experiment in the so called "classical design". The physics requirements and performance of the subsystems will be briefly described in the latter part of this chapter. The muon system will be widely studied in the chapter 2.

1.8.1 The vertex locator

A fundamental requirement for the experiment is a good vertex reconstruction in order to individuate secondary vertices due to b-hadron decays. A very good vertex resolution is needed to study the B_s meson oscillations and their CP asymmetries. In LHCb a VErtex LOcator (VELO) made of 25 stations, each one containing two discs of silicon detector with circular (r) and radial (ϕ) strips will be used. A silicon thikness of 150 μm is used to reduces multiple scattering. The read-out pitch varies from 40 to 90 μm.

The system provides a resolution on the impact parameter of 40 μm for high-momentum tracks.

Two dedicated planes of silicon detectors act as a pile-up veto available for the level-0 trigger. These planes will be placed upstream of the main vertex detector, opposite to the spectrometer arm. Simulations show that 80% of double interactions will be rejected while retaining 95% of the single ones [20].

1.8.2 The tracking system

Charged particle precision tracking will be performed with a system of traking stations. In the original project, 9 stations were planned. Studies are now under way in order to reduce the material budget without spoiling the tracking performance. A different granularity will be used between the inner part where the particle flux is higher and the outer one. The main purposes for the tracking system are:

- High precision particle momentum measurements in order to have a high accuracy in the reconstructed mass of the decaing B-mesons.
- Precise measurements of the direction of the track segments in the two RICH detectors.
- A full track recontruction from the vertex detector down to the calorimeters and muon system.

For the outer regions (98% of the total area) the use of honeycomb-like drift chamber made with straw tubes is planed. This technology will ensure a single hit position resolution of about 200 μm. For the inner part full silicon technology will be used because of the higher fluxes (up to 3.5 MHz/cm^2). From the tracking system a resolution on the B invariant mass measurements of 10$\div$20 MeV is expected from the simulation [21].

1.8.3 RICH detectors

For the study of the channel $B_d \to \pi^+\pi^-$ the separation of kaons from pions will be crucial in order to reduce the background given by $B_d \to K^\pm \pi^\mp$, $B_s \to K^\pm \pi^\mp$ and $B_s \to K^\pm K^\mp$. Also other channels, important for CP asimmetries studies, would be dominated by large background without a reliable K/π separation. To achieve this goal a system consisting of two Ring Imaging Cherenkov has been designed.

The first RICH (RICH 1) is placed upstream of the magnet to detect low momentum particles. The RICH 1 is made of a 5 cm thick aerogel and 95 cm long CF_4 radiators with an expected number of respectively about 15 and 55 photoelectrons detected per track with β=1.

The second RICH (RICH 2) is situated downstream of the magnet and the tracking system and will detect the high momentum particles. It is made of a 180 cm long CF_4 filled radiator with approximately 30 detected photoelectrons per track with β=1. From the simulation, efficiency and purity of the RICH system are expected to be higher than 90 % and a 3σ separation of pions from kaons is expected in a $1 \div 150$ GeV/c momentum range [22].

1.8.4 The calorimeter system

The calorimeter system has three main purposes in the LHCb experiment:

- to provide high transverse energy hadron, electron and photon candidates for level 0 trigger;
- to identify electrons for flavour tagging in semileptonic B decays;
- to reconstruct π^0 and prompt photons with good accuracy.

The system will be composed of an electromagnetic calorimeter (ECAL) and a hadron calorimeter (HCAL).

The ECAL will be made of 2 X_0 preshower (PS) detector needed to separate charged pions and electrons and a 25 X_0 of sampling structure with 2 mm lead sheets interspersed with 4 mm thick scintillator plates. To reduce the background given by high E_T π^0 a scintillator pad detetctor (SPD) will be introduced in front of the PS. The expected energy resolution is:

$$\frac{\sigma(E)}{E} = \frac{10\%}{\sqrt{E}} \oplus 1.5\% \quad \text{(E in GeV)}$$

The HCAL is an iron/scintillator tile calorimeter with plates parallel to the beam. There will be an average of 4 mm scintillator thickness every 16 mm of iron [23]. The energy resolution will be:

$$\frac{\sigma(E)}{E} = \frac{80\%}{\sqrt{E}} \oplus 10\% \quad \text{(E in GeV)}$$

1.8.5 The muon system

The muon system will consist of five detector stations: the first one is placed up-stream of the calorimeters and the others down-stream. Longitudinally segmented shield will be used to attenuate hadrons, photons and electrons. The shield comprises the electromagnetic and hadronic calorimeter and four layers of steel. To reach the fifth station, penetrating the shield, a muon must have an energy of at least 5 GeV.

The detectors chosen for equipping the muon stations are mainly based on Multi-Wire Proportional Chamber technology.

The main purpose of the muon system is a fast measurement of the muon transverse momentum p_t (information used by the level-0 trigger) and a muon track identification for the off-line track reconstruction. The resolution achieved in the p_t measurement is 20 %.

With a moderate value of the p_t threshold ($1 \div 1.5$ GeV/c) the minimum bias retention is expected to be about 2 % while the efficiency on $b \to \mu X$ events should be about 55 % [24].

1.8.6 The trigger system

Given the ratio $\sigma_{b\bar{b}}/\sigma_{inel.} = 0.6\,\%$ and the limits on DAQ and storage capacity, a very efficient trigger system is crucial for the experiment performance. The trigger has to select only the interesting fraction of the $b\bar{b}$ channels. The LHCb trigger consists of four levels of event selection.

Level-0

The level-0 trigger has an imput rate of about 10 MHz and an output rate of about 1 MHz. It is a hardware trigger, based on calorimeter and muon system information. The latency time is 4 μs. A selection of events with leptons, hadrons and photons with a high p_t combined with a pile-up veto is performed. The pile-up veto identifies bunch-crossings having more than one pp interaction using vertex detector and calorimeter information.

The level-0 output rate is mainly composed of events having single high p_t particle: 20 % of muons, 10 % of electrons, 60 % of hadrons and 10 % of photons or multi-leptons.

Level-1

The output trigger rate of the level-1 is about 40 kHz with a maximum latency time of 256 μs. It exploits the presence of displaced secondary vertices of the b events using the vertex locator. After reconstruction of the primary vertex, events showing pairs of tracks with a significant impact parameter to this vertex are selected.

A fraction of events passing the high p_t filter of the level-0 is due to muons produced by particles decaying in flight, electrons from photon-conversion and overlapping showers. The tracking system is used to refine the level-0 trigger. Events are rejected if, in the tracking system, no correspondence is found to the tracks reconstructed by the level-0 trigger.

Levels 2 and 3

The trigger levels 2 and 3 are based on algorithms running on processor farms. Level-2 reduces the rate of events to 5 kHz refining the vertex trigger and rejecting fake secondary vertices due to track multiple scattering.

The level-3 trigger reduces data rate to about 200 Hz. A complete reconstruction of b-hadron decays is performed, using all sub-detectors.

1.8.7 Physics performance

Exploiting the huge number and the variety of B-meson produced at LHC and the layout described above, LHCb will be able to study the B physics with very unique statistics and precision. After one year of data taking, a large number of interesting events are expected (see table 1.2).

In the forward region, parent particle momenta are mainly carried by the longitudinal components of the daughter particle momenta. Therefore, the threshold value for p_t can be kept low. We have seen, for example, that for the muon threshold a value of about 1.5 GeV/c will be used. This allows to acquire a large number of $B_d^0 \to J/\psi K_S$ resulting, after one year, in an accuracy on the β measurement $5 \div 10$ times better than the current one.

The presence of a RICH detector will allow to study channels with K-meson or π in the final state, providing a good measurement of the α and γ values.

Decay Modes	Offline Reconstr.	Physics Observable	Error
$B_d^0 \to J/\psi K_S$ + tag	> 40 k	β	0.6^o
$B_d^0 \to D^*\pi$ + tag	530 k	γ	10^o
$B_s^0 \to D_s K$ + tag	2.4 k	γ	10^o
$B_d^0 \to \pi^+\pi^-$ + tag	4.9 k	α	$(5 \div 10)^o$
$B_d^0 \to \rho\pi$ + tag	1.3 k	α	$(5 \div 10)^o$
$B_s^0 \to J/\psi\phi$ + tag	370 k	$\delta\gamma$	2^o
$B_s^0 \to \mu\mu$	5	rare event with	B.R. $2.0 \cdot 10^{-9}$

Table 1.2: Expected numbers of events reconstructed offline in one year (10^7 s of data taking) with an average luminosity of 2×10^{32} cm^{-2} s^{-1}, for some interesting channels [56].

The high energy in the centre of mass will produce a large number of B_s mesons whose decay channels will be useful to evaluate the $\delta\gamma$ value and to study rare processes.

1.9 Other LHC experiments

We can briefly summarize the performance expected in the B physics sector by the two general purpose experiments operating on LHC: ATLAS and CMS which will operate at a maximal Luminosity of 10^{34} cm^{-2} s^{-1}.

As ATLAS and CMS are designed to look for particles produced in very hard collisions, the detectors have a pseudo-rapidity coverage up to an $|\eta|$ of $2.4 \div 2.5$. The first level trigger, in both experiments, is based on the identification of events with high p_t muons or electrons. The threshold value will be set to $5 \div 6$ GeV/c resulting in a low efficiency for $b\bar{b}$ events.

These experiments can reconstruct B-meson final states containing lepton pairs, such as $J/\psi K_s$ or $J/\psi\phi$. By exploiting these channels, after one year, β will be measured with an accuracy of about 1^o.

The absence of a good π/K separation will not allow to achieve a good efficiency in reconstructing some important channels:

- $B \to \pi\ \pi$. This channel is used for the α angle value extraction. Therefore, in one year, a resolution of about $0.01 \div 0.02$ on the $sin(2\alpha)$ will be achieved which could be of the same order as the measurement itself.

- $B \to DK$ or $B \to D\pi$. These channels cannot be studied and therefore the γ angle will not be measured.

We can conclude that ATLAS and CMS will provide some accurate measurements in the B physics sector for α and, in particular, β angle, but they cannot provide some fundamental measurements on γ and $\delta\gamma$.

Chapter 2

The LHCb muon system

Muons can give very interesting informations on the $pp \to b\bar{b}$ events at LHCb:

- A high transverse-momentum muon can indicate the heavy flavour contents of the initial state;
- Muons from semileptonic b decays provide a flavour tag for the b-hadrons parent;
- Muons are present in the final state of many CP sensitive B decays and, in particular, in the two "gold plated" ones: $B_d^0 \to J/\Psi(\mu^+\mu^-)K_s$ and $B_s^0 \to J/\Psi(\mu^+\mu^-)\phi$;
- Rare and forbidden decays, such as the flavour changing neutral current process $B_s^0 \to \mu^+\mu^-$, have muons in the final state.

For these reasons an efficient and fast muon system has been designed for LHCb.

2.1 System requirements

The main purposes of the muon system are to provide a fast selection of events having a high p_t muon for the level-0 trigger and a high efficiency in muon track identification. As we have seen in the previous chapter, the effective level-0 trigger input rate will be about 10 MHz which has to be reduced to 1 MHz with a latency of 4.0 μs.

Between 10 % $\div$ 20 % of the global level 0 output rate will be allocated to the muon trigger which has to ensure:

- A fast track identification and reconstruction;

- A reliable muon p_t estimate;
- A high efficiency in a 25 ns time window in order to unambiguosly identify the bunch crossing the muons come from;

This imposes very severe requirements on the system layout and on the detectors used.

2.2 Muon system layout

The muon system consists of five stations (M1–M5) placed along the beam line interspersed with iron shields as shown in Fig. 2.1. Each station is

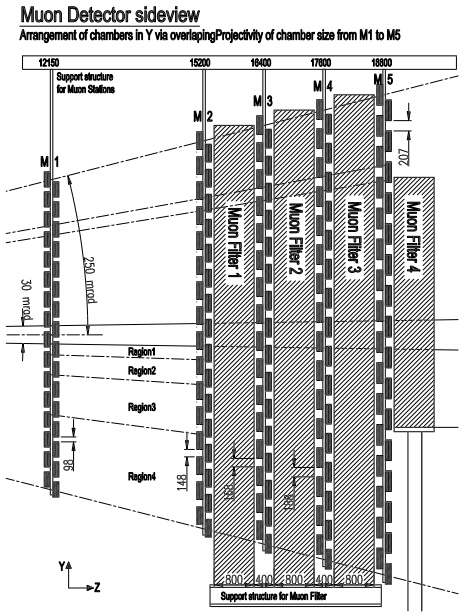

Figure 2.1: Side view of the muon system. The five stations and the iron shield are visible.

composed by two layers of detectors which are readout by separate front-end electronics for redundancy reason. The analog signals coming out from the chambers are discriminated and the logical OR of the digital signals from the two layers is sent to the trigger system.

Because of the large variation in the particle flux between the central and the external parts, each station is subdivided into four regions of different granularity. The detector granularity as seen by the trigger system is called *logical layout* and the logical pads may not coincide with the physical ones.

The logical layout of M2 is shown in Fig 2.2 and the different logical pad dimensions are summarized, for the five stations, in Tab. 2.1. The dimension

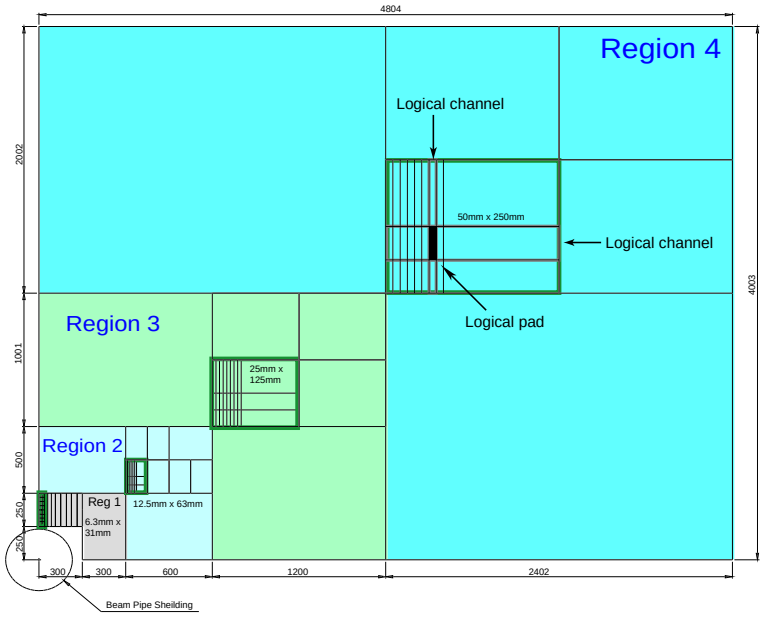

Figure 2.2: Logical layout of the M2 station.

of the logical pads in the bending plane (x dimension in Fig. 1.5) was mainly chosen for the space infomation accuracy required to obtain a good p_t resolution. The y dimension is determined by the rejection of background events which do not point to the interaction region. The logical layout in the five muon stations is projective in y to the interaction point.

	Pad Dimensions at M1 (cm^2)				
	M1	M2	M3	M4	M5
R1	1×2.5	0.5×2.5	0.5×2.5	2×2.5	2×2.5
R2	2×5	1×5	1×5	4×5	4 ×5
R3	4×10	2×10	2×10	8×10	8×10
R4	8×20	4×20	4×20	16×20	16×20

Table 2.1: The logical pad size (scaled as z_{M1}/z_{Mi}). This indicates the exact projectivity in y between stations and the doubling of size in both directions between regions.

2.3 The background

In the muon system a high particle flux (mainly not muons) is expected. This determines strong requirements on the chamber rate capability, ageing characteristics and on the system redundancy. Four main classes of background are expected:

- Muons coming from in-flight decays of the large number of π/K mesons produced in the $p-p$ collisions which represent the bulk of the level 0 muon trigger;
- Photons from π^0 decays interacting in the area around the beam pipe creating electromagnetic showers. Hadrons interacting late in the calorimeters creating shower muons or hadrons punch through;
- Charged particles (mainly low-energy electrons) generated in neutron reactions which in general affect only one detector layer. The hits due to this background can arrive with a maximum delay of few 100 ms after the event;
- muons coming in the beam halo which could cross the muon system simulating a particle coming from the interaction point and cause a muon trigger.

2.3.1 Background simulation

Proton-proton interactions at the centre-of-mass energy of 14 TeV are generated with Pythia 6.1 [25]. The model parameters were tuned to reproduce results for proton-antiproton collision with a centre-of-mass energy in the studied range 50 GeV $\rightarrow$ 1.8 TeV. The LHCb apparatus is described in the context of GEANT 3.21 [26]. Inside the muon shields, in order to keep the event simulation time acceptable, the muons are tracked down to an energy of 10 MeV and other particles to an energy of 500 MeV. In stations M2 and M5, the relatively high tracking thresholds suppress hits that would result from shower generation or photon conversion in the shields. The loss is corrected by adding a parameterised background obtained by a detailed simulation perfomed with GCALOR [27]. With the parameterised background added, the standard simulation for M2-M5 reproduces the GCALOR results to better than 10 %. No parameterised background is added for station M1. In this station, the distribution from standard simulation disagrees from the GCALOR results less than the intrinsic GCALOR uncertainties. Possible inaccuracies in the simulation at high and low energies are accomodated by

using two sets of safety factors to increase the number of hits in all five muon stations. A factor 1 for each station is taken to simulate the so called *nominal background*. Factors 2 for M1 and 5 for M2-M5 define the *maximal background*. A smaller safety factor for M1 is used because of a lower contribution from the low-energy processes. The nominal and maximal rates for each region are summarized in table 2.2.

	M1	M2	M3	M4	M5
R1	$230 \cdot 10^3$	$7.5 \cdot 10^3$	$2 \cdot 10^3$	$2.3 \cdot 10^3$	880
	$460 \cdot 10^3$	$37.5 \cdot 10^3$	$10 \cdot 10^3$	$6.5 \cdot 10^3$	$4.4 \cdot 10^3$
R2	$93 \cdot 10^3$	$5.3 \cdot 10^3$	650	430	350
	$186 \cdot 10^3$	$26.5 \cdot 10^3$	$3.3 \cdot 10^3$	$2.2 \cdot 10^3$	$1.8 \cdot 10^3$
R3	$40 \cdot 10^3$	$1.3 \cdot 10^3$	200	150	130
	$80 \cdot 10^3$	$6.5 \cdot 10^3$	$1.0 \cdot 10^3$	750	650
R4	$12.5 \cdot 10^3$	230	83	50	45
	$25 \cdot 10^3$	$1.2 \cdot 10^3$	415	250	225

Table 2.2: Particle rates (in Hz/cm^2) in the muon system: the first row gives the calculated rate at a $Luminosity = 2 \times 10^{32}$ cm^{-2}s^{-1} ; the second row the rate including the safety factors.

2.4 The level 0 μ-trigger scheme

In order to provide a fast and efficient level-0 trigger the scheme shown in Fig. 2.4 was adopted. A hit in station M3 is called a *track seed*. Starting from each track seed a straight-line is extrapolated forward to the interaction point and backward up to the station M5. In M2, M4 and M5, hits are looked for in regions (field of interest "FOI") centred in the intersections between the station and the straight-line. If at least one hit is found in M2, M4, and M5 FOIs, the track is flagged as a muon candidate. A second straight-line passing through the hit in M2 and the track seed, is extrapolated to M1 to define the centre of the FOI. If at least one hit is found in the M1 FOI the track is definitively flagged as a muon. In M1, the hit closest to the extrapolation point is used, together with the hit in M2, to evaluate the track transverse momentum p_t. Because of the high distance between M1 and M2 (3.1 m) and the high granularity of M1 (see table 2.1) a good resolution on the p_t measurement is obtained. In Fig. 2.3 (a) the p_t resolution as expected from the system simulation is shown. In the whole momentum range $10 \rightarrow 60$ GeV/c a p_t resolution of about 20 % can be achieved.

A first consequence of this scheme is that a muon to trigger must give a hit in all stations and this results in a muon-momentum threshold of 5 GeV.

A threshold in the p_t value will be set to cut the low interesting events. If overthreshold the event is declared interesting ("triggered") and passed to higher selection levels. The value of this threshold is chosen by optimizing the system performance.

In Fig. 2.3 (b) the efficiencies in selecting $b \rightarrow \mu X$ events and in rejecting the minimum bias events are shown in a muon p_t cut range of $0 \rightarrow 3$ GeV for nominal background. A p_t cut of 1.5 GeV would ensure a $b \rightarrow \mu X$ efficiency of 44 % and a minimum bias retention of 1.1 % (i. e. a muon trigger rate of about 110 kHz). This performance would be extremely spoiled without the presence of M1. With a muon p_t evaluated using the hits in stations M2 and M3 (instead of M1–M2), with a total muon trigger output rate of 1.1 kHz, the $b \rightarrow \mu X$ efficiency would be about 26 %.

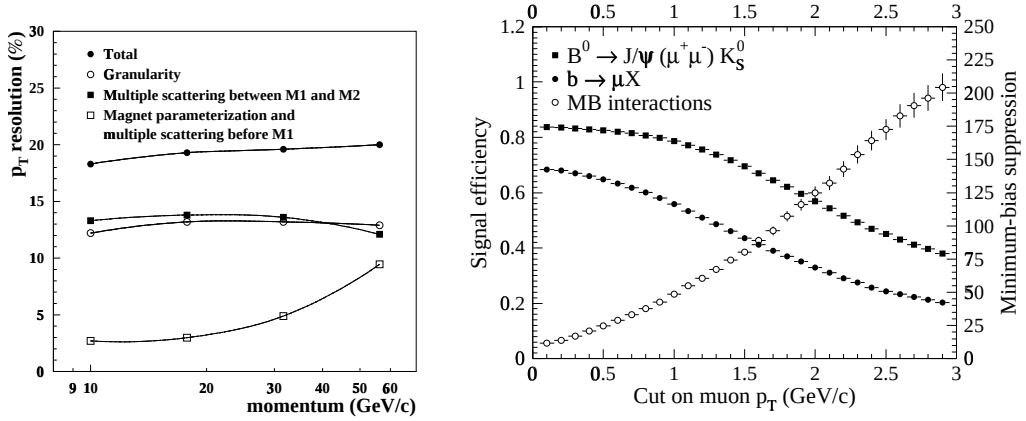

(a) (b)

Figure 2.3: The muon system performance: (a): The p_t resolution of the muon system as expected from the simulation. (b): The $b \rightarrow \mu X$ efficiency and the minimum bias retention as a function of the muon p_t cut.

2.5 Detector performance requirements

The combination of the experiment physics goal and the background conditions has determined the choice of the detectors used in the system. The chamber requirements are summarized in the following:

- *Rate capability and ageing.* The particle flux increases by a factor 2000 from the outer region of M5 to the inner region of M1. This imposes

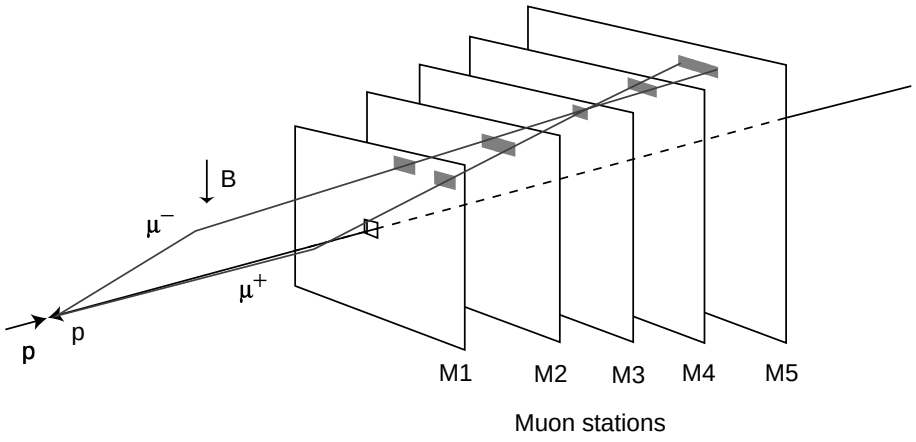

Figure 2.4: Track finding by the muon trigger.

differents requirements on the rate capability and detector ageing according to the chamber position in the system.

- *Time resolution.* In order to have unambiguous bunch-crossing identification a high detection efficiency (99 %) within 25 ns for each station is required. Thus all the chambers should provide very good time performance.

- *Spatial resolution.* A good spatial resolution is required, especially in M1 and M2, in order to obtain an accurate p_t evaluation. It is then important to reduce as much as possible the probability of having more than one pad fired by a crossing track. The average number of pad fired is called *pad-cluster size*. Since two detector layers are present in each station, inclined tracks could hit more than one logical pad giving an effect called "geometrical pad-cluster size" which, in some regions, could reach the value of 1.3 as shown from the simulation. In order to minimise any additional deterioration of the spatial resolution the detector "intrinsic pad-cluster size" has to be kept below 1.2.

2.6 The study on M1 performance

In the muon system, the M1 station plays a very special role. As we have seen, in order to ensure a good p_t resolution the M1 station shows two main differences with respect to the other stations:

1. *The position.* In order to provide a good lever arm and reduce the multiple scattering effect, M1 is placed upstream of the calorimeters. This results in a very high particle flux on the station. In the inner part the particle flux reaches values as high as 500 kHz/cm^2 which is more than 10 times higher than the maximum rate in M2. This imposes very severe requirements on the detector choice and has a large influence on the trigger performance.

2. *The logical pad size.* In the bending plane, the logical pad size in M1 are the smallest of the muon system. A detector ensuring a quite good spatial resolution is then needed.

In order to evaluate the impact of the M1 performance on the trigger system we performed a detailed Monte Carlo study. The method developed and the results obtained will be discussed in the following sections.

2.6.1 Data sample and FOI optimisation

In these studies two different sets of data were used:

- a sample of 13466 $b \rightarrow \mu X$ events with nominal background;

- a sample of 40322 minimum bias (anelastic, diffractive and elastic) events with nominal background. 8820 events had a real muon in the final state.

A minimum bias retenction of 1 % was required which traslates into a level 0 muon-trigger rate of about 100 kHz. First of all, a procedure to determine the trigger FOIs and p_t threshold so as to maximise the trigger efficiency was performed. Afterward, the optimized FOI shown in table 2.3 have been used in the whole simulations. The p_t threshold was set to 1.5 GeV/c.

	Station 1	Station 2	Station 4	Station 5
x FOI	5	7	2	2
y FOI	1	1	1	3

Table 2.3: Optimised FOI (expressed in pad units) for a minimum bias retention of 1% and a p_t cut of 1.5 GeV/c.

2.6.2 Trigger acceptance and M1 efficiency

If for the M1–M5 stations an efficiency of 95 % per layer in 25 ns is achieved this would ensure a station efficiency (two OR-ed layers) larger than 99 % in a bunch crossing time window. The trigger requires one hit in all the stations and thus the whole system would have an efficiency in reconstructing the muon tracks larger than 95 %. A loss of efficiency in one station is expected to influence linearly the whole system performance.

Several studies on the system performance were done by simulating different efficiencies for M1. We studied the station efficiency in the range: 90 % $\rightarrow$ 99.75% which means a single layer efficiency 68.4 % $\rightarrow$ 95 %. The results on the system efficiency for $b \rightarrow \mu X$ events and for minimum bias events are shown in Fig. 2.5. The trigger acceptance for both types of

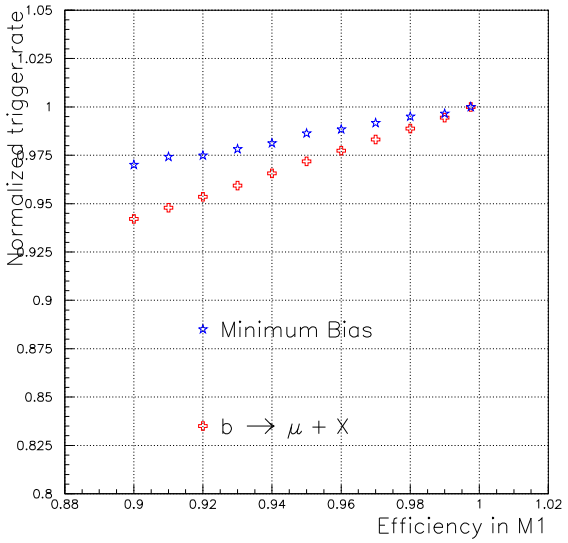

Figure 2.5: Trigger acceptance as a function of the efficiency of the M1 station.

events is found to drop less than the M1 efficiency. For example, when in M1 the efficiency is 90 % the system efficiency on $b \rightarrow \mu X$ events is 94 %. This phenomenon could be understood by studying the hit multiplicities in the M1 FOI (Fig. 2.6). Because of the high M1 occupancy it is often possible to have more than one hit within the FOI. In Fig. 2.6 the FOI multiplicities in M1 for $b \rightarrow \mu X$ and for minimum bias events are shown. In both cases the average number of hits is higher than 1. In fact, the study shows that only 50 % of the hits in M1 come from a true muon, while for M2 the "muon

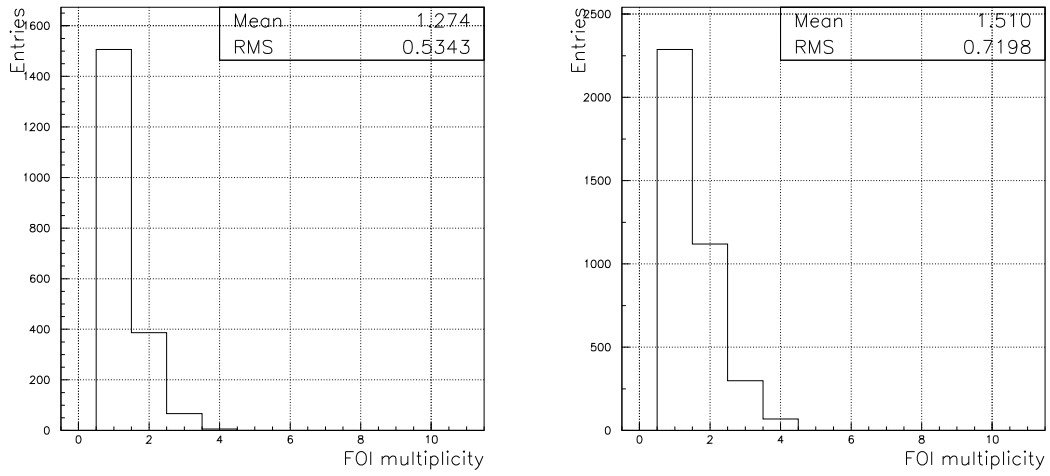

(a) (b)

Figure 2.6: Multiplicity in the FOI of M1. (a): $b \rightarrow \mu X$ events. (b): minimum bias events.

purity" is 95 %. If the detector is inefficient and the "true" hit a of muon track is lost, the system can often find another hit for triggering recovering the efficiency loss of M1.

The second result to outline is that the trigger rate for $b \rightarrow \mu X$ drops faster than the minimum bias event one. This could been explained by the highest FOI multiplicity for the minimum bias events with respect to the $b \rightarrow \mu X$ (Fig. 2.6 (a)).

2.6.3 Trigger acceptance and M1 cluster size

The intrinsic pad-cluster size impact on the system performance is a very important parameter to study for M1.

An intrinsic pad-cluster size of values from 1.0 to 2.0 was simulated. The results on the trigger rate are shown in Fig. 2.7. Two main observations can be done:

- Both the $b \rightarrow \mu X$ and the minimum bias rates increase for high pad-cluster sizes;

- The increase in the minimum bias events rate is steeper than the $b \rightarrow \mu X$ one.

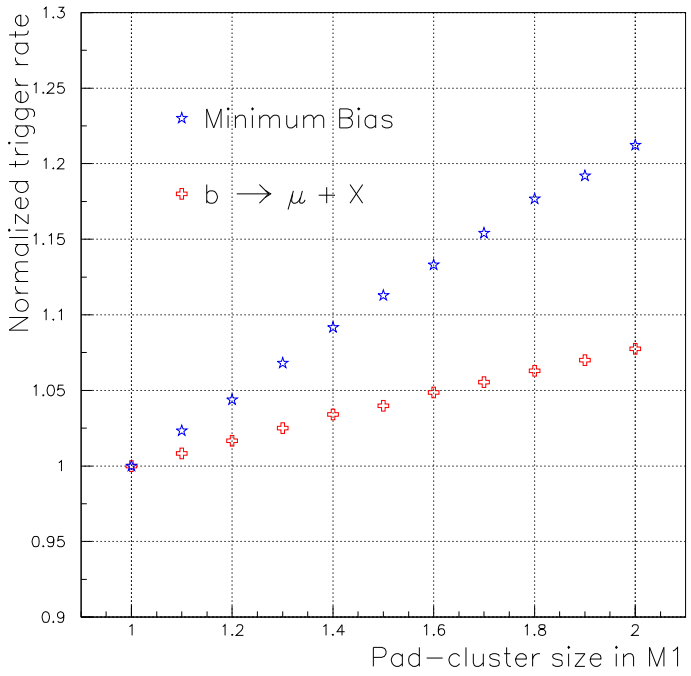

Figure 2.7: Trigger acceptance as a function of the intrinsic pad-cluster size of the M1 station.

This could be explained by a deterioration in the spatial resolution and thus in the p_t resolution due to the large pad-cluster size. This deterioration leads to a lowering in the effective p_t threshold.

The p_t distribution of $b \to \mu X$ and minimum bias events are shown in Fig. 2.8. Around the threshold value used in this study (1.5 GeV) the p_t distributions are very different:

- the $b \to \mu X$ events have a quite flat p_t distribution;
- the minimum bias event p_t distribution increases rapidly at low p_t.

Therefore, a lower effective threshold provides a increse larger for minimum bias events then for the $b \to \mu X$ ones.

In Fig. 2.9 the p_t true distributions of events triggered with a p_t cut of 1.5 GeV/c are reported. Comparing these distributions with the total p_t true distributions (Fig. 2.8), one can see how the p_t threshold cut rejects muons with low momenta.

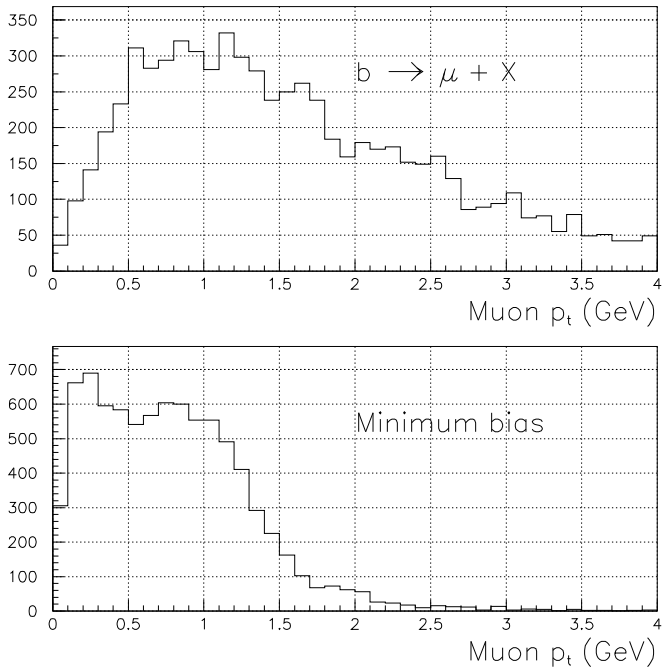

Figure 2.8: Muon true p_t distribution for $b \to \mu X$ (top) and minimum bias events (bottom).

We also studied the events which are "triggered" if the pad-cluster size is 2.0 and are not "triggered" if it is 1.0. In Fig. 2.10 the true p_t spectra of muons coming from these events are shown. The nominal p_t cut was set to 1.5 GeV/c. The mean values of about 1.2 GeV/c confirms how a high pad-cluster size lowers the effective p_t threshold.

2.6.4 Effect comparison and conclusions

To conclude this study we compared the results obtained. The relevant parameter is the ratio between the $b \to \mu X$ ("signal") and minimum bias ("noise") trigger rates. In Fig. 2.11 the normalized ratio as a function of the M1 efficiency and intrinsic pad-cluster size is shown.

Since the minimum bias acceptance increases rapidly for high detector cluster size, the level-0 muon trigger performance deteriorates less for an M1 effeciency of 90 % than for a intrinsic pad-cluster size of 2.0. In particular an M1 efficiency of 90 % would mean a loss in the signal to noise ratio

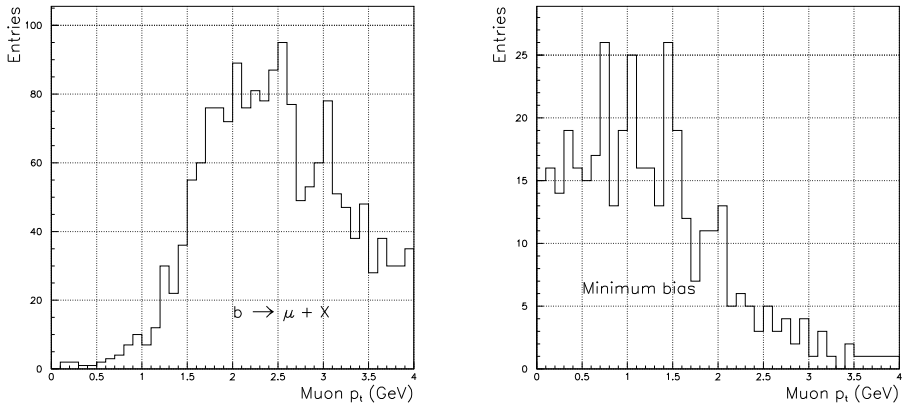

(a) (b)

Figure 2.9: (a): Muon true p_t distribution for events triggered with a threshold of 1.5 GeV/c. (a): $b \rightarrow \mu X$ events. (b): minimum bias events.

comparable with the loss corresponding to an instrumental cluster size of 1.25. A small detector pad-cluster size of 1.10, corresponds, from the point of view of the signal to noise ratio loss to an M1 efficiency of 96 % and thus to a layer efficiency of 80 %.

The official requirements of a maximum pad-cluster size of 1.2 and a minimum efficiency in 25 ns of 99 % seems not to be optimized for M1. Our idea is that the pad-cluster size should be kept as low as possible, while a little inefficiency (up to 2÷3 %) does not have big impact on the muon system performance.

2.7 Muon system technologies

The chamber technologies for equipping the muon system were chosen taking into account the above considerations.

For all regions except the inner part (R1 and R2) of M1 *Multi Wire Proportional Chamber* technology was adopted. A geometry of two gaps in OR for each chamber with wire spacing of 1.5 mm and a gas gap 5 mm wide was chosen (Fig. 2.12). The use of a fast gas mixture ($Ar/CO_2/CF_4$ (40/50/10)) results in a time resolution of 3 ns. A good rate capability was found up to few hundreds of kHz/cm^2. For these chambers the main cross-talk source is represented by the direct induction by particle crossing the detector between the edge of two pads. To keep below 20 % the rate this

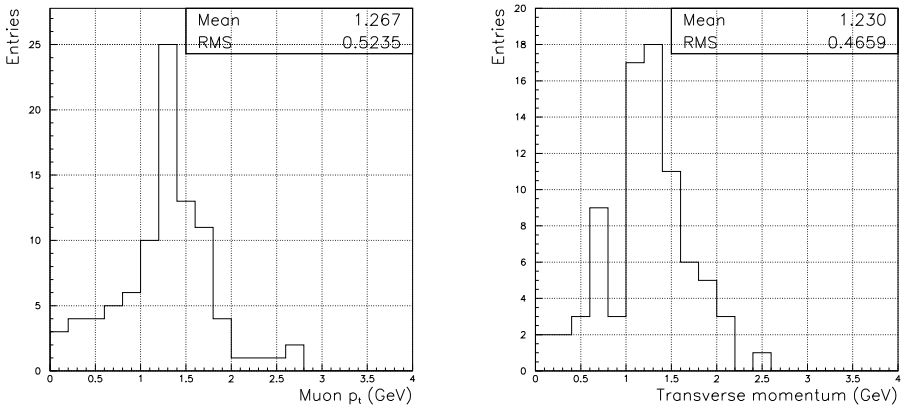

(a) (b)

Figure 2.10: (a): Muon true p_t distribution of (a) $b \rightarrow \mu X$ events and (b) minimum bias events triggered only because of a pad-cluster size of 2.0.

of kind of cross-talk, (which means a cluster size of 1.2) the cathode pad dimensions should be kept larger than 2.2 cm. This explain why this kind of detector cannot be used in R1 and R2 of M1 where the pad x dimensions are 1 cm and 2 cm respectively (table 2.1).

2.7.1 The M1R1 and M1R2 technology

Because of the high particle rate and the detector requirements for the two inner regions of M1 (especially a moderate pad-cluster size) the technology for equipping these regions has not yet be decided.

Although the area of the inner region of M1R1 and M1R2 is 2.9 m^2 (the 6 % of the M1 and less than 1 % of the total), half of the muons will hit these regions.

It is then crucial to find a detector ensuring the good perfomance needed. Two main alternatives were considered:

1. *Detector based on MWPC technology.*
   The direct pad-cluster size can be kept low by placing the anode wires asimmetrically in the gas gap at 1 mm from the cathode pads (*Asymmetric chamber*). This also would allow to operate at reduced gain which means less ageing effects. The ageing problem can be also reduced by reading signal simultaneously on the two cathode plane (*Double cathode read-out MWPC*). The two planes are segmented in pads

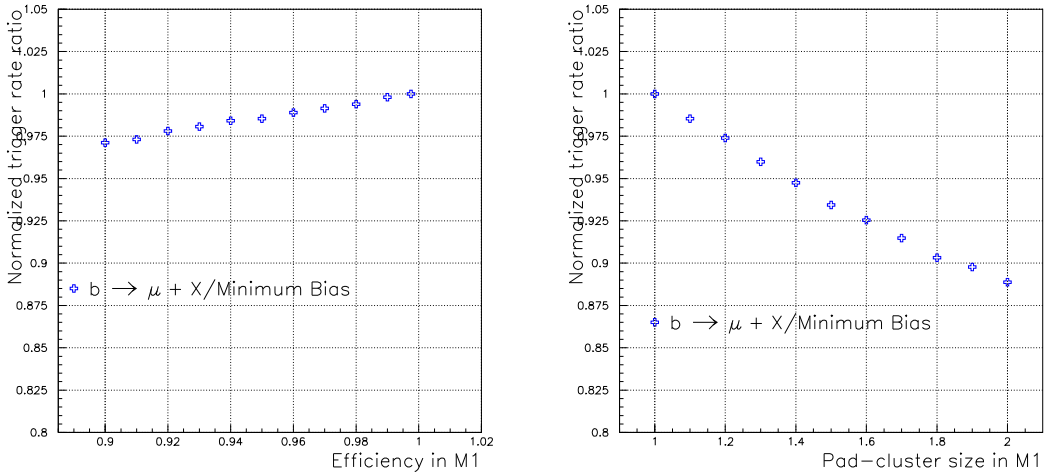

(a) (b)

Figure 2.11: The ratio between the $b \to \mu X$ and minimum bias trigger rates as a function of (a) the M1 efficiency and (b) the M1 cluster size.

and the signal of two facing pads are analogically added. In this way the chamber can work in a configuration with a reduced gain. These two kinds of detector have been built and tested in September 2002. They show two main problems:

- The pad-cluster size reaches the value of 1.32 and 1.39 in the Asymmetric and Double cathode readout respectively;
- Because of the low rate capability (less than 1 MHz/cm^2) the ageing due to 10 years in LHCb cannot be studied in accelerated test and results cannot be achieved in reasonable time.

2. *Triple GEM detector.*
For my PhD thesis I worked in the LHCb group of "Università degli Studi di Cagliari", together with a group from "Laboratori Nazionali di Frascati", to design and develop a triple-GEM based technology for equipping M1R1 and M1R2. Several detector prototypes were built and tested. Very interesting and encouraging results for chamber effiency, cluster size, rate capability and ageing were found.

In the following chapters a detailed description of the work performed will be shown together with the results obtained.

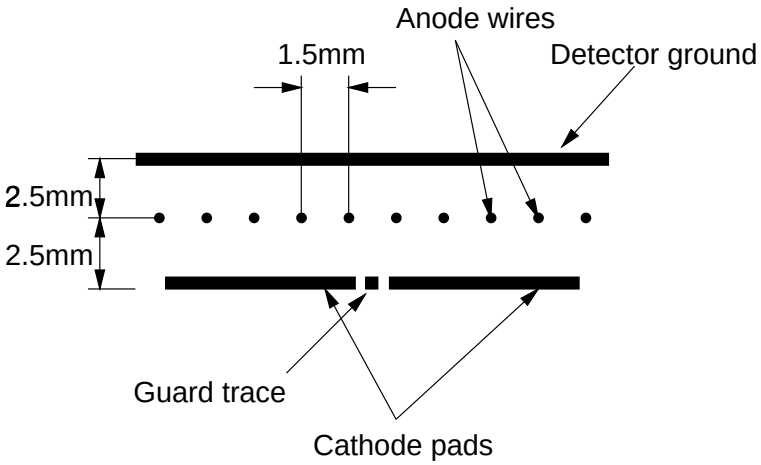

Figure 2.12: The MWPC gap layout.

Chapter 3

The Gas Electron Multiplier

In the last ten years substantial efforts have been made in studying and developing *micropattern gas detectors* (see for example [29]). Due to their good performance (i.e. high rate capability, excellent time and position resolution) and low production costs (their construction is based on photolithographic methods used for industrial fabrication of printed circuit boards) micropattern gas detectors have been proposed for many different applications in astrophysics and high energy physics experiments and medical imaging. In this framework one of the latest development was the GEM: *Gas Electron Multiplier*. Proposed in 1997 [30] they have seen a growing interest in X-ray and charged-particle detection. They have shown the same level of performance as the other micropattern gas detectors, together a very stable operation and robustness.

3.1 Principle of operation

A GEM is a 50 μm thick kapton foil, clad on each side with a thin copper layer (5 μm) and perforated with a high surface density of channels as shown in Fig. 3.1. By applying a voltage difference of the order of 500 V between the two copper sides, an electric field as high as 100 kV/cm is produced within the channels. Primary electrons created in a gas by an ionizing particle can be led towards the GEM by a suitable external electric field. The high field inside the channels induces an avalanche process making them working as multiplication channels. Another electric field in the region below the GEM can extract secondary electrons resulting in an effective gain of the order $10 \div 100$.

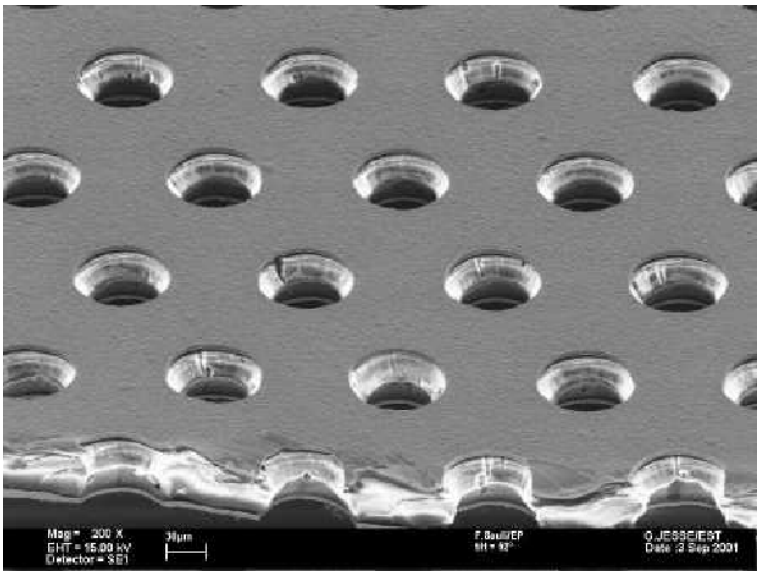

Figure 3.1: GEM foil as seen at the electron microscope.

3.1.1 The drift field

The electric field above the GEM is called *drift field* (E_d). Its main purpose is to drift the electrons created by ionising particles towards the GEM. In a region a few hundreds microns above the GEM the drift field lines connect with the GEM channel field lines which collect electrons into the holes (field lines focusing). A too high drift field would make a large fraction of electrons hit the upper GEM copper side and the electron transparency would reach to the optical one. On the other hand E_d has to be high enough to avoid charge losses in the gas through secondary effects as the recombination.

3.1.2 The GEM channel electric field

The electric field into the GEM channel (E_c) is mainly created by the potential difference applied between the two copper sides (V_{gem}). The main effect of E_c is to allow the avalanche to develop. The number of secondaries created by primary electrons increases while increasing E_c.

A secondary effect of E_c is connected with the GEM electron transparency. A high E_c helps electrons entering into the GEM holes, but on the other hand it reduces the extraction of the secondaries produced.

3.1.3 The transfer field

The transfer of secondary electrons from the GEM channel to another charge amplifier (e. g. GEM or MSGC) is performed by the electric field below the GEM: the *transfer field* (E_t). The higher is E_t, the more efficient the secondary electron extraction is. In the case when the secondary electrons are drifted towards the readout strips or pads, the field is called *induction field* (E_i).

3.1.4 Geometrical parameters

Different kinds of GEM have been built and tested [33]. The GEM foil layout has a large influence on the GEM performance:

- The electric field inside the channels is inversely proportional to the channel width;
- The GEM electron transparency is directly proportional to the channel width and the channel surface density;
- The channel shape has a large impact on the detector performance. The conical shape gives rise to a high electron capture in the kapton resulting in a high GEM charging-up. The charging-up gives causes time variations of the GEM gain (top of Fig. 3.2). On the other hand, the reversed conical shape causes ion capture. Thus, the cylindrical shaped channel is expected to ensure a better GEM operation with respect to the conical or reversed conical ones (bottom of Fig. 3.2).

The current technologies do not allow construction of perfect cylindrical channels. A bi-conical shape results to be the best approximation to a cylindrical one. For charged particle detection, the highest perfomance is provided by the so called *Standard* GEM: bi-conical holes (Fig. 3.3) with an external diameter of 70 μm, an internal of 50 μm and a pitch of 140 μm, resulting in an optical transparency of the order of 20 %.

3.2 Single GEM studies

To achieve a better understanding of the standard-GEM properties we performed several studies. First of all we made a complete and detailed simulation of the microscopic processes occuring in a GEM by means of the Maxwell [31] and Garfield [32] packages. We did not expect accurate quantitative results from the simulation, whose main aim was to gave us an idea

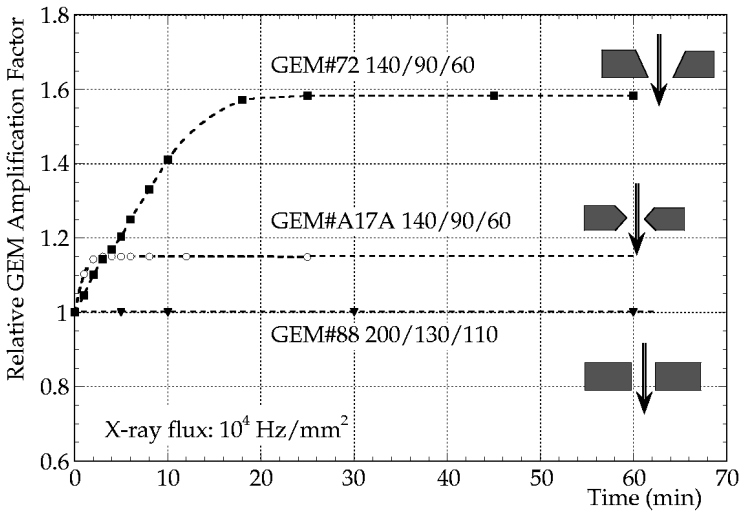

Figure 3.2: Gain time-dependence for several hole shapes under a 10^4 Hz/mm^2 X-ray rate [33].

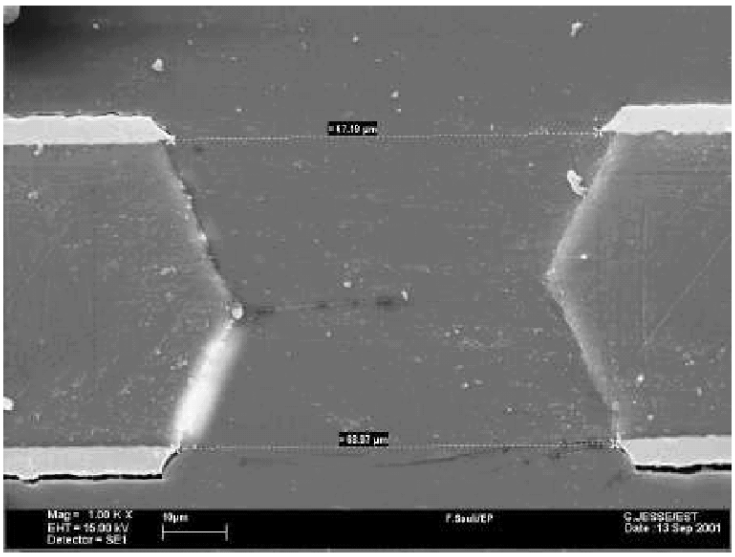

Figure 3.3: GEM hole cross-section as seen at the electron microscope.

of the GEM behavior in different electric configurations. We then wrote a macroscopic analytical model of the charge flows in a single-GEM detector as a function of the electric fields. Then, we performed a set of experimen-

tal measurements using an X-ray tube, in order to check the validity of our model. In all these studies we used an $Ar/CO_2/CF_4$ (60/20/20) gas mixture.

3.2.1 The simulation

The gas mixture

The gas mixture properties were calculated by using the following simulation tools:

- Magboltz [35] was used to compute the electron drift velocity and the longitudinal and transverse diffusion coefficients;
- Heed [36] calculates the energy loss through ionization of a particle crossing the gas and allows to simulate the cluster production process;
- To compute the Townsend and attachment coefficient Imonte 4.5 was used [37].

We report two examples of the gas mixture properties computed. The electron drift velocity calculated as a function of the electric field is compared in Fig. 3.4 (a) with experimental data. The probability distribution of the number of primary clusters produced by a minimum ionizing particle in a 3 mm gap, shown in Fig. 3.4 (b) gives an average value of about 15.

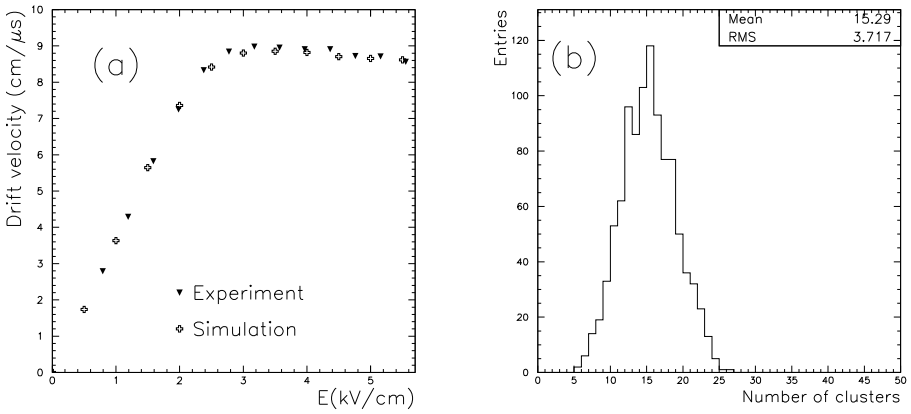

Figure 3.4: $Ar/CO_2/CF_4$ (60/20/20) gas mixture properties. (a): Drift velocity obtained from experimental measurements [38] and from the Magboltz simulation. (b): Number of primary clusters created by a minimum ionizing particle in a 3 mm gap obtained from the Heed simulation.

The electric field configuration

To calculate the map of the electric field resulting by applying a potential difference on the two copper sides of a GEM immersed in an external electric field a 3D-model was built in the Maxwell framework. This model is based on an elementary "cell" with dimension of $400 \times 121 \times 70$ μm^3 shown in Fig. 3.5. A 50 μm thick kapton foil clad on each side (b and c in the figure) with a 5 μm thick copper layer contained in a box is simulated. By setting appropriate

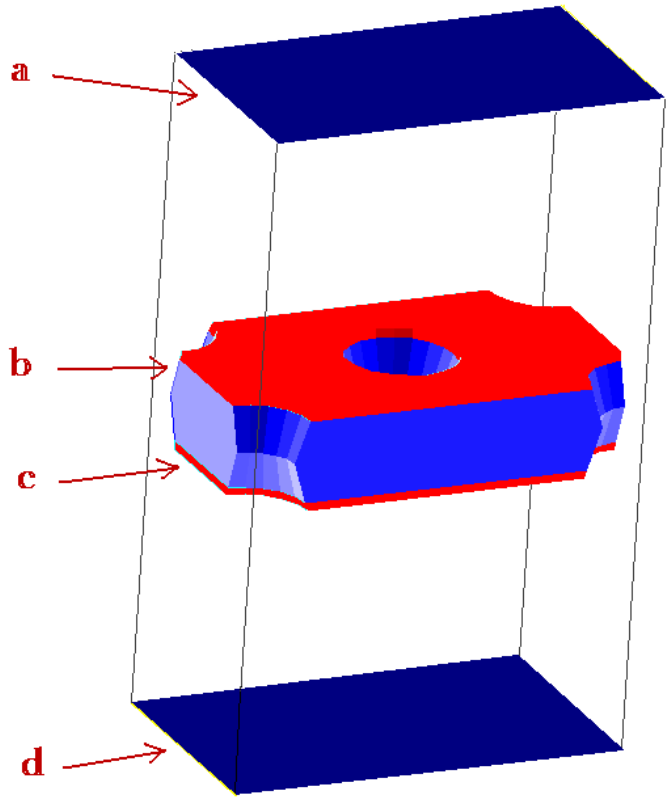

Figure 3.5: GEM foil elementary module layout used in Maxwell.

boundary-conditions on the surfaces a, b, c and d it is possible to reproduce the electrostatic configuration of a GEM foil between two external electric fields. An entire GEM foil can be obtained by periodically replicating this elementary module, when only the electric-field-components tangential to the lateral faces of the box are taken into account. The Maxwell program calculates, by the finite elements method, the electric field map. About 31,000 thetraedrons have been used, resulting in an error on the system

electrostatic energy smaller than 0.04%.

With the model described above we evaluated the electric field in a region around the channel. In Fig. 3.6 the equipotential lines (top) and the electron drift lines without the diffusion effect (bottom) are shown. Since at the channel opening the equipotential lines are bended, the electrons are forced to enter into the hole. The value of E_c as a function of the position along the channel axis and the channel diameter is shown in Fig. 3.7. For a V_{gem} of 450 V a maximum electric field value of 65 kV/cm is obtained.

3.2.2 GEM electron transparency study

The single-GEM electron transparency has been simulated as a function of the external electric fields and V_{gem}. Electrons were produced in a uniformly random position on a surface 150 μm above the GEM (where the equipotential surfaces are almost flat) and then a process of Monte Carlo drift is generated:

- Due to the diffusion effect and to a partial field lines defocusing, some electrons hit the upper GEM electrode (Fig. 3.8 (a)). The ratio between the number of electrons entering the channel and the number of electrons generated above the GEM will be indicated as *collection efficiency*: ϵ^{el}_{coll}.

- Some electrons are lost on the kapton inside the GEM channel because of the diffusion effect. Other electrons can hit the lower copper side of the GEM because of the poor extraction capability of the electric field below the GEM (Fig. 3.8 (b)). The ratio between the number of the electrons extracted (when the multiplication is not simulated) and the number of electrons entering the channel will be indicated as *extraction efficiency*: ϵ^{el}_{extr}.

- For the ions produced in the avalanche process it is possible to define in the same way the parameter ϵ^{ion}_{extr}.

A very important parameter for the charged particle detection is the *electron-transparency* $T = \epsilon_{coll} \cdot \epsilon_{extr}$. In order to evaluate the behavior of T as a function of the electric configurations, simple studies were performed.

- In Fig. 3.9 (a) the electron transparency as a function of the drift field is shown. The ϵ^{el}_{coll} and the total transparency decrease at high drift fields due to the defocusing effect, while ϵ^{el}_{extr} does not depend strongly on this parameter.

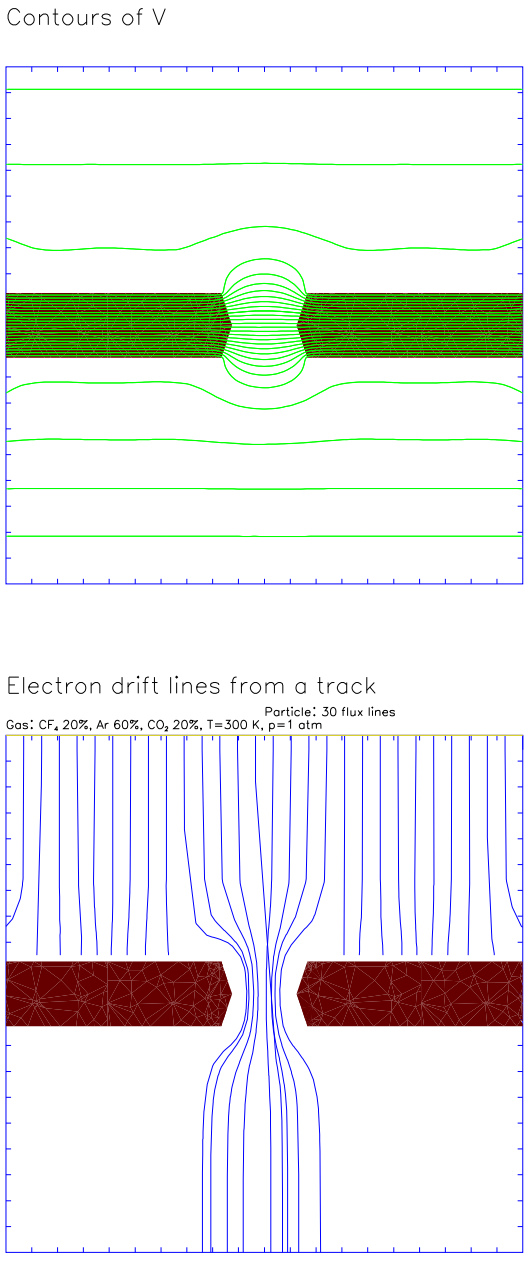

Figure 3.6: Region of 400×400 μm around the GEM channel. (Top): Equipotential lines. (Bottom): Electron drift lines (without diffusion effect).

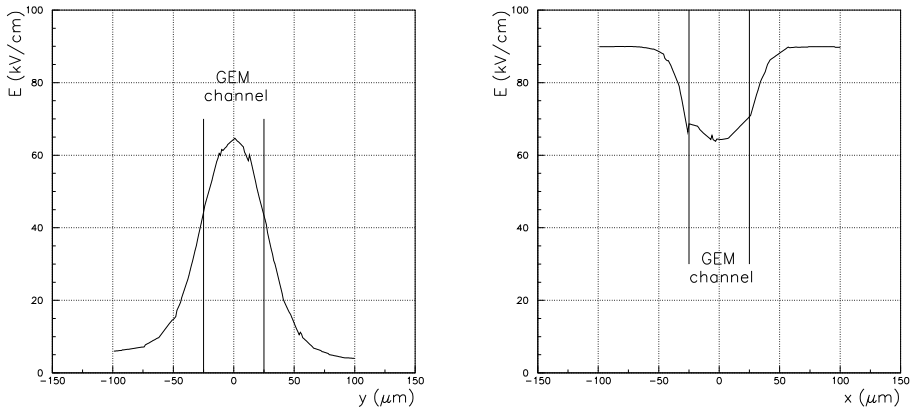

(a) (b)

Figure 3.7: Value of the Electric field as a function of the position in the hole. (a): Along the channel axis (x=0); (b): Along the channel diameter (y=0).

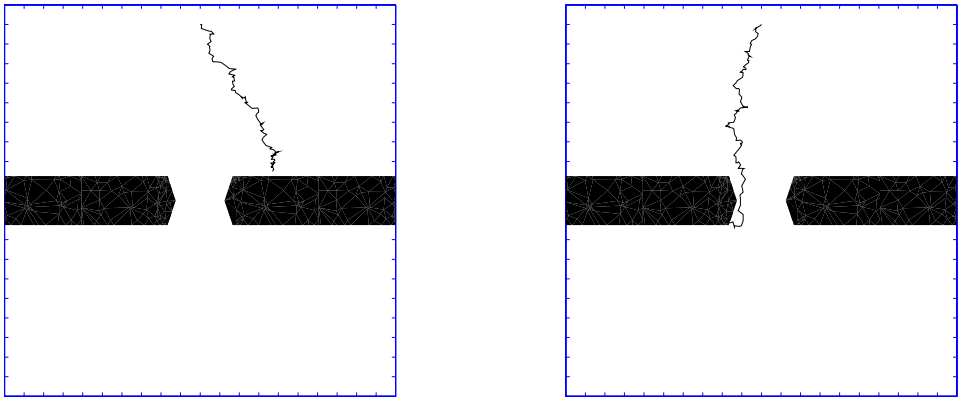

(a) (b)

Figure 3.8: Example of simulated processes: (a) Electron hitting the upper electrode; (b) Electron lost inside a GEM channel.

- In Fig. 3.9 (b) the behavior of T for different transfer fields is shown. Due to a better electron extraction capability the total transparency of a GEM increases at high transfer fields.

The properties of one side of the GEM appear to depend only marginally on the electric field applied on the other side.

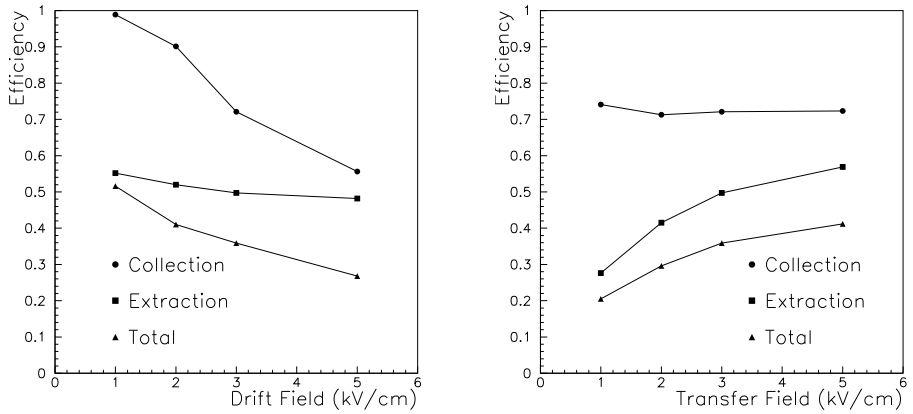

(a) (b)

Figure 3.9: Transparency dependence on drift field (a) and transfer field (b).

3.2.3 GEM gain

When the electrons enter the high electric field region inside the channel they are accelerated. When their energies exceed the first ionization potential of the gas molecules, the electron-molecule impact can results in an ion-electron pair production. The process of ionization by collision is the basis of the avalanche multiplication. In a simple model, the number of pairs produced in a dx path is linearly proportional to the number of electrons:

$$\frac{dn}{dx} = \alpha(E) \cdot n \tag{3.1}$$

The $\alpha(E)$ is called *first Townsend coefficient* and is a function of the electric field.

If electronegative gases are used electron capture processes will occur. As in the equation (3.1):

$$\frac{dn}{dx} = -\eta(E) \cdot n \tag{3.2}$$

where $\eta(E)$ is called *attachment coefficient*. The gain for a single electron drifting from x_1 to x_2 results from the equations (3.1) and (3.2):

$$G = exp\left(\int_{x_1}^{x_2} [\alpha(E) - \eta(E)]dx\right)$$

The Townsend and attachment coefficients calculated with Imonte 4.5 are shown in Fig. 3.10 as a function of the electric field. The field in the channels is larger than 40 kV/cm and then the attachment effect is expected to be negligible with respect to the multiplication. The attachment effect becomes important on secondary electrons leaving the GEM in a zone where the field is less than 20 kV/cm as shown Fig. 3.7 (a).

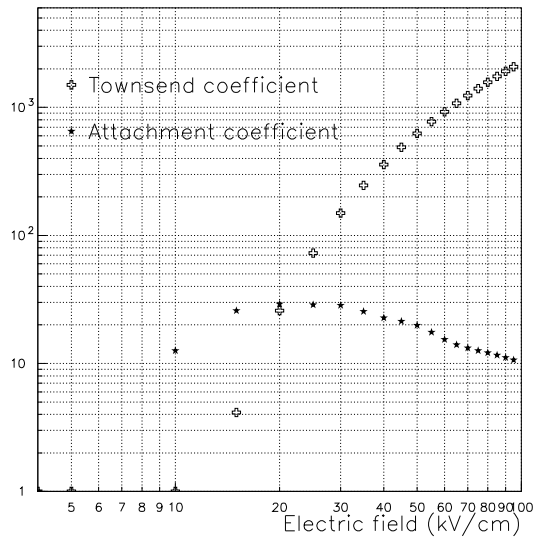

Figure 3.10: Simulated Townsend and attachment coefficients as a function of the electric field.

In order to study the single-GEM gain, avalanche processes were simulated with a Monte Carlo method from Garfield (Fig. 3.11). The drift lines are concentrated near the channel axis (Fig. 3.6 (bottom)) where the electric field is less intense (Fig. 3.7 (b)). Due to the diffusion effect the electrons can reach the regions close to the kapton where the higher field results in a higher multiplication.

The average number of secondary electrons produced for one electron entering into a hole will be indicated as intrinsic gain G_{intr}, while the average number of secondary electrons extracted from the lower side of the GEM for each primary electron generated above the GEM will be indicated as the "effective gain" G. G is related to G_{intr} by:

$$G = G_{intr} \cdot T$$

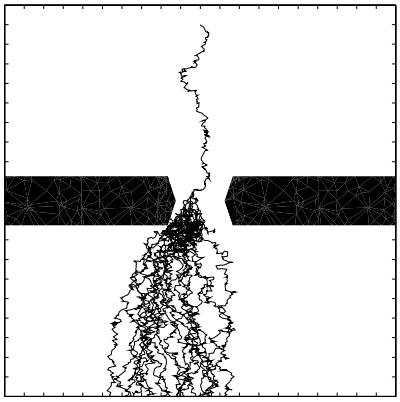

Figure 3.11: Simulated avalanche developping in a GEM hole.

The G and G_{intr} are calculated for different V_{gem} values for a drift field of 3 kV/cm and a transfer field of 5 kV/cm.

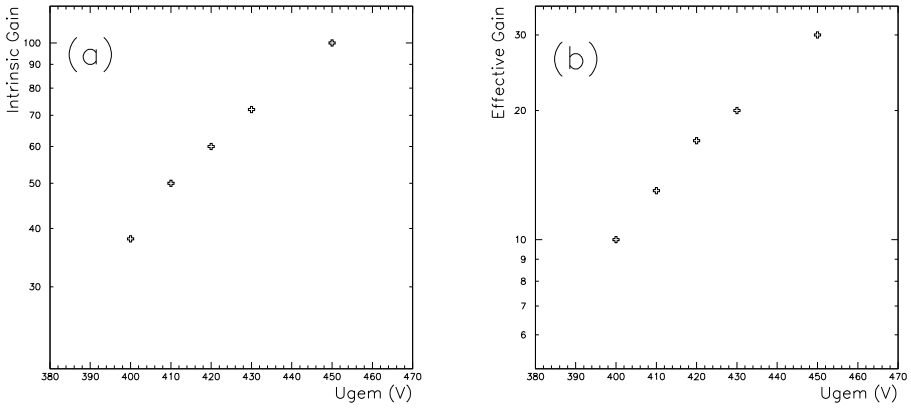

Figure 3.12: G_{intr} (a) and G (b) as a function of the GEM voltage supply.

3.3 Single GEM experimental measurements

The single GEM characteristics have been experimentally investigated by means of an X-ray tube. The tube has an iron internal target and provides

a 5.9 keV photon beam.

The X-rays lose energy in the gas by photoelectric effect. As a photon impacts on an atom, an electron with almost the same energy as the photon is produced. The range of such an electron in the gas is of the order of 100 μm. In this path, it loses its whole energy and produces, in an $Ar/CO_2/CF_4$ (60/20/20) mixture, about 220 electrons.

3.3.1 Experimental setup

For the gain study, a single GEM chamber, as shown in Fig. 3.13, was used. The region between the cathode and the GEM (the *drift gap*) was 3 mm

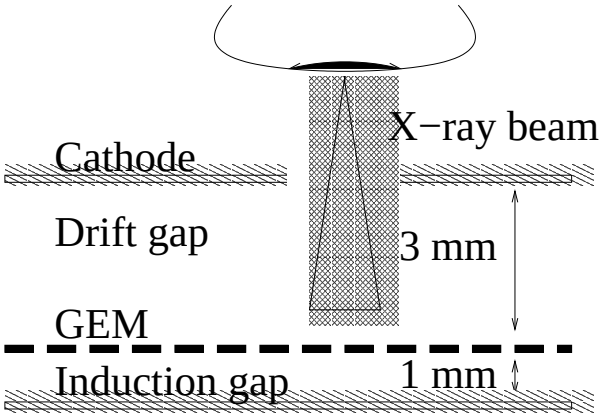

Figure 3.13: Experimental set-up for the measuremets of the GEM detector properties by using an X-ray tube.

wide, while the region below (the *induction gap*) was 1 mm wide. Since the X-ray spot illuminated the chamber as in Fig. 3.13, 90 % of electrons were created into the drift gap. The primary electron clouds drifted up to the GEM and the secondary electrons were collected on the anode. The currents on the detectors electrodes (see table 3.1) were measured by means of a multichannel nanoamperometer.

3.3.2 Analytical model

By means of a simple model (see for details [39]) it is possible to describe the currents flowing in the single-GEM chamber as a function of the detector parameters (ϵ^{el}_{coll}, ϵ^{el}_{extr}, ϵ^{ion}_{extr} and G_{intr}).

If n_0 is the number of electrons created by a single photon and R is the photon interaction rate, we may define the *ionization current* $I_0 = e \cdot n_0 \cdot R$. I_0

Electrode current	Symbol
Cathode	I_c
GEM top	I_t
GEM bottom	I_b
Anode	I_a

Table 3.1: Symbol used for the detector electrode currents.

represents the current which would flow in the detector anode and cathode in the "ionization chamber" mode (no-GEM, gain=1). In presence of the GEM, the detector currents become:

$$\begin{aligned} I_c &= I_0(1+\epsilon_{coll}^{el}\cdot G_{intr}\cdot\epsilon_{extr}^{ion}) && (3.3)\\ I_t &= I_0\left[-(1-\epsilon_{coll}^{el})+\epsilon_{coll}^{el}\cdot G_{intr}(1-\epsilon_{extr}^{ion})\right] && (3.4)\\ I_b &= -I_0\cdot\epsilon_{coll}^{el}\cdot(G_{intr}+1)(1-\epsilon_{extr}^{el}) && (3.5)\\ I_a &= -I_0\cdot\epsilon_{coll}^{el}\cdot(G_{intr}+1)\epsilon_{extr}^{el} && (3.6) \end{aligned}$$

Unfortunately this system cannot be solved and the parameter values cannot be directly extracted with the exeption of:

$$\epsilon_{extr}^{el}=\frac{I_a}{I_a+I_b}. \qquad (3.7)$$

Starting from the simulation results, we made some assumptions on the other parameter behaviors as a function of the electric fields and we expressed them by means of analytical functions containing free constants:

$$\begin{aligned} \epsilon_{coll}^{el} &= exp\left[-(xE_d/V_{gem})^2\right] && (3.8)\\ \epsilon_{extr}^{el} &= 1-exp\left[-(s_-E_i/V_{gem})\right] && (3.9)\\ \epsilon_{extr}^{ion} &= 1-exp\left[-(s_+E_d/V_{gem})\right] && (3.10)\\ E_h &= aV_{gem}+b(E_d+E_i) && (3.11)\\ G_{intr} &= g\cdot e^{\alpha E_h} && (3.12) \end{aligned}$$

The equation (3.8) describes the fact that the collection efficiency decreases rapidly for high E_d.

We found also that V_{gem} helps in collecting electrons into the hole because of the field focusing. The extraction capability is directly proportional to the

external electric field and inversely proportional to the V_{gem} value. This is modelled in equantions (3.9) and (3.10) with functions whose asymptotic limit is 1, which corresponds to the complete charge extraction for a very high external field.

E_h, defined in the equation (3.11), represents the effective electric field into the hole. The two external fields contribute to E_h with the same weight because of the complete geometrical up-down simmetry of the GEM. The gain is described as an exponential function of E_h in equation (3.12) and $\alpha = \mathrm{cm/V}$ is only a dimensional factor.

3.3.3 Measurements

We performed detector current measurements for several values of the drift and induction fields and the V_{gem}. The free constant values were evaluated by minimizing Δ, which is the sum of the squared differences between the measured currents and the ones obtained with the model weighted by the experimental error:

$$\Delta = \Sigma_{j,k} \left[\left(I_{j,k}^{exp} - I_{j,k} \right) / \sigma_{j,k} \right]^2 \tag{3.13}$$

with $j = c, t, b, a$. k varies from 0 to n where n is the number of experimental measurements. The value of I_0, experimentally measured, was let as a free parameter in the minimization procedure. After the Δ minimization, we obtained the following values for the constants:

$$\begin{aligned} I_0 &= (6.9 \pm 0.2)\mathrm{nA} \\ a &= (21.00 \pm 0.03)\ \mathrm{cm}^{-1} \\ b &= (9.0 \pm 0.4) \cdot 10^{-3} \\ x &= (56.90 \pm 0.13) \cdot 10^{-3}\ \mathrm{cm} \\ s_+ &= (68.23 \pm 0.23) \cdot 10^{-3}\ \mathrm{cm} \\ s_- &= (61.90 \pm 0.12) \cdot 10^{-3}\ \mathrm{cm} \\ g &= 11.3 \pm 0.4 \end{aligned}$$

if V_{gem} is expressed in Volts and the electric field values are expressed in kV/cm. The value of I_0 found by the minimization procedure is good agreement with the measured one which was (7.3 ± 0.2) nA. In Fig. 3.14 there are two examples of our sets of measurements. The experimental values of the detector currents (dots) and the behaviors expected from the minimization procedure (lines) are shown as a function of the electric field below the GEM (Fig. 3.14 (top)) and of the GEM voltage (Fig. 3.14 (bottom)). In all cases a

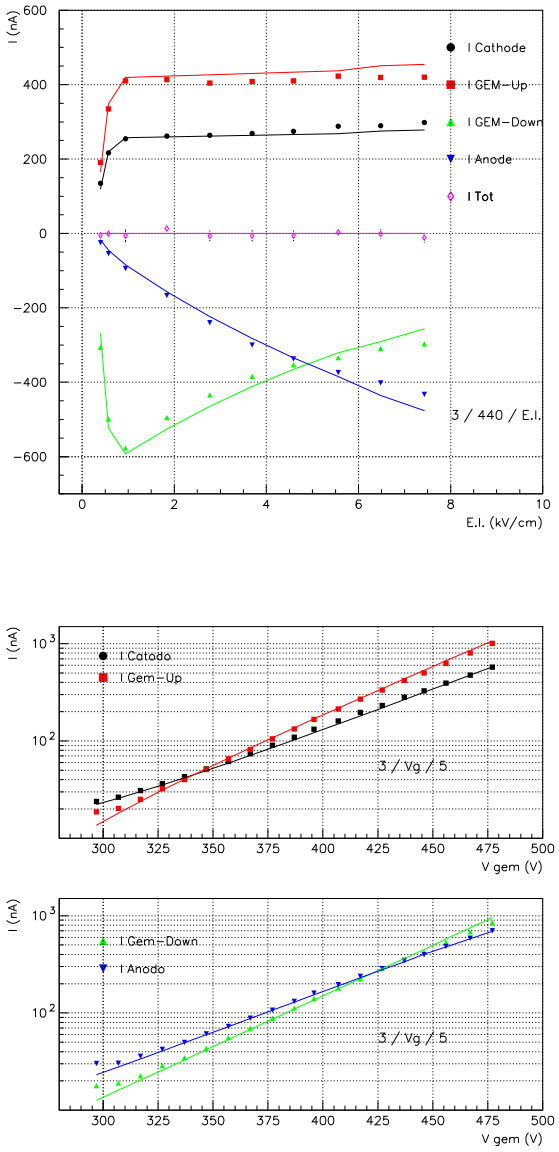

Figure 3.14: Example of comparison between experimental data and the analytical model as a function of the induction field (top) and the GEM voltage supply (bottom).

good agreement was found excluding the case of very low V_{gem} values where the simple gain model in the eqaution (3.12) is no longer valid. With the values above, the detector parameter dependences on the electric fields were

determined and are displayed in Fig. 3.15.

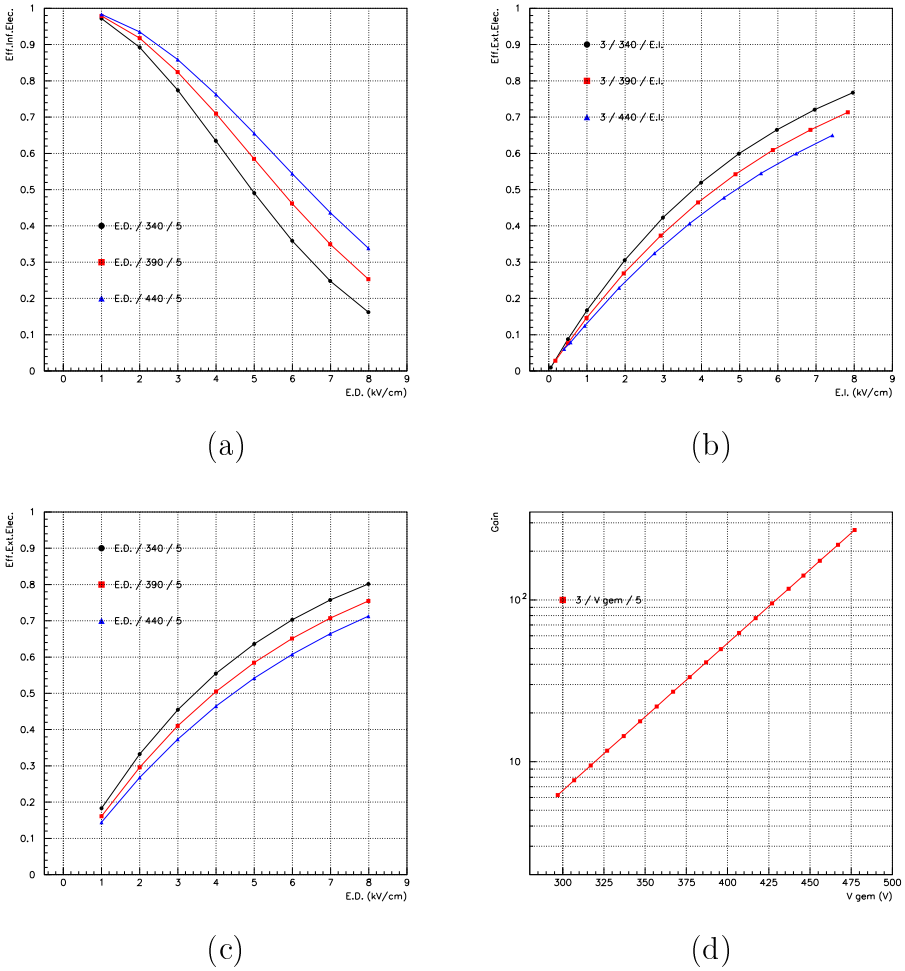

Figure 3.15: Electron collection efficiency (a), electron extraction efficiency (b), ion extracion efficiency (c) and GEM intrinsic gain (d) as a function of the detector electrical configurations.

Very important quantitative information can be extracted from the analysis of the results:

- *(a)*: The ϵ_{extr}^{el} has a strong dependence on E_d. Even for a V_{gem}=440 V a drift field higher than 4 kV/cm produce a loss of about 35 % of the electrons because of the defocusing effect. Because of these results, we decided to work with an E_d in the range $2 \div 3$ kV/cm.

- *(b) and (c)*: The extraction capability of electrons and ions as a function of the external electric field show almost the same behavior. This indicates that the charge diffusion in the gas, which is very different for electrons and ions, has no effect on the extraction process. The extraction capability results very low for low external electric fields: at 3 kV/cm we found $\epsilon_{extr}^{el} \simeq \epsilon_{extr}^{ion}$=40%. In order to extract half of the charge from the channel, an external field of at least 5 kV/cm is needed.

- *(d)*: The intrinsic gain of a GEM operated in $Ar/CO_2/CF_4$ 60/20/20 in the range 300 V $\rightarrow$ 500 V is of the order of $10 \div 300$. In the whole range the experimental values of G_{intr} are larger than the simulated ones by a factor 3 (see Fig. 3.12 (a)). The discrepancy might be due to little inaccuracies in the evaluation of Townsend and attachment coefficients made with Imonte. Since in the simulation of the amplification processes these coefficient are used as exponents, little inaccuracies have a large impact on the secondary electron number computation.

3.3.4 GEM gain fluctuations

Once the gain absolute value is measured, an important parameter to study is represented by the gain fluctuations. They influence the resolution of the GEM detector in measuring the number of primary electrons created by a particle. Moreover, large gain fluctuations may cause detector instabilities.

We simulated single primary-electrons and we computed the number of secondary electrons leaving a GEM for each primary electron after the multiplication. The distribution obtained is shown in Fig. 3.16. It has two main characteristics:

- In the column at 0 we count the number of time where no secondary electrons exit the channel;

- The rest of the distribution has an exponential-like shape with a very long tail.

We have seen that a single 5.9 keV photon produces about 220 electrons in the gas. Using the distribution in Fig. 3.16 we simulated, the charge spectrum of a GEM illuminated by an X-ray tube. The result is shown in Fig. 3.17 (top).

In order to measure the experimental charge spectrum of a single-GEM illuminated by the X-ray tube, the signals on the pads were readout using a front-end electronics whose main characteristics are discussed in the

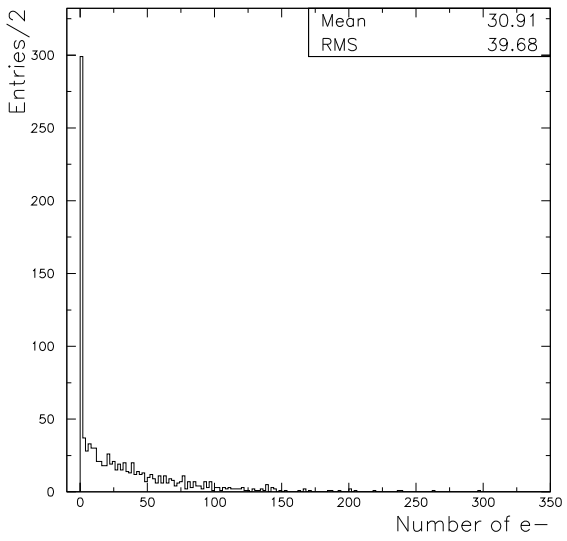

Figure 3.16: Distribution of the number of secondaries leaving the GEM

next chapter (see section 4.2.1). The signals were acquired by using a 50 fC/channel sensitivity ADC. The GEM experimental charge spectrum is shown in Fig. 3.17 (bottom) for a V_{gem}=460 V (the ADC pedestal is already subtracted). The RMS found is about 20 % of the mean value.

The mean values of the two distributions in Fig. 3.17 are very different. This is due to the fact that the GEM gain found with the simulation results to be about 3 times smaller than the real one (see Fig. 3.12 and Fig. 3.15 (d)). On the other hand, the RMS of the distributions are about the 20 % of the mean values in both cases. This could indicate that the plot in Fig. 3.16 represents the real distribution of the numbers of secondary electron produced for each primary electron entering the channel.

3.4 Conclusions

The simulation has been a very useful tool to reach an excellent understanding of the microscopic processes arising during the detector operation. The experimental measurements gave us important indications on how to optimise the GEM performance and quantitative answers on the GEM electron transparency and gain. The comparison between the simulation and the experimental data showed a good agreement for the electron transparency

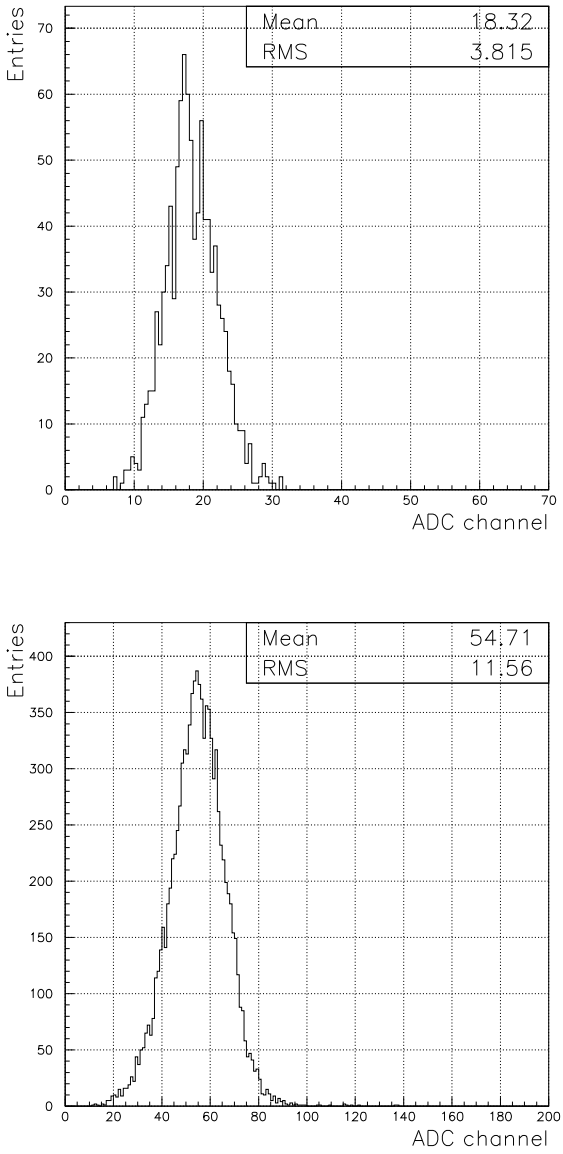

Figure 3.17: Charge spectrum of a single GEM with V_{gem}=460 V illuminated with 5.9 keV X-ray. (top): From the simulation. (bottom): From laboratory measurement.

studies.

The information and results obtained have been used to optimize the triple-GEM detector as illustred in the next chapter.

Chapter 4

The triple-GEM based detector

Structures realized by assembling two or more GEM at close distance, allowing to reach high gains, are good solutions to build efficient detectors operating in safe conditions. In particular, the use of 3 GEM in cascade gives an overall gain of the order of $10^4 \div 10^5$, which is adequate for minimum ionizing particle detection.

4.1 The triple-GEM detector layout

A triple-GEM detector consists of 3 GEM foils sandwiched between two conductive planes: the *cathode*, which together with the first GEM defines the so called *drift gap*, and the *anode* which is usually used as signal readout and is segmented in strips or pads.

The regions between the GEM are called *transfer gaps* while the *induction gap* is the gap between the last GEM and anode. The cross-section of this detector is shown in Fig. 4.1. The ionisation electrons produced in the

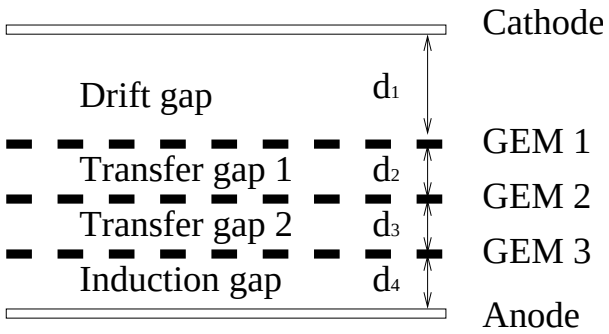

Figure 4.1: Triple-GEM based detector cross-section.

drift gap by a charged particle drift towards the first GEM where they get

multiplied. By means of the transfer electric fields the electron clouds reach the second and then the third GEM. Once the electrons cross the last GEM and appear in the induction gap, they give rise to an induced current signal on the anode. This current is then amplified and shaped by the readout electronics.

4.1.1 The drift gap

The ionization produced in the drift gap, once multiplied by the 3 GEM, induces the main part of the signal. The geometry of this gap has to be chosen to ensure a high particle detection efficiency. For a charged track, the number n of clusters created has a Poisson distribution with an average value $\bar{n}$ depending on the particle energy and the gas mixture. In particular, for a minimum ionizing particle, $\bar{n}$ depends essentially on the gas mixture properties.

For an $Ar/CO_2/CF_4$ (60/20/20) mixture one has $\bar{n} \simeq 5$ clusters/mm (Fig. 3.4). From the Poisson distribution it is possible to calculate that, with a 3 mm thick drift gap, the probability of producing less than 5 clusters is below than 10^{-3}. Even taking into account the non-perfect electron transparency of the GEM, this ensures a very efficient detector operation.

4.1.2 The transfer gaps

In multiple GEM structures a very special role is played by the gaps between the GEM which are not present in the single-GEM detectors. In these gaps the secondary electron clouds are carried out from a GEM and drifted towards the following one. Therefore, the electric field in the transfer gap (the *transfer field* E_t) is an important parameter to study and adjust for an optimization of the charge transfer:

- A high E_t is needed to ensure a good extraction capability of the secondary electrons from the upper GEM in the transfer gap (see Fig. 3.15 (b));
- On the other side E_t has to be kept low to reduce the defocusing effect and to have a high collection efficiency in the lower GEM (see Fig. 3.15 (a));

It is possible to evaluate the chamber behavior as a function of the transfer fields by convoluting the electron collection and extraction coefficients found from single GEM studies in the previous chapter.

The maximum for the electron transparency is found for a transfer field of about 3.5 kV/cm (Fig. 4.2). It results that less than 35 % of the electron produced in a GEM enters the holes of the following one. This represents another important quantitative result from our analytical model. Since it is not possible to separate the GEM gain and the GEM transparency, there is no a direct way to measure the absolute value of the electron transparency of a transfer gap.

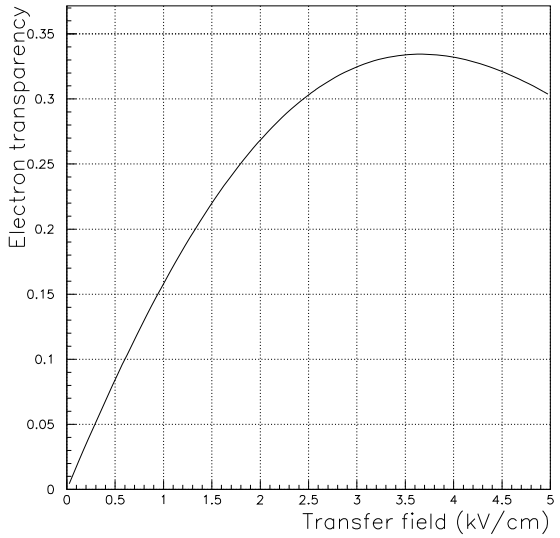

Figure 4.2: Electron transparency of a transfer gap as a function of E_t evaluated by the convolution of ϵ^{el}_{extr} and ϵ^{el}_{coll} found in previous chapter (Fig. 3.15).

We studied experimentally the electron transparency behavior as a function of the transfer fields. We tested a 3-GEM detector with a 1 mm thick transfer gap 1 and 2 mm thick transfer gap 2. In Fig. 4.3 the current on the pads as a function of the two transfer fields are shown ((a) as a function of the transfer field 1 and (b) as a function of the transfer field 2). As the GEM gains are indipendent from E_t the electron transparency of the detector results optimized when the pad current value is maximum.

The pads current has a maximum for a value of about 3.4 kV/cm for both the transfer fields 1 and 2. This result is in agreement with the behavior found by the convolution of ϵ^{el}_{extr} and ϵ^{el}_{coll} (Fig. 4.2) and means that the optimized E_t is gap-thickness indipendent.

In all the following measurements and tests, the value of the transfer field has been kept in the range $3 \div 4$ kV/cm.

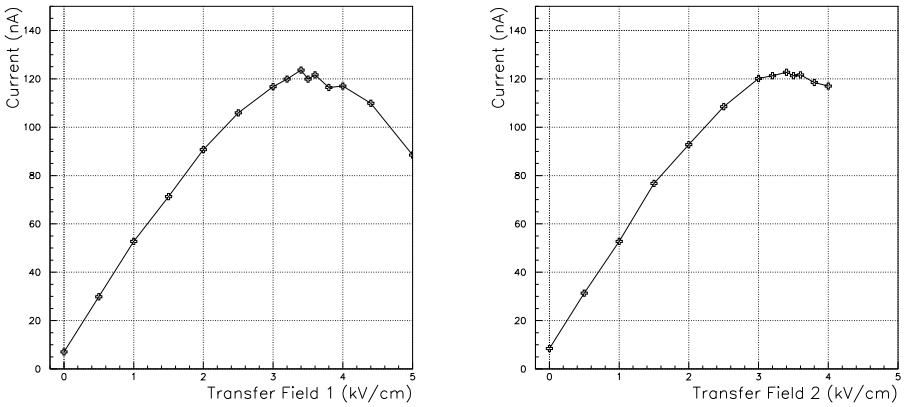

(a) (b)

Figure 4.3: Electron transparency study: the anode current as a function of the transfer fields.

4.1.3 The induction gap

In order to maximize the amount of charge collected on the pads, the electron transparency was studied as a function of the *induction field* E_i. As it is known from the X-ray measurements (see Fig. 3.15 (c)), the higher is E_i the higher the electron extraction capability from the third GEM is. A too high electric field could give raise to detector instabilities. For this reason we choose to work with an E_i of 5 kV/cm.

4.1.4 Signal formation

In GEM based detectors the signal is completely induced by the electron motion in the *induction gap*. As the electrons emerge from the last GEM, they start to induce on the pads a current which stops when they are collected. The time evolution of the current can be calculated by means of the Ramo theorem [41]:

"Given any configuration of electrodes $1, ..., j, ..., n$ at different potentials $V_1, ..., V_j, ..., V_n$, the current flowing into an electrode k due to a moving charge q is:

$$I_k = \frac{-q\vec{v}(x) \times \vec{E}_k(x)}{V_k} \tag{4.1}$$

where $\vec{E}_k(x)$ is the electric field created by raising the electrode k to the potential V_k while keeping $V_{j \neq k} = 0$."

In particular, if V_k=1 V the resulting electric field is called *weighting field* ($\vec{E}_k^w$) and the Ramo theorem becomes:

$$I_k = -q\vec{v}(x) \times \vec{E}_k^w(x) \tag{4.2}$$

By using the Ramo theorem we can calculate the current induced by one electron drifting in the induction gap on a 1 $\times$ 1 cm^2 pad. In Fig. 4.4 the equipotential lines of the weighting field of the pad placed in a 1 mm wide induction gap are shown. In this configuration the pad transversal dimensions

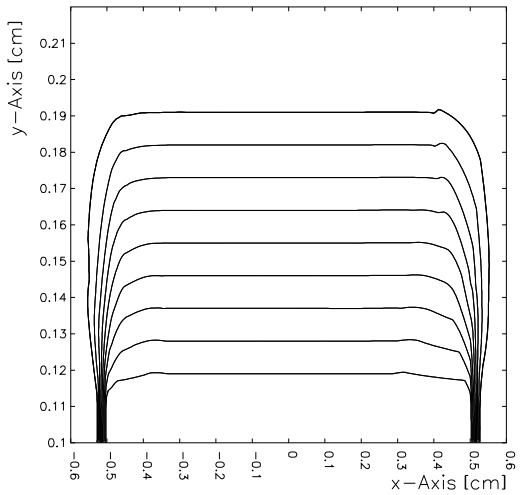

Figure 4.4: Weighting field of a 1 $\times$ 1 cm^2 pad in a 1 mm gap.

are large with respect to the gap thickness. Therefore, apart some boundary effects, $\vec{E}_w(x)$ is almost constant above the pad. The real electric field is also constant in the gap and then the electron drift velocity is constant too. From the equation 4.2 it follows that the drifting electrons induce a constant current I during the drift process (Fig. 4.5). If q is the charge collected, since

$$\int_{\text{drift time}} I \cdot dt = q, \tag{4.3}$$

the shorter is the drift time the higher the value of I. For this reason the induction gap has bo be chosen as thin as possible. We adopted a 1 mm wide induction gap.

Another interesting application of the Ramo theorem is the possibility of calculating the signal induced by a charge collected by a pad, on the

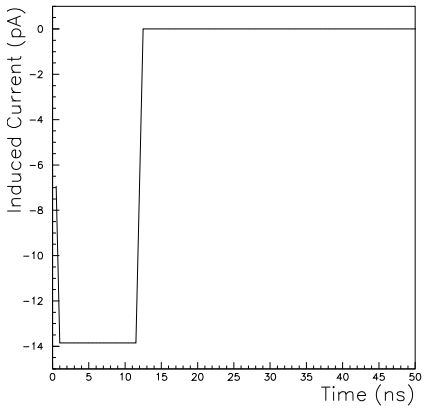

Figure 4.5: Current I induced on a pad by one electron drifing in the last gap as calculated with Ramo theorem.

neighbouring ones. This represents the *cross-induced* signal. In Fig. 4.6 the weighting field of the pad A in the region between two pads is shown.

If an electron drift in the last gap and is collected on the pad B (for example in the position $x = 480$ μm) we cas use the Ramo theorem to evaluate the cross-induced signal:

- The drift velocity and the weighting field are anti-parallel in the upper region of the gap;
- In the central region they become orthogonal;
- In the lower region they are parallel.

This means that we should expect a bipolar induced current. Moreover, in this case no charge is collected on the pad A. Therefore from the equation 4.3 we expect that the area under the two poles should be the same.

In Fig. 4.7 the cross-induced current in this case is shown as calculated with the Ramo's theorem. The two poles are clearly visibles. The cross-induced signal peak value (-1.5 pA) is about ten times smaller than the direct-induced one (Fig. 4.5).

4.2 Detector prototypes layout

The detector prototypes were built by using 10 $\times$ 10 cm^2 GEM. The GEM foils are stretched by using an "home-made" tool (Fig 4.8 (a)) and then glued

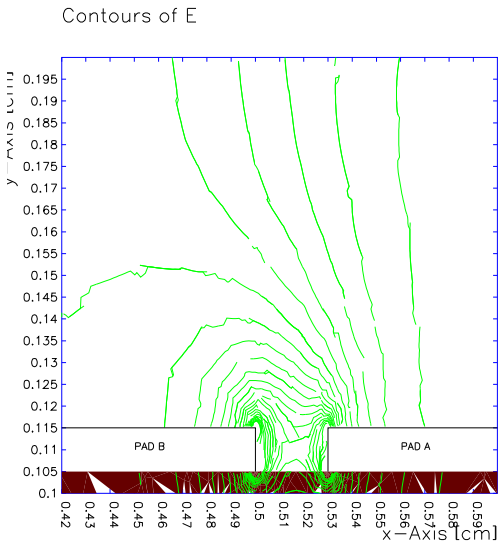

Figure 4.6: Electric field lines of the weighting field at the edge between two pads.

on fiberglass frames. In Fig. 4.8 (b) some GEM during the glueing procedure are shown.

After the glueing, the GEM are stacked in the gas tight box, together with the pad plane (used as anode) and with a conductive plane (the cathode) used to define the drift field. The pads used in our prototypes have 1×2.5 cm^2 dimensions. The gap thickness is determined by the GEM frames and no spacers are used between the GEM. Fig. 4.8 (c) shows the detector inside the gas-tight box before the closing.

4.2.1 The read-out board

The signals on the pads were readout with VTX electronic boards ([53]) whose main characteristics, measured in laboratory, are summarized in the table 4.1.

rise time	9.2 ns
sensitivity	12.3 mV/fC
noise	1820 e$^-$
cross-talk	5 %

Table 4.1: VTX read-out electronics characteristics.

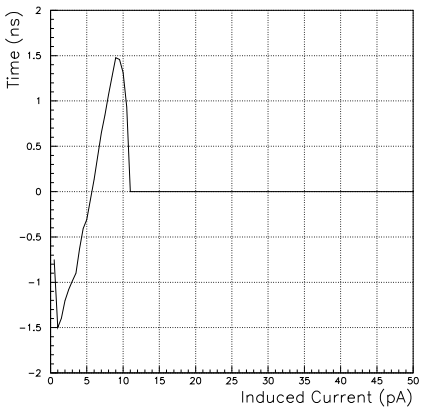

Figure 4.7: Current I induced by one electron collected on the neighboring pad as calculated by the Ramo theorem.

Capacitive cross talk between different channels on the board was found. The height of the cross-talk induced signal was measured to be the 5 % of the height of the original signal.

4.2.2 The track signal

The charge clouds produced by the multiplication of the primary electron clusters, will cross the chamber up to the last gap where they induce a current on the pads until they get collected. The signal of a charged track is given by the convolution of the single signals due to the different electron clouds reaching the induction gap. The current induced on the pads is then amplified and shaped by the read-out electronics. An example of a track signal as seen at the electronics output is shown in Fig. 4.9. It is possible to see:

1. the signal rise due to the arrival of the first electron cloud in the last gap;

2. the flat part of the signal, visible between t=45 ns and t=55 ns, due to the constant $\vec{E}_w$;

3. the signal duration time which is about 30 ns corresponding to the maximum drift time in the ionization gap.

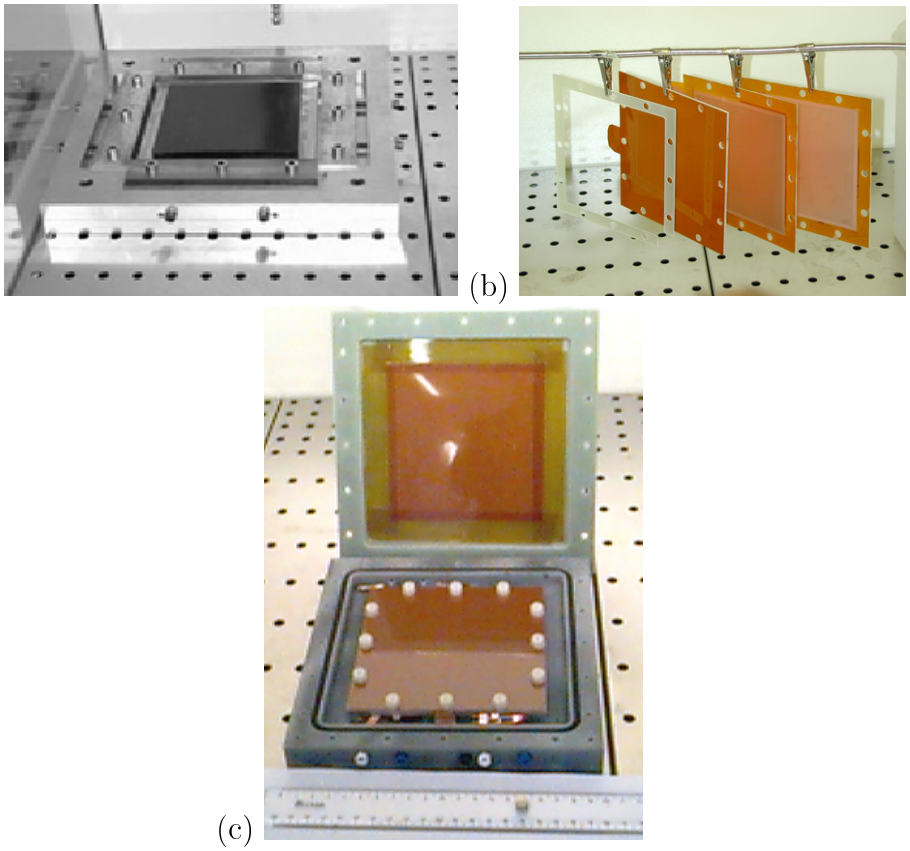

Figure 4.8: (a): The GEM stretcher. (b): GEM glued to frame support in the clean room. (c): A triple GEM detector in the gas-tight box before the closing.

4.3 Test and measurements with X-rays

4.3.1 Detector gain

Each single GEM has an effective gain which is an exponential function of the voltage applied as shown in section 3.2.3:

$$G^{(i)} = A_k e^{\alpha_k V_{gem}}$$

A_k and α_k being dependent on the gas mixture. The detector gain is essentially given by:

$$G = G^{(1)} \cdot G^{(2)} \cdot G^{(3)} = A_k^3 e^{\alpha_k (V_{gem1} + V_{gem2} + V_{gem3})} \tag{4.4}$$

and results a function of the sum of the 3 GEM voltage supplies (V_{tot}).

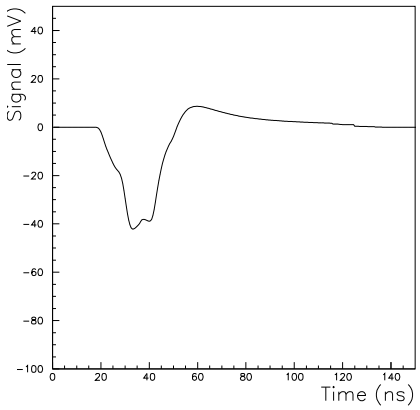

Figure 4.9: Signal due to a track after the electronics.

The overall detector gain for different gas mixtures was measured by using the X-ray tube. The results are shown in Fig. 4.10 and the following observations can be done:

- The presence of the isobutane make possible to reach higher gains at low V_{tot};
- In the Ar/CO_2 based mixtures the larger is the Argon percentage the higher is the gain for a fixed V_{tot};
- The presence of the CF_4 limits the avalanche development because of its high electron affinity resulting in a lower gain;

All these effects explain the lowest gain of the $Ar/CO_2/CF_4$ (45/15/40) mixture with respect to the other ones for a given V_{tot}.

From the exponential fit of the measurements in Fig. 4.10 we obtained the following functions describing the detector gain for the different gas mixtures:

- $G(Ar/CO_2\ 70/30) = \ 3 \cdot 10^{-6} \cdot \ \exp(20.0 \cdot V_{tot})$;
- $G(Ar/CO_2/CF_4\ (60/20/20)) = \ 3 \cdot 10^{-5} \cdot \ \exp(16.9 \cdot V_{tot})$;
- $G(Ar/CO_2/CF_4\ (45/15/40)) = \ 2 \cdot 10^{-7} \cdot \ \exp(19.4 \cdot V_{tot})$;
- $G(Ar/CF_4/C_4H_{10}\ (65/28/7)) = \ 1 \cdot 10^{-7} \cdot \ \exp(24.7 \cdot V_{tot})$;

where V_{tot} is expressed in kV.

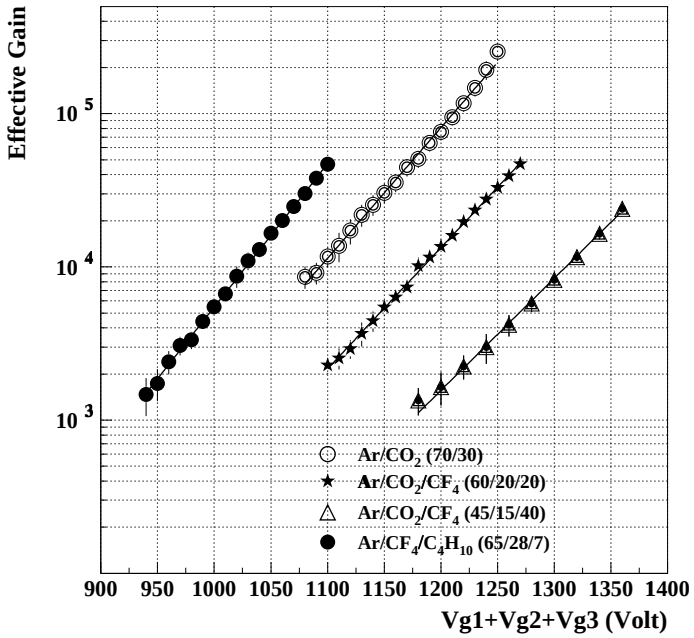

Figure 4.10: Measured gain of the 3-GEM detector with different gas mixtures.

4.3.2 Rate capability

The main limitation to high rate capability in a gas detector is the dead time needed to free the multiplication region from the slow ions restoring the electric field for a new avalanche developing.

The GEM channel is 50 μm high and can be completely freed in less than 10 μs. This leads to a maximum rate of 10^5 Hz/channel. In a 1 cm^2 area about 5000 channels are presents making the maximum rate a GEM can stand equal to 5 $\times 10^8$ Hz/cm^2. At this rate the detector is completely inefficient. In fact the efficiency begins to drop before this value.

The rate capability of the detector with a gain of 2×10^4 was measured by studying the ratio (pad current)/(X-ray rate) as a function of the X-ray rate (Fig. 4.11). A good stability was found up to about a rate of 10^7 Hz/cm^2 showing a very high rate capability.

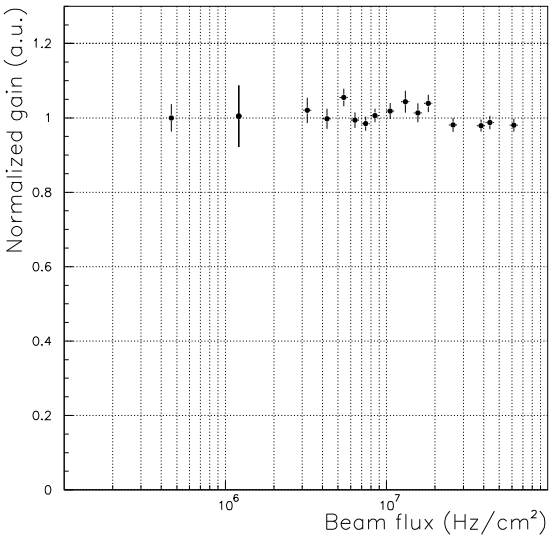

Figure 4.11: Normalized gain as a function of the X-ray flux. The stability shows a very good rate capability up to few 10^7 Hz/cm^2.

4.3.3 Ageing properties

The operation in a high particle rate environment can be very critical for the gas mixture filling the detector. During the avalanche development excited atoms are formed which can return to the ground state through a radiative process by emitting photons of few electronvolt energy. Photon mediated processes, as ,for example, photoelectron extraction, result very dangerous for stable detector operations. In general a fraction of polyatomic gas is added to the gas mixture in order to capture the emitted photons. The large amount of non-radiative states (rotational and vibrational) allows the absorption of photons in a wide energy range. This is a common properties of most organic compounds (e. g. hydrocarbons and alcohols) and of several inorganic compounds like freons or CO_2. This molecules dissipate the excess of energy either by elastic collisions or by dissociation into simpler radicals. These radicals recombine either into simpler molecules (dissociation) or forming larger complexes (polymerization). The latters can deposit on cathodes and anodes and substantially modify the chamber operation. For example, if a thin polymer-layer of insulator develops on the cathode, positive ions deposit on the outer layer side. The dipole electric field can be so high as to extract electrons from the cathode and a regime of permanent discharge is in-

duced. This particular effect is called *Malter effect* [54]. The use of inorganic gas such as CO_2 would eliminate some of the ageing effect, but, however, radiation damage of carbon dioxide detector was observed [55]. Variations in the detector operation as the one described above are called *chamber ageing*.

In order to study the ageing of our detector a long test with high rate (50 MHz/cm^2) X-ray beam was performed. The spot size was about 1 cm^2 which means that about 5000 channels were illuminated.

The chamber was gas supplied with a flux of 100 cc/min of an $Ar/CO_2/CF_4$ (60/20/20) mixture. It was measured that this flux was enough to avoid effect of gas poisoning which can arise for a too low gas rechange. Polyamide pipes were used which do not ensure a complete water tightness. The fluoride present in the CF_4 and the hydrogen of the water may create fluoride acid (HF) which can etch the GEM copper layer resulting in an increase of ageing effects. The V_{tot} was 1230 V resulting a gain of about 2×10^4. In this configuration a 3-GEM in the region M1R1 would integrate a maximum charge of 13 C/cm^2 in 10 years of LHC.

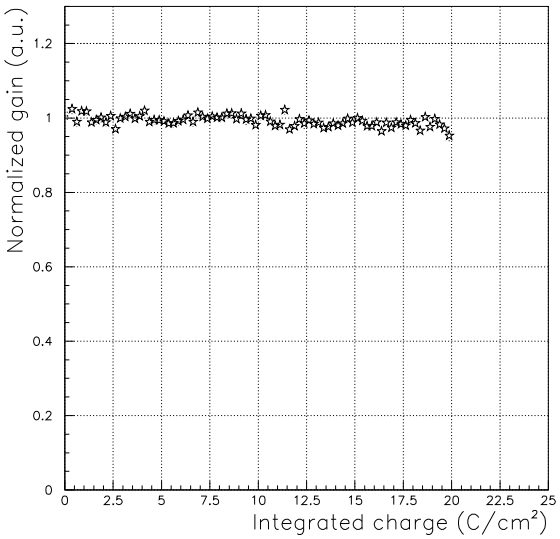

Figure 4.12: Normalized gain as a function of the charge integrated on the chamber anode.

The current measured on the pads was about 30 μA. After 10 days of test a total charge of 20 C/cm^2 was integrated on the detector pads. The behavior of the pad current during the test is shown in Fig. 4.12. Effects due to ambient pressure and temperature variations were corrected by using a

second, low irradiated, 3-GEM chamber as a monitor. Only a little variation (less than 5%) was found in the chamber gain allowing to conclude that no important ageing effects are expected inside the GEM channels during the chamber operation for 10 years of LHC.

4.4 Chamber efficiency and time performance

In parallel with the laboratory measurements, several beam tests were performed to study and optimize the detector total efficiency and time performance.

These items were deeply investigated as a function of several detector characteristics and the results will be shown and discussed in the following sections.

4.4.1 Measurements set-up

The scheme of the set-up used in the beam-tests is drawn in Fig. 4.13.

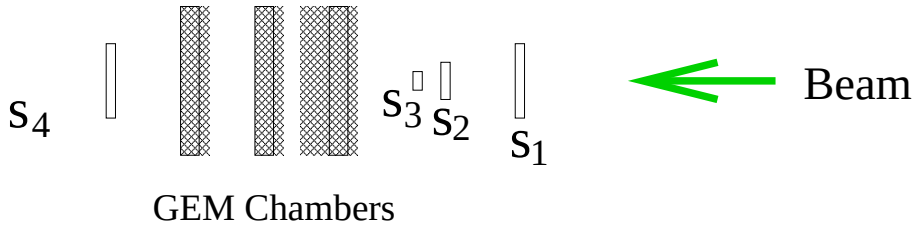

Figure 4.13: Schematic draw of the set-up used in the test beam.

The coincidence of scintillators S_1, S_2, S_3 and S_4 (with area respectively of 10×10 cm^2, 15×15 cm^2, 1×3 cm^2 and 3×1 cm^2) was used to give the trigger signal to the DAQ system. The S_1 and S_4 signals were also sent to a constant fraction discriminator. The coincidence of the discriminator outputs was delayed to give the common stop to the TDC.

The pad signals were discriminated and sent to a TDC. The response time of the chamber is defined by the signal crossing of a discriminator threshold. The high voltage to the different electrodes was supplied separately in order to explore all possible detector electric configurations.

In each configuration $5 \cdot 10^4$ events were acquired.

4.4.2 Total efficiency studies

The first parameter studied was the efficiency in detecting minimum ionizing particles. As we found in the section 4.1.1 a 3 mm wide drift gap ensures to have at least 5 clusters created. With an adequate detector gain and electron transparency this leads to a very efficient chamber. We measured the total efficiency at the CERN PS with a $3 \div 4$ GeV π^- beam. The efficiency as a

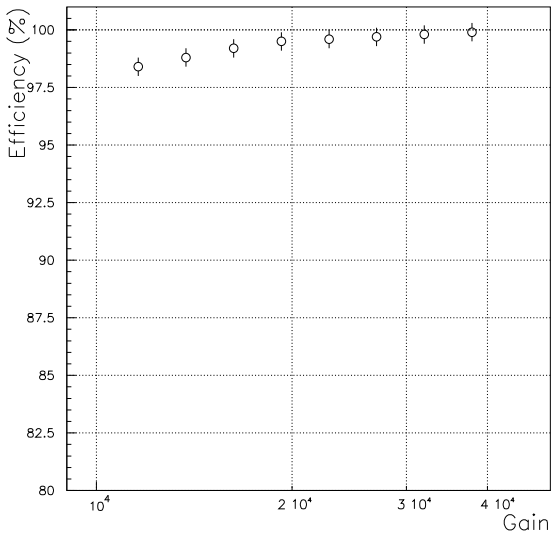

Figure 4.14: 3-GEM chamber detection efficiency as a function of the gain as measured during a beam test with an $Ar/CO_2/CF_4$ (60/20/20) mixture.

function of the detector gain is shown in Fig. 4.14. The total efficiency is above the 99% for a total gain of the order of 10^4.

4.4.3 The time performance

The main request for triggering in LHC experiments is to provide a high efficiency in the bunch-crossing time-window (25 ns). Thus, beside to a high overall efficiency, the detectors should ensure a good time performance. The time performance of the chamber is related to the statistics of the clusterization in the drift gap. The general expression for the probability-distribution of the distance x from the first GEM of the creation point for the cluster j, is [40]:

$$A_j^{\bar{n}}(x) = \frac{x^{j-1}}{(j-1)!}\bar{n}^j e^{-\bar{n}x} \tag{4.5}$$

where $\bar{n}$ is the average number of cluster created per unit length. Knowing the drift velocity in the drift gap v_d, the probability-distribution of the arrival times on the first GEM for the cluster j results:

$$P_j(t_d) = v_d \cdot A_j^{\bar{n}}(v_d t_d) \tag{4.6}$$

In particular, for the first cluster (the one produced closer to the first GEM):

$$P_1(t_d) = v_d \cdot \bar{n} e^{-\bar{n} v_d t_d} \quad \text{and} \quad \sigma_1(t_d) = 1/\bar{n} v_d \tag{4.7}$$

This gives the intrinsic value for the time resolution of a GEM-based detector if the first cluster is always detected. This value depends only on the gas mixture properties and, for example, for the $Ar/CO_2/CF_4$ (60/20/20) is $\sigma_1(t_d) = 2.2$ ns. As we have seen in section 4.2.2, the signal is given by the convolution of the currents induced by the motion, in the induction gap, of the electron clouds due to the different clusters released in the drift gap by a track. Due to the statistical fluctuations of the detector gain and of the electron transparency, it could happen that the signal induced by the first cluster cannot be discriminated. In this case the second cluster is needed to make the signal go above the threshold. When also with the second cluster contribution the signal is not high enough, the third is needed and so on. This effect is the main cause of the deterioration of the detector time resolution. In order to avoid this effect or to reduce its impact, it is necessary:

- *to increase the single electron detection capability*: the electron transparency and the overall detector gain can be adjusted by optimizing the chamber electrical configuration.
- *to reduce the time distance between the clusters and the statistical fluctuations* $\sigma_j(t_d)$: from the equation 4.6 these two parameters behave, for all clusters, as the term $1/nv_d$. Thus, the choice of a *fast* and *high yield* gas mixture should help in optimising the detector time response.

Chamber electric optimization

We studied the efficiency in a 25 ns (ϵ_{25}) window as a function of the electric fields in the drift gap (Fig. 4.15 (a)) and in the transfer gap (Fig. 4.15

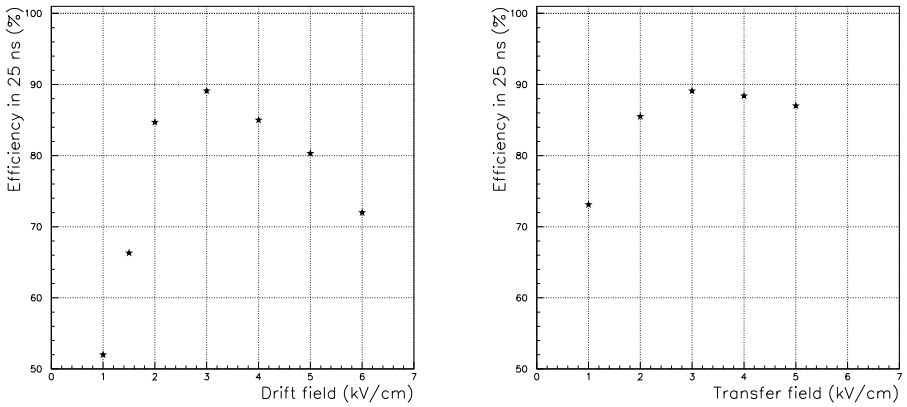

(a) (b)

Figure 4.15: Chamber efficiency in a 25 ns time window as a function of: the drift field (a) and the transfer field (b).

(b)). In both cases we found losses in the time performance for electric field giving a poor electron transparency. The results suggested, as it was expected from the transparency studies, to work with E_d, E_{t1} and E_{t2} in the range 3 $\rightarrow$ 4 kV/cm.

The gain has a large impact on the single electron detection capability. A high average gain reduces the probability that statistical fluctuations of the amplifications give underthreshold signal and allows to reach very high effinciency in a 25 ns time window as shown in Fig. 4.16 for the $Ar/CO_2/CF_4$ (60/20/20) mixture.

The gas mixture studies

In order to improve the time performance of the chamber a detailed study on the time response for different gas mixtures was performed. We started our tests with an Ar/CO_2 (70/30) mixture, very widely used, which shows:

- a high gain (see Fig. 4.10);
- a drift velocity for an electric field of 3 kV/cm of 70 μm/ns (Fig. 4.17 (a));
- a specific clusterization of $\bar{n}$=12 clusters/3mm resulting in a $\sigma_1(t_d)$=3.5 ns (Fig. 4.17 (b));

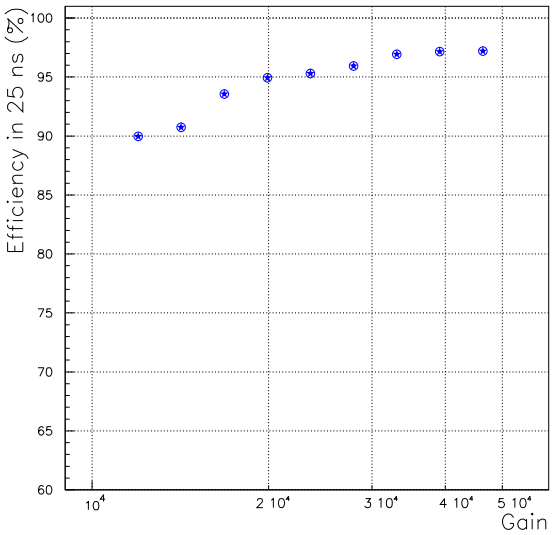

Figure 4.16: Chamber efficiency in a 25 ns time window as a function of the overall gain with an $Ar/CO_2/CF_4$ (60/20/20) mixture.

In Fig. 4.18 (a) the time spectrum obtained with a gain of $7 \cdot 10^4$ is shown. The distribution RMS is about 10 ns resulting in a ϵ_{25} of about 88% (see Fig. 4.19).

In order to improve the chamber time performance some CF_4 was added to the mixture. The pure CF_4 has a very high drift velocity and a very high specific clusterization:

$$v_d = 130\ \mu\text{m/ns at 3 kV/cm and } \bar{n} = 25\text{clusters/3mm} \rightarrow \sigma_1(t_d) = 1.5\ \text{ns}$$

The first mixture studied was a $Ar/CO_2/CF_4$ 60/20/20. In this case $\sigma_1(t_d)$=2.2 ns. The time spectrum obtained with a gain of $2 \cdot 10^4$ is shown in Fig 4.18 (b) and has an RMS of about 6 ns and the ϵ_{25} is 96 % (see Fig. 4.19). This gas mixture represented a great progress in the chamber time performance and has been the standard one for many of our measurements. For new improvements we had interesting results with two other mixtures:

- $Ar/CO_2/CF_4$ (45/15/40);
- $Ar/CF_4/\text{Iso-}C_4H_{10}$ (65/28/7);

As the term $1/nv_d$ for these gas mixtures is about the same at 3 kV/cm (1,75 ns as shown in Fig. 4.17), they were supposed to give the same time

performance. Because of its high gain (Fig. 4.10), the isobutane based mixture allows to work at moderate V_{tot}, while it may suffer for long term ageing effect. On the other hand a large amount of CF_4 reduces the gain (Fig. 4.10), but provides high drift velocity and high specific clusterization. The time spectra obtained with these two mixtures are quite similar (Fig. 4.17 (c) and (d)). In both distributions the RMS is about 4.5 ns and ϵ_{25} is 98 %. In Fig. 4.19 the ϵ_{25} for the four mixtures are compared as a

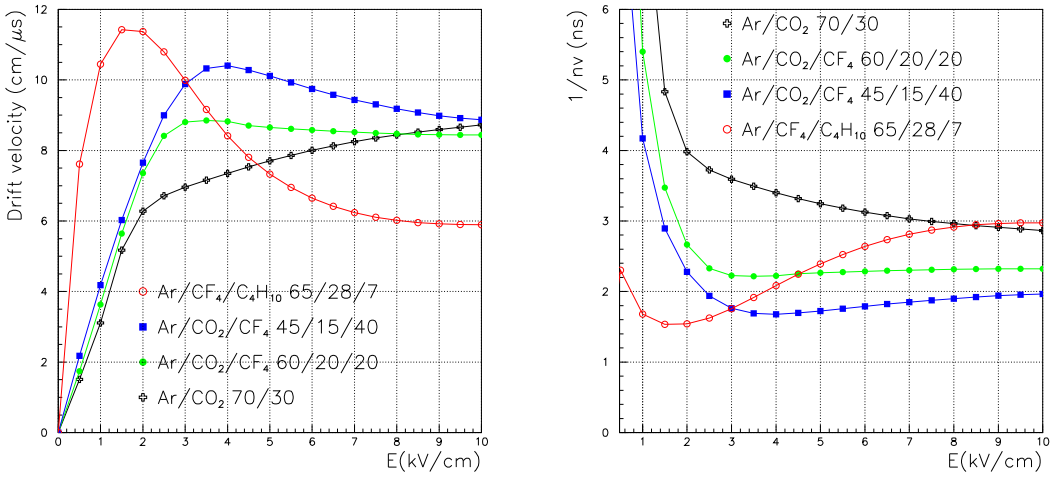

(a) (b)

Figure 4.17: (a): The computed electron drift velocity for the gas mixture tested. (b): The 1/nv term for the gas mixture tested.

function of the detector gain. Having optimized the detector electron transparency, for a fixed gas mixture the time performance is a function of the gain. Fig. 4.19 demonstrates that the asymptotic value of ϵ_{25} is a function of the gas properties:

- for a slow and low yield mixture (Ar/CO_2 70/30 for example), even at very high gain, ϵ_{25} is lower than 90 %;
- for a fast and high ionizing gas mixture an ϵ_{25} of 98 % can be reached at moderate gain values.

4.4.4 The bi-GEM effect

As a charged particle crosses the detector, ionization is produced all along the track. Due to statistical fluctuations of the amount of primary charge or

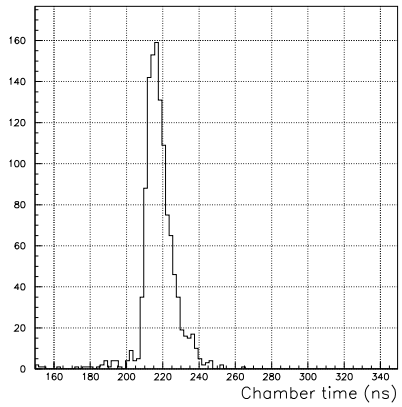

a: Ar/CO_2 70/30

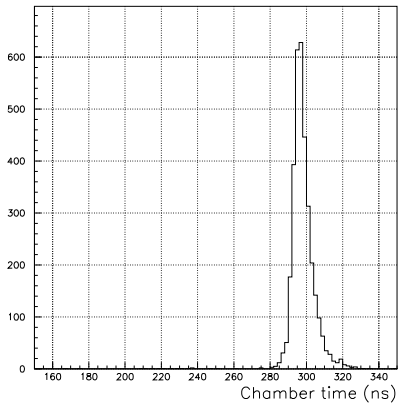

b: $Ar/CO_2/CF_4$ (60/20/20)

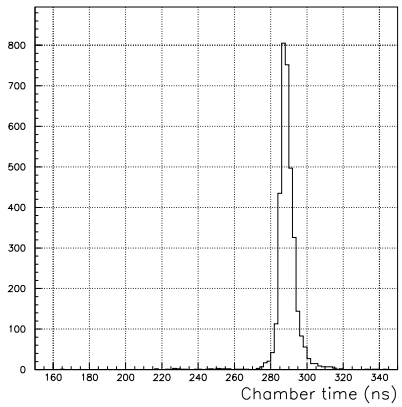

c: $Ar/CF_4/C_4H_{10}$ (65/28/7)

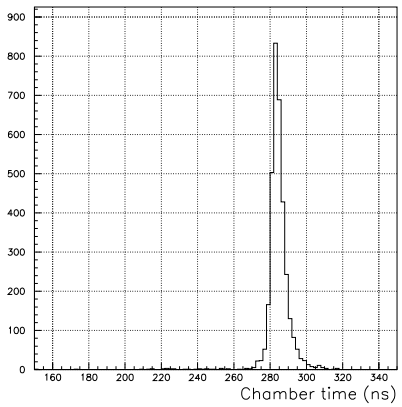

d: $Ar/CO_2/CF_4$ (45/15/40)

Figure 4.18: TDC spectra with different gas mixtures.

of the GEM gain, the ionization produced in the first transfer gap, multiplied only by the last two GEM, can induce on the pads a signal large enough to be discriminated. This signal is called *bi-GEM signal*.

The electron clouds produced by the multiplication of the clusters created in the first transfer gap have to cover only the second transfer gap before starting to induce the signal on the pads. Therefore these bi-GEM signals will be in advance with respect to the signals produced by electrons coming from the drift gap.

In Fig. 4.20 (top) the TDC spectrum obtained with V_{gem1}=430 V and V_{gem2}=V_{gem3}=390 V is shown. The spectrum obtained with V_{gem1}=0 and V_{gem2}=V_{gem3}=390 V (the bi-GEM spectrum) is superimposed in black. In

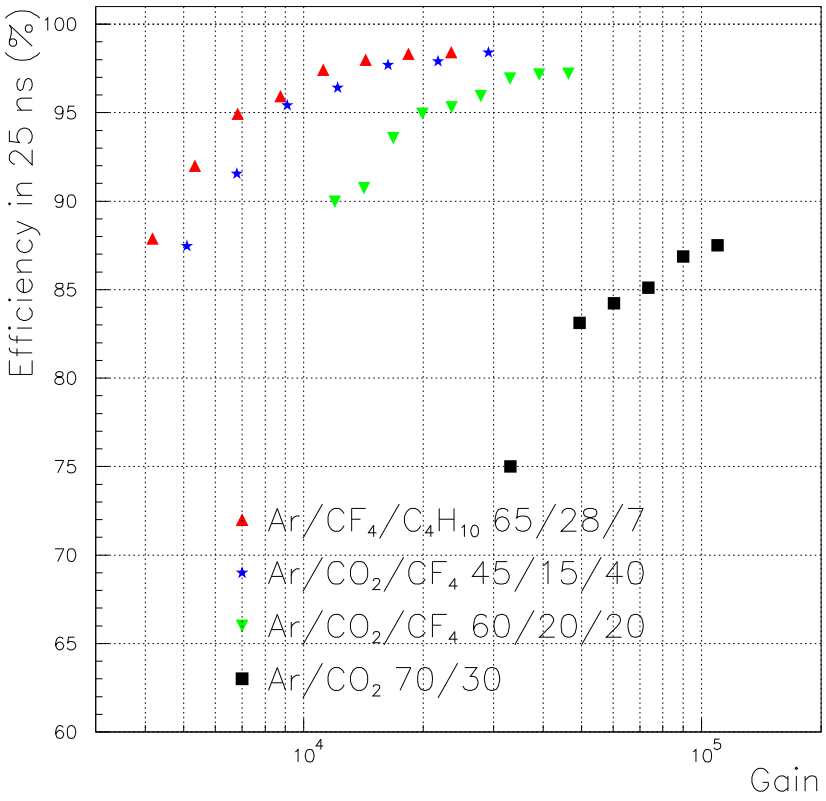

Figure 4.19: Chamber efficiency in a 25 ns time window as a function of the gain for the 4 gas mixtures studied.

both cases a detector with d_1=2 mm was used. The bi-GEM hits arrive with an advance of about 20 ns and they represent the 2% of the total number of events.

In order to reduce the bi-GEM effect, the detector geometry was changed. The first transfer gap thickness was reduced to 1 mm to halve the time advance of the bi-GEM hits and the average amount of primary charge created. The rate of the bi-GEM events was expected to decrease. In Fig. 4.20 (b) the same spectra as in Fig. 4.20 (a) are shown as obtained with d_1=1 mm. The time advance of the bi-GEM events in results reduced to 10 ns. Moreover the bi-GEM events are less than 1 % of the total.

The impact of the bi-GEM effect is largely reabsorbed. This suggested that the thickness of the first transfer gap has to be as low as possible. We

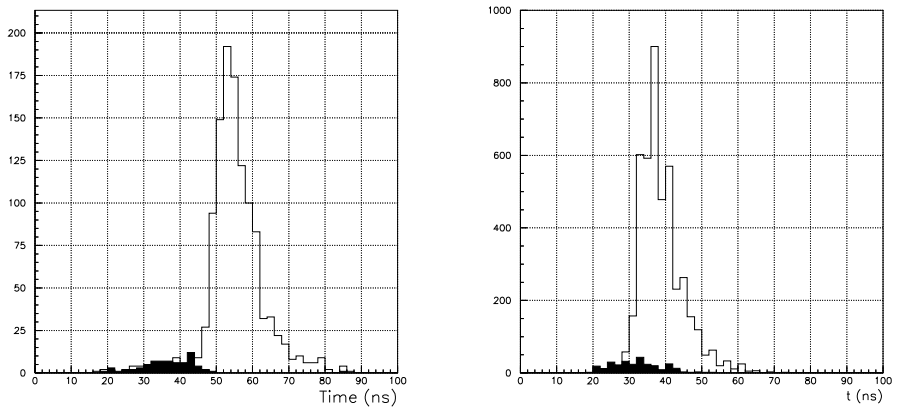

(a) (b)

Figure 4.20: The bi-GEM effect with a 2 mm transfer-gap 1 (a) and with 1 mm gap (b).

fixed the d_1 value to 1 mm.

4.4.5 Conclusions on time performance

A lot of work has been performed on detector efficiency and time performance optimization:

1. the electron transparency was optimized by adjusting the drift and the transfer fields which have been studied both with X-rays and test beams;

2. the detector geometry was chosen to reduce as possible the bi-GEM effect;

3. different gas mixtures were investigated in order to improve the time resolution;

After several tests a very good time response was achieved providing ϵ_{25} of about 98 %.

4.5 Detector charge spectra

The total charge spectra were computed, in the simulation, convoluting the gain distributions of three single GEM (as the one in Fig. 3.16) with the

cluster production distribution. The total number of electrons reaching the induction gap is given by

$$n_{tot} = (\Sigma_{i=1}^{npair} g_i^{(1)}) \cdot g^{(2)} \cdot g^{(3)} \tag{4.8}$$

where *npair* is the number of single electrons in the different clusters as evaluated by the Heed program [36] and $g^{(k)}$ is a value randomly extracted from the gain distribution for the kth GEM.

In the 4.8 for the first GEM a different gain is assigned to each primary electron of a cluster. In the following GEM, due to the large number ($\simeq 30$) of secondary electrons leaving the first GEM, the gain was not calculated for each electron, but the whole electron cloud was multiplied by an average gain value.

Using the Ramo theorem (see 4.1.4), we evaluated the induced current on the pads which was then convoluted with the electronics response (see 4.2.1). This allowed us to simulate the charge spectra as seen by an ADC (Fig. 4.21 (a)).

We acquired experimental detector charge spectra for minimum ionizing particles as a function of V_{tot} using an ADC with 50 fC/count sensitivity and a 200 ns gate (Fig. 4.21 (b)).

The average values of the charge spectra simulated were found to be lower than the experimental ones; this effect has also be seen by other authors [**?**]. In the whole range $V_{tot} = 1200\ V \rightarrow 1250\ V$ a factor 3 was used to adjust the total gain.

After the recalibration, a very good agreement between simulation and experimental data was achieved. The charge spectra obtained with V_{tot}= 1220 V are shown in Fig. 4.21. In Fig. 4.22 the positions of the peaks of the total charge spectra simulated are compared with the experimental ones. It is possible to see how, after the "recalibration", a good agreement was found in the whole range $V_{tot} = 1200\ V \rightarrow 1250\ V$.

4.6 Discharge studies

The energy loss (ΔE) of a charged track in a thin gas sample can be described by the Landau distribution which is analytically approximated by:

$$f(\lambda) = 1/\sqrt{2\pi} e^{1/2(\lambda + e^{-\lambda})} \tag{4.9}$$

where $\lambda = (\Delta E - \Delta E_{mp})/\xi$ and $\xi = (Z\rho d)/(A\beta^2 X_0)$, d being the gas sample thickness. ΔE_{mp} is the most probable energy loss given by the first term in the Bethe and Bloch formula. In Fig. 4.23 the characteristic shape of the Landau distribution with ΔE_{mp}=300 is shown. The long tail in the energy

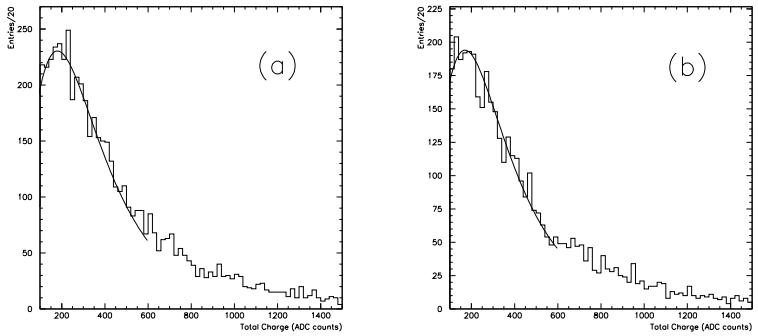

Figure 4.21: Experimental (a) and simulated (b) detector total charge spectra.

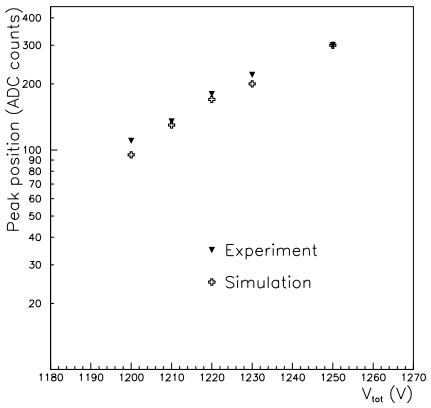

Figure 4.22: Position of the Landau distribution peaks from experimental data and simulation.

loss values allows to have a large amount of pairs created in the gas. In these events, the charge amount in the GEM channels may become huge. When a large amount of ions and electrons migrate towards the respective electrodes, they can screen completely the external electric field in a region and the charges can recombine by emitting photons having the energy for ionizing other gas atoms. A lot of free charges can be created providing a conductive channel in the gas. This process is called *streamer formation*. A phenomenological study shows that a streamer occurs when the charge amount in the avalanche becomes greater than the Raether limit: 10^8 electrons [44]. The conductive channel acts as a short circuit between the two copper sides of the GEM. Therefore the whole amount of charge accumulated on the GEM and the electrical field in the channels drop to zero.

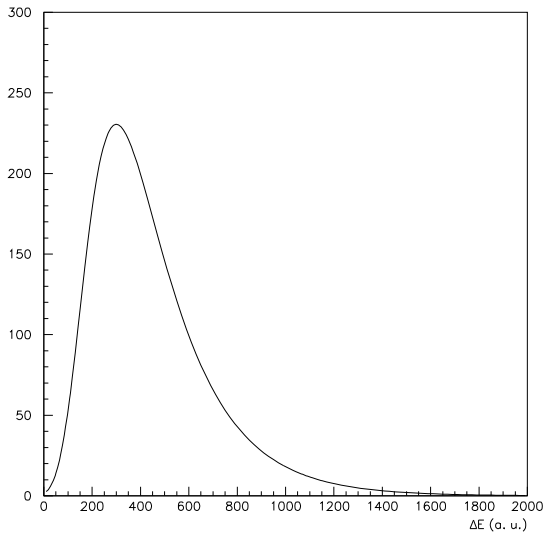

Figure 4.23: Typical Landau's distribution.

This process is called *discharge* and has been investigated in order to understand:

- how is it possible to reduce the discharge probability;
- how many discharges a GEM detector can stand without any damage or ageing effects.

It is usually defined *discharge probability per incident particle* as n_d/N_p where N_p is the number of particle crossed the detector causing n_d discharge.

4.6.1 The diffusion effect

While trying to reduce the discharge probability very interesting results were found in studying the positive contribution of the charge diffusion in the gas. Without the diffusion effect, due to the GEM amplifications, the charge amount in the channels would rapidly increase by passing from a GEM to the following one. We recall that the gain distributions (as the one in Fig. 3.16) show tails proportional to their mean values. Therefore, fluctuations are larger where the gain is larger.

In this situation, to minimize the discharge probability, one would have to set $V_{gem1} > V_{gem2} > V_{gem3}$ in order to have less gain fluctuations where the charge amount is higher.

GEM	e^- cloud radius	e^- entering	e^- produced
1	1	1	$Ae^{\alpha V_{gem1}}$
2	βd_1	$Ae^{\alpha V_{gem1}}$	$A^2 e^{\alpha V_{gem1}+V_{gem2}}$
3	$\beta^2 d_1 d_2$	$A^2 e^{\alpha V_{gem1}+V_{gem2}}$	$A^3 e^{\alpha V_{gem1}+V_{gem2}+V_{gem3}}$

Table 4.2: Number of channels involved, e^- entering and exiting for the 3 GEM in a chamber.

Let now take into account the effect of the diffusion. During the transfer between two following GEM, the electrons in the clouds diffuse because of the scattering with the gas molecules. Since the transverse dimension of the electron clouds increase as the square root of the path covered [40], the number of channels involved in the multiplication process rises linearly with the distance when passing from a GEM to the following one. Thus, if on one hand the number of electrons increases due to gain, on the other one the diffusion effect can help by spreading the charge. The probability to reach the Raether limit in each single channel results reduced.

We can evaluate how to distribute the gain among the GEM in order to minimize the discharge probability. The simplest condition is to have in each GEM the same charge amount per channel and keep it far from the Raether limit. If one electron enters a channel of the first GEM, after the multiplication an amount of $Ae^{\alpha V_{gem1}}$ will leave the channel. Let β be the scale factor between the path covered and the electron cloud radius. The electron cloud entering the second GEM will have a radius βd_1. In this way it is possible to calculate the number of channels involved and the number of electrons entering and exiting for all the GEM in the chamber. The results are shown in table 4.2.

For a fixed V_{tot} value, the condition to have in each channel of the various GEM the same amount of electrons is verified when:

$$e^{\alpha(V_{gem3}-V_{gem2})} = \frac{d_2}{d_1}$$

This means that, once the V_{tot} value is chosen, if $d_2 > d_1$, the discharge probability is minimized by the diffusion effect if $V_{gem3} > V_{gem2}$.

4.6.2 Test with α particles

In order to check the validity of our theory on the diffusion effect, we made some tests in laboratory. The detector discharges were monitored by acquir-

ing the currents on the detector pads. When a discharge occurs a recharge process is needed.

In Fig. 4.24 the pad current of a chamber illuminated with an α source is shown. The discharge is seen as a drop of the pad current, which disappears after the recharge process. Because of their high ionizing power the α particles are very usefull to trigger and then to study discharging phenomena. The α particles were produced in the drift gap by a radioactive source. We used an $Ar/CO_2/CF_4$ (60/20/20) mixture.

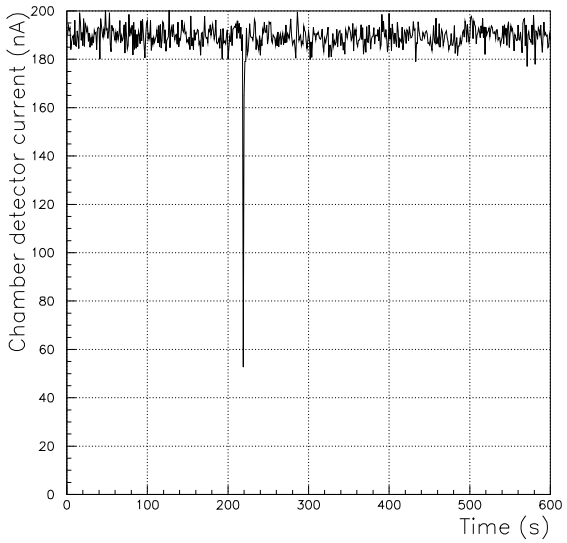

Figure 4.24: The monitored current on the detector pads.

The discharge probability of a detector irradiated with an α source was studied as a function of the gain in two different electric configurations:

- $V_{gem1} > V_{gem2} > V_{gem3}$ which minimise the discharge probability if no positive effect from the diffusion is expected;
- $V_{gem1} > V_{gem3} > V_{gem2}$ the configuration found to minimising the discharge probability if the diffusion effect is taken into account;

The results obtained are shown in Fig. 4.25. The configuration $V_{gem1} > V_{gem3} > V_{gem2}$ shows a discharge probability lower, of about one order of magnitude, with respect to the case $V_{gem1} > V_{gem2} > V_{gem3}$ in the whole explored range. In particular the difference increase for a gain lower than 10^5.

These results indicate the really positive effect of the charge spreading due to the charge diffusion in the gas on the discharge prevention.

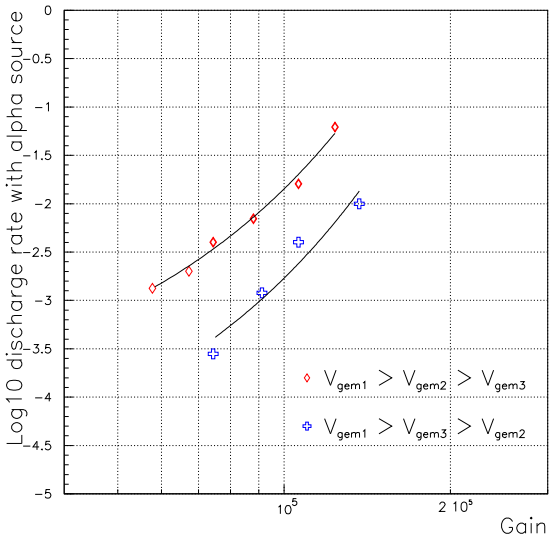

Figure 4.25: The discharge rate of a 3-GEM detector irradiated with an α source in two different GEM voltage supply configurations.

4.6.3 Test at the Paul Scherrer Institute

After the encouraging results on the discharge probability suppression by means of the diffusion effect two chambers have been built and tested on the high intensity hadron beam at the Paul Scherrer Institute (PSI). In order to amplificate the diffusion effect, while one chamber had the standard gap thickness 3/1/2/1 (chamber A) the other one was built with a very wide second transfer gap 3/1/7/1 (chamber B).

4.6.4 The set-up

The experimental set-up was quite similar to the one shown in Fig. 4.13. The scintillator counters were used, in this case, to evaluate the beam intensity, size and position. The current supplied to the detector by the high voltage device was acquired in order to monitor the discharge rate.

4.6.5 The πM1 beam

The tests were performed in the πM1 experimental area. The beam at PSI is a quasi continuous beam with 19 ns time separation between two particle bunches. In our experimental area, the beam was composed by protons (the

main part) and pions of 350 MeV/c momentum. At these energies protons lose 5 times more energy by ionization than pions. By inserting 1 mm thick aluminum radiator along the beam line, it was then possible to separate, after a magnetic dipole, the two beam components. We choose to work with the π^+.

In order to evaluate the contamination of protons still present, we studied the counting rate of a scintillator detector as a function of the discriminator threshold (Fig. 4.26). A plateau was found for threshold values between 150 and 200 mV. From the ratio between the rate at the plateau and the total rate, a proton contamination of about 7 % was estimated.

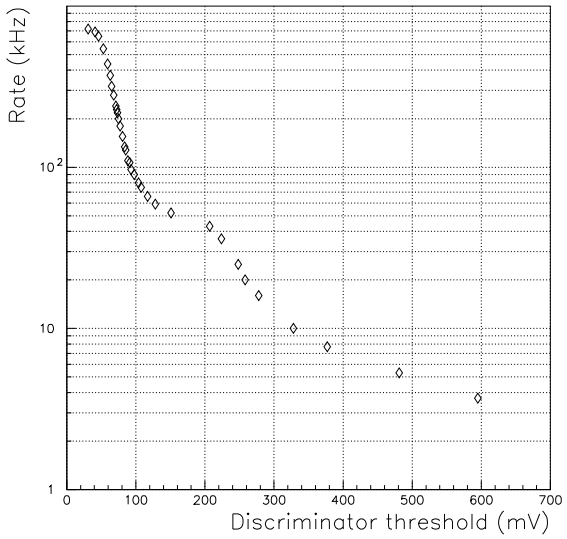

Figure 4.26: The scintillator counting rate as a funtion of the threshold. The presence of a plateau indicates the proton contamination estimated to be about 7 %.

The scintillator counters became completely inefficient when illuminated with the high rate beam. In order to evaluate the effective beam rate on a 2×2 cm^2 area, we measured the scintillator coincidence counting rate and the current on the GEM detector pads as a function of the beam slit opening. With almost closed slits, we measured the scale factor between the GEM detector current and the counting rate (Fig. 4.27 (a)). This scale factor was then used to translate the current measured with wide opened slits in the effective rate on a 2×2 cm^2 area (Fig. 4.27 (b)) which was evaluated to be 100 MHz.

We also studied the beam profile, by moving the scintillator with respect to the beam line. The transversal sizes of the beam were found to be 3 $\times$ 5 cm^2 FWHM from which we estimated a total rate on the detector of about 300 MHz.

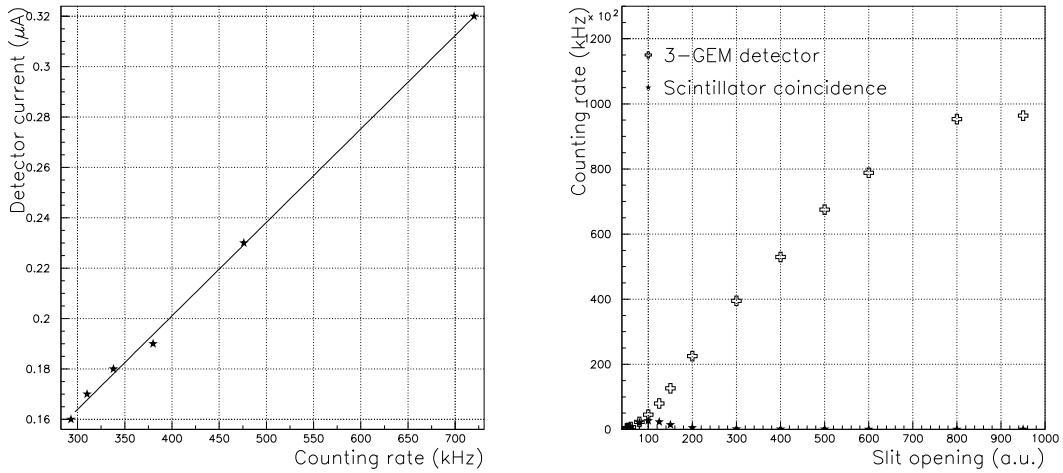

(a) (b)

Figure 4.27: (a): The 3-GEM detector current as a function of the counting rate. (b): The rescaled 3-GEM detector counting rate as a function of the beam slit opening.

4.6.6 The measurements

As described in section 4.6.2 the electrode currents were acquired in order to monitor the discharges. Since the high voltage supply was set to provide a maximum current of 50 μA in each channel and the total charge on the GEM is about 5 μC, the recharging time resulted about 100 ms. In Fig. 4.28 an example of data acquired is shown. The current decrease, observed in all electrodes, in the interval 90 s $\rightarrow$ 110 s is due to a beam current drop as can seen in the diagram on the bottom. The discharges appear:

- On the GEM electrodes as a positive spikes which represent the sudden increase of current needed to the recharging;
- On the pads as a drop of current due to the momentary gain drop.

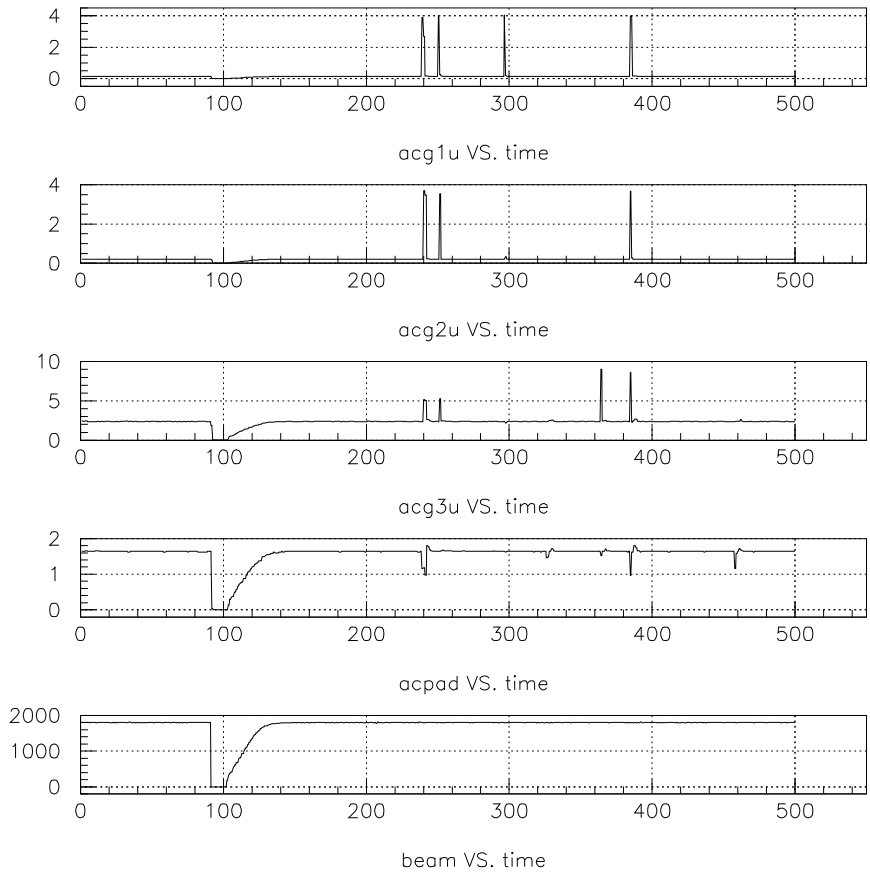

Figure 4.28: Example of current behaviors in the chamber electrodes.

It can be noticed that sometimes the discharges can propagate through the whole detector as shown in Fig. 4.28 at a time of 385 s.

For both detectors A and B we measured the discharge probability as a function of the overall gain with 3 different gas mixtures. Taking into account the results of tests with α particles, we chose a configuration with $V_{gem1} > V_{gem3} > V_{gem2}$.

4.6.7 Results

The measured discharge probability per incident particle are shown for the 3 different mixtures as a function of the gain in Fig. 4.29. In all cases it

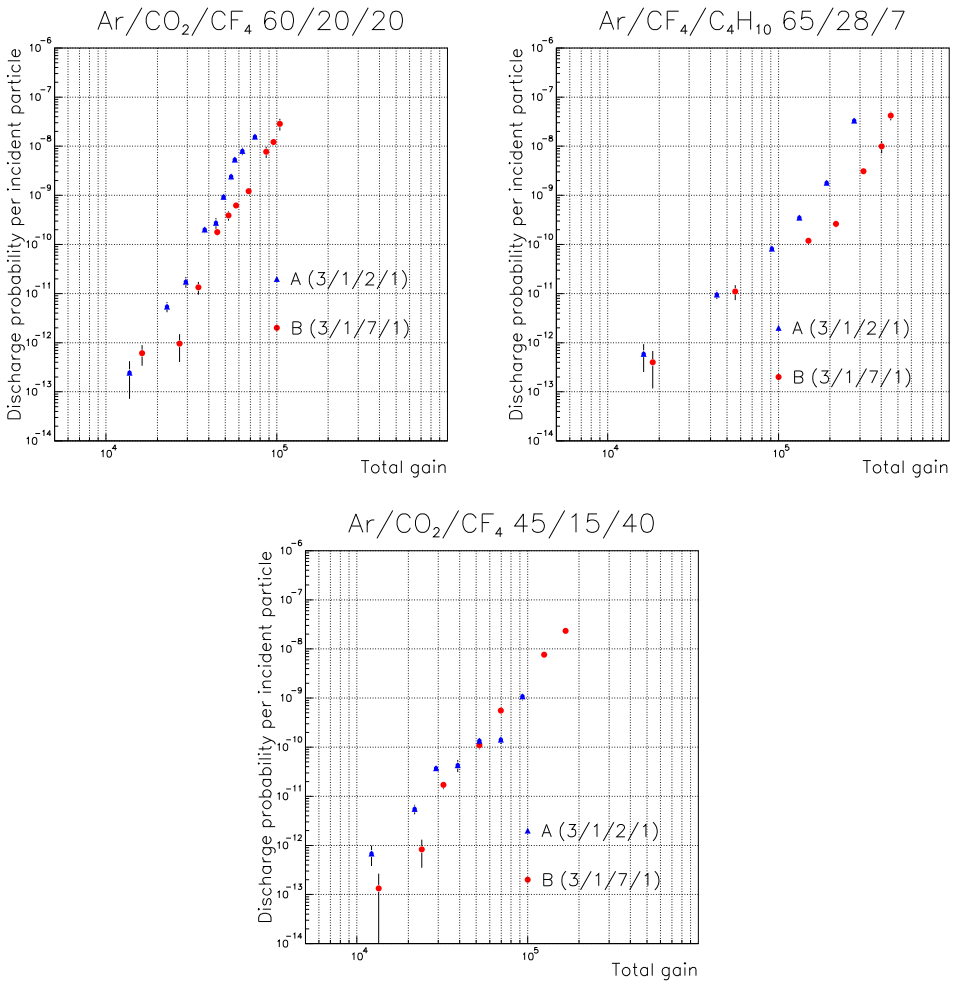

Figure 4.29: The discharge probability per incident particle.

seems that chamber B has a reduced discharge probability with respect to the chamber A. This indicates that the wide gap, by exploiting the diffusion effect, contributes in reducing the discharge probability. The gas mixture has also an important impact. In Fig 4.30 we report the discharge probability for the chamber B as a function of the gain for the three different gas mixtures.

The discharge probabilities for the $Ar/CO_2/CF_4$ based mixtures have almost the same dependence on the gain. In both cases for a gain of 10^5 the discharge probability reach a value of 10^{-8} per incident particle. In fact, it seems that the mixure with larger amount of CF_4 shows a little reduction in the discharge probability with respect to the other one. This could be

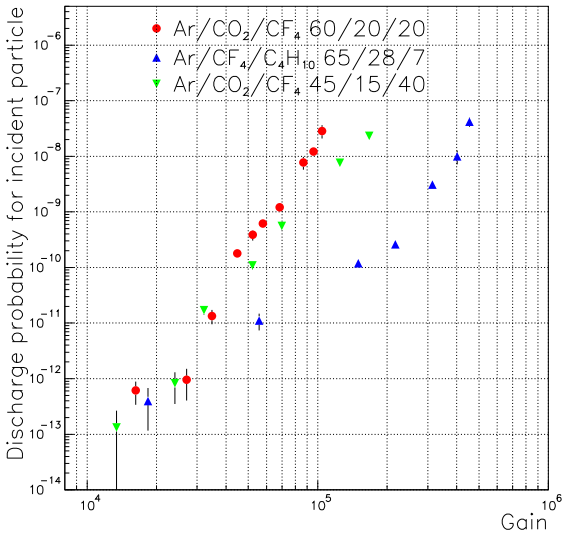

Figure 4.30: The discharge probability per incident particle for the chamber B as a function of the gain.

explained taking into account the large attachment coefficient of the CF_4.

For the isobutane based mixture the discharge probability increases slowly with the chamber gain because of the high absorption power of the isobutane especially for the 11.6 eV photons emitted by the Argon. In particular for a gain of 10^5 the discharge probability per incident particle is of the order of 10^{-10}.

4.7 The pad-cluster size

The average number of pads giving an overthreshold signal per track is called *pad-cluster size*. There are different causes for having more than one pad fired:

- *Direct induction by collected electron clouds.*
  If a charged particle crosses the detector near the edge between two pads, the electron clouds are collected by the two pads and the induced signal is shared.

- *Cross induction by non-collected electron clouds.*
  Also in the case when the charges are completely collected by only one

pad, during the drift in the last gap they can induce a bi-polar signal on the neighbouring pads (Fig. 4.7). If the charge amount is high enough the negative part of the signal can be discriminated.

- *Capacitive coupling between pads or read-out electronics.*
  The signal on a pad can be induced on the neighbouring channels through capacitive coupling between the pads or between electronics channels on the read-out electronic board.

4.7.1 Measurements and results

During the test beam the distribution of the number of fired pads per track crossing (pad mutiplicity) was monitored. In Fig. 4.31 it is shown a typical distribution of the number of pads fired. The column at 1 indicates the

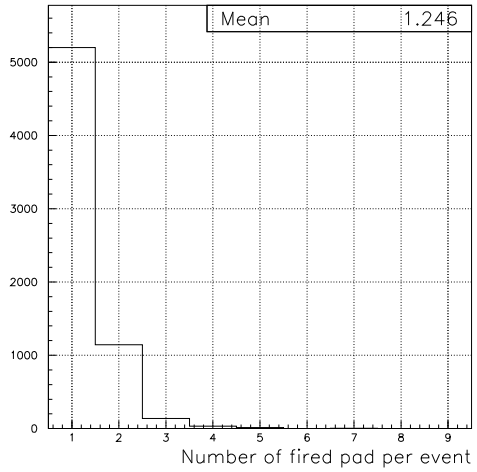

Figure 4.31: Distribution of the number of fired pads per event.

events with only one pad fired which represent the 80 % of all events. The probability to have a large number of pad with overthreshold signal is not negligible (e.g. 0.5 % to have 4 pads fired) and can be related to events with a large amount of created clusters which, once multiplied, induce signal on a very large area. In fact the pad multiplicity is a direct function of the charge within the detector and thus of the gain.

We studied the pad multiplicity as a function of the gain for the three gas mixtures (Fig. 4.32). The contribution due to pad and electronic capacitive coupling was studied on test bench. The pad capacitive coupling was found

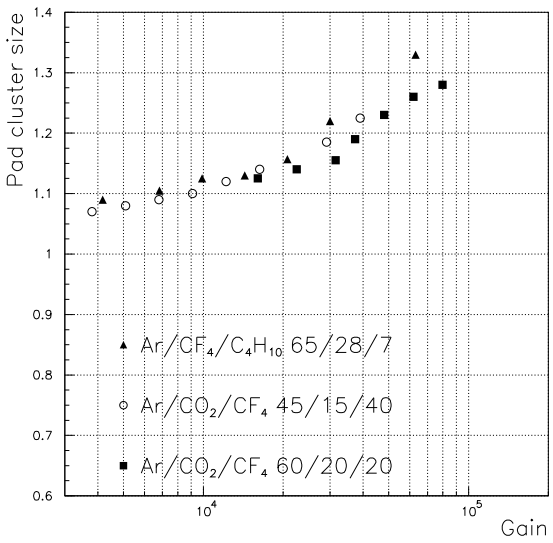

Figure 4.32: The pad cluster size as a function of the gain.

to be less the 1 %, while the board cross talk (see table 4.1) was about 5 %. These effects can explain why the cluster size for very low gains seems to be about 1.07. For high detector gains the $Ar/CO_2/CF_4$ gas mixtures show the same behavior. The cluster size is smaller than in the isobutane based mixture case. This can be explained by the high CF_4 attachment coefficient which in general squeezes the avalanches resulting in a better spatial resolution. Moreover, the isobutane based mixture has a high diffusion coefficient which spreads the electron clouds on a large area. Anyway for the three gas mixtures up to gains of the order $2 \div 3 \times 10^4$ the cluster size is found to be less than 1.2.

4.8 Conclusions

The measurements performed on triple-GEM chambers have given very interesting informations. Several detector prototypes were tested during more than two years of measurements without showing important behavior differences. The detector shows very high robustness and rate capability.

The geometry, the gas mixture and the electrical configuration were studied in order to optimize the detector efficiency and the time performance while minimizing the discharge probability per incident particle. In 25 ns

time window the detector reaches an efficiency larger than 98 % , while keeping the discharge probability per incident particle lower than 10^{-12}.

The pad cluster size was also measured finding values below 1.3 up to gain of the order of 10^5.

In the next chapter, all the results obtained will be compared with the LHCb muon system requirements in order to understand if this detector can be used in the regions M1R1 and M1R2.

Chapter 5

The triple-GEM detector for LHCb

In this chapter the results of the beam tests will be analyzed in order to understand if the triple-GEM detectors provide the performance requested for equipping the regions M1R1 and M1R2.

5.1 The final detector layout

The layout proposed for the GEM chambers presents some differences with respect to the tested prototypes.

1. *Detector geometry.*
   Large standard GEM foils having dimensions 20×24 cm^2 (as the one shown in Fig. 5.1) are used to reduce the total number of chambers minimizinf the overlap.

   Taking into account the results about the bi-gem effect and the discharge probability, we propose the following chamber geometry:

   - 3 mm wide drift gap;
   - 1 mm wide first transfer gap;
   - 7 mm wide second transfer gap;
   - 1 mm wide induction gap.

   The dimensions of the pads are 1×2.5 cm^2.

2. *Electrical configuration.*
   One of the copper sides of the large GEM is segmented in 6 electrically

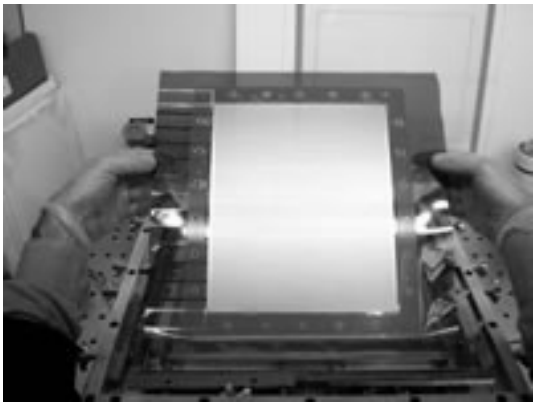

Figure 5.1: 20 $\times$24 cm^2 GEM before glueing on the frames.

indipendent sectors of 80 cm^2 area. The sector sizes were chosen in order to have the same area as the 10×10 cm^2 GEM. The sectors are supplied through a resistor chain as shown in Fig. 5.2. If a streamer

Figure 5.2: The resistor chain used to supply the different sectors.

occurs, only the sector involved will discharge while the other ones remain efficient. Separation of a GEM electrode in sectors not only reduces the inefficiency effect due to the discharges, but also limits the energy released during the discharge process. The electrostatic energy stored in a GEM sector is

$$E_{sect} = \frac{1}{2} C_{sect} \cdot V_{gem}^2$$

and thus, as the capacitance of a sector is about 1/6 of the total GEM capacitance, E_{sect}=(1/6) E_{gem}. The lower available energy should reduce the damages caused to the detector by the discharges.

The detector electrodes are no longer supplied by separate high voltage channels, but through a resistor voltage divider.

In order to optimize the detector transparency, we adopted the following values for the electric fields:

- 3 kV/cm for the drift field;
- 3 kV/cm for the transfer fields;
- 5 kV/cm for the induction field;

The configuration of the GEM voltage is $V_{gem1} > V_{gem3} > V_{gem2}$ in order to minimize the discharge probability.

5.2 The time performance

As we have seen in chapter 2, for redundancy reasons the five stations of the muon system will be made of two indipendent layers. The signals from each layer are discriminated and then logically OR-ed and passed to the trigger system. Each station has to ensure an efficiency larger than 99.0 % in a 25 ns time window.

We measured the time performance of a detector made by two OR-ed chambers. The results of these measurements for the three different gas mixtures as a function of the gain are shown in Fig. 5.3. As we measured studying the single-chamber, the $Ar/CO_2/CF_4$ (45/15/40) gives the best time performance, reaching an ϵ_{25} of 99.5 %. The $Ar/CO_2/CF_4$ (60/20/20) mixture has the lower drift velocity and this corresponds to the worst time performance. Even at high gains the efficiency in a 25 ns window is at most 99.0 %.

5.2.1 Ageing properties and discharge probability

The detector has to ensure a stable operation for 10 years in a very high particle flux. The maximum rate expected in M1R1 and M1R2 is $5 \cdot 10^5$ Hz/cm^2. This means that the chambers will integrate $5 \cdot 10^{13}$ particles and a total charge of about 13 C each cm^2. Is this detector able to survive?

From the point of view of the total integrated charge we have seen in section 4.3.3 that the detector shows a very good stability up to a total integrated charge of 20 C/cm^2 with an $Ar/CO_2/CF_4$ based mixture. The complex molecules of isobutane can give rise to problems of polymerization. For this reason, studies on the ageing caused by the $Ar/CF_4/C_4H_{10}$ (65/28/7) mixture are under way.

Because of the high particle rate, a high amount of discharges can occur and could deteriorate the detector performance. In order to evaluate the

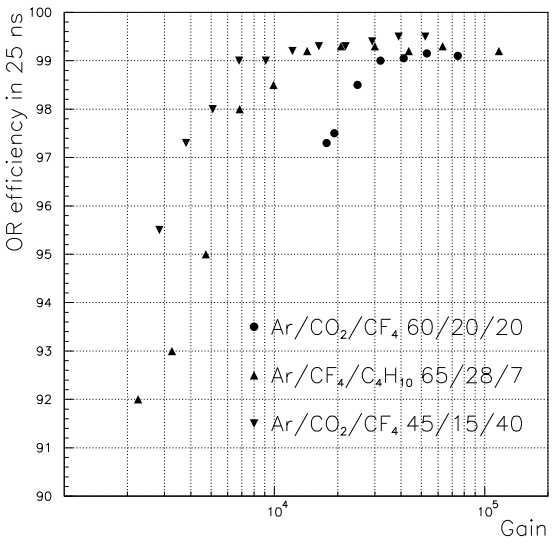

Figure 5.3: Efficiency of two chambers logically OR-ed in a 25 ns time window as a function of the gain.

maximum amount of discharges the detector can tolerate, we plan to make a long and "destructive" test. Anyway, we can extract some useful information considering the PSI test during which the chambers had both integrated about 5000 discharges. Most of the discharges occurred in configurations having a high V_{tot}. In this cases the energy released per discharge, proportional to V_{gem}^2, resulted higher than for the usual operation conditions. The discharge rate was very high as, for example, in Fig. 5.4 when about 100 discharges were integrated in 4000 seconds. Thus, the detectors operated in very demanding conditions. After the test in the high intensity beam, we measured the time performance of the chambers and we did not find any deterioration in the chamber behavior. We concluded that no damages or other ageing effects appeared even if the GEM chambers were operated in high voltage conditions. Thus, the amount of 5000 discharges seems to be a safe limit for proper detector operation. As the GEM sectors will be independent, a damage in a sector will not produce effect on the other ones. Thus, the chamber voltage configuration should ensure less than 5000 discharges per sector in ten years. Taken into account the maximum particle rate expected in M1R1 and M1R2, this means that the discharge probability has to be kept less than 10^{-12}.

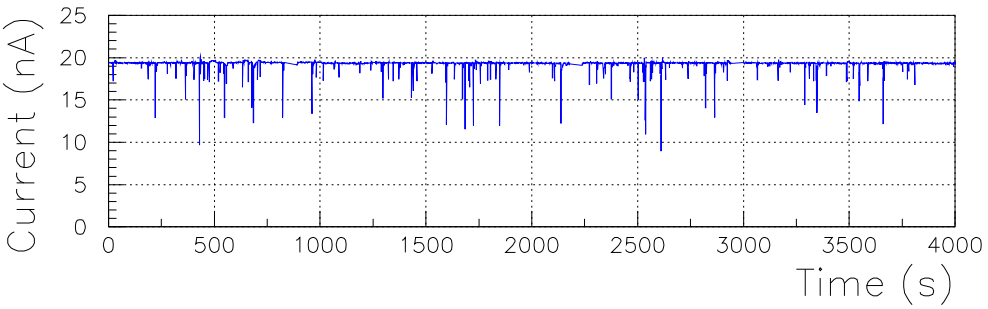

Figure 5.4: Current on the pads of a detector in high discharging conditions.

5.3 The working region

Once the detector electron transparency is optimized, the gain is the main parameter to control the detector efficiency, the time performance, the pad-cluster size and the discharge probability. We know that the chamber efficiency and the time performance improve while increasing the gain. On the other hand, the pad-cluster size and the discharge probability rise with the gain. As we have seen in section 3.2.3 the gain is essentially an exponential function of the sum of the 3 GEM voltage supplies (V_{tot}).

In order to be used in LHCb, the GEM detector should ensure a range of V_{tot} values where all the performances are within the experiment requirements. This range in V_{tot} is called *working region*.

We compared the results on the time performance with the discharge probabilities in order to visualize the different working regions for the three gas mixtures.

- *$Ar/CO_2/CF_4$ (60/20/20).*
  The discharge probability per incident particle becomes larger than the safe limit of 10^{-12} for a $V_{tot} = 1220$ V, as shown in Fig. 5.5. Unfortunately, the ϵ_{25} of two OR-ed chambers is 99 % for $V_{tot} = 1230$ V and then this gas mixture does not show any reasonable working region.

- *$Ar/CO_2/CF_4$ (45/15/40).*
  The value of $V_{tot} = 1315$ V gives a discharge probability of 10^{-12}. The beginning of the working region can be set at $V_{tot} = 1250$ V. This results in a 65 V wide working region as shown in Fig. 5.6.

- *$Ar/CF_4/C_4H_{10}$ (65/28/7).*
  This gas mixture provides both a good stability for the detector oper-

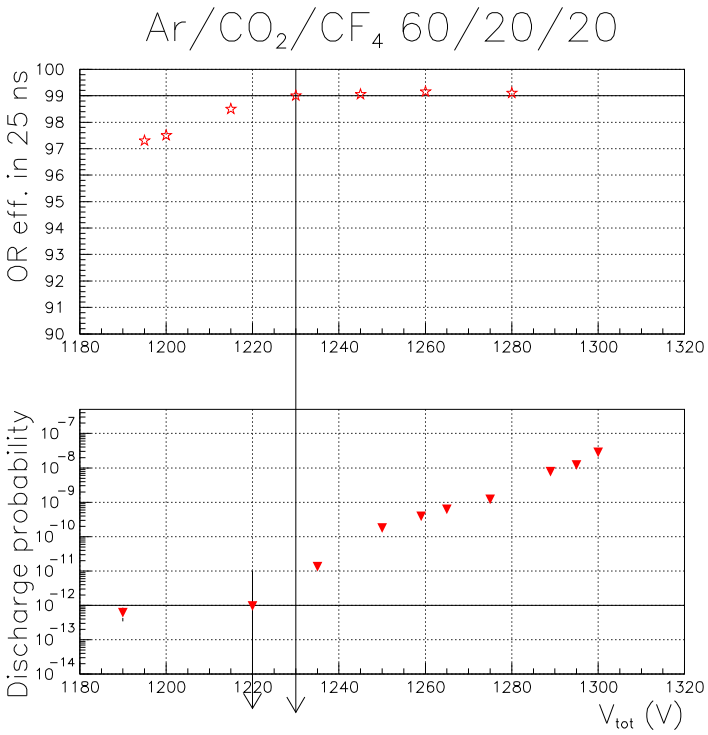

Figure 5.5: Discharge probability per incident particle as a function of V_{tot} for the $Ar/CO_2/CF_4$ (60/20/20) mixture.

ation and good time performance. We found a working region about 40 V wide (Fig. 5.7) from a V_{tot} = 1035 V up to a V_{tot} = 1075 V.

5.4 The pad-cluster size

As we have seen in chapter 2, the pad-cluster size is a very important parameter to keep under control. We studied the pad multiplicity as a function of V_{tot} in the working regions seen above. The pad-cluster sizes are below the value of 1.3, as shown in Fig. 5.8, for the three considered gas mixtures in the V_{tot} range studied.

The experiment requirements tolerate a maximum pad-cluster size of 1.20 in all muon stations. The pad multiplicity for the three gas mixtures results within this limit for the V_{tot} values ensuring a discharge probability less than 10^{-12} as shown in table 5.1.

In section 2.6.4 we have seen that a pad-cluster size higher than 1.15

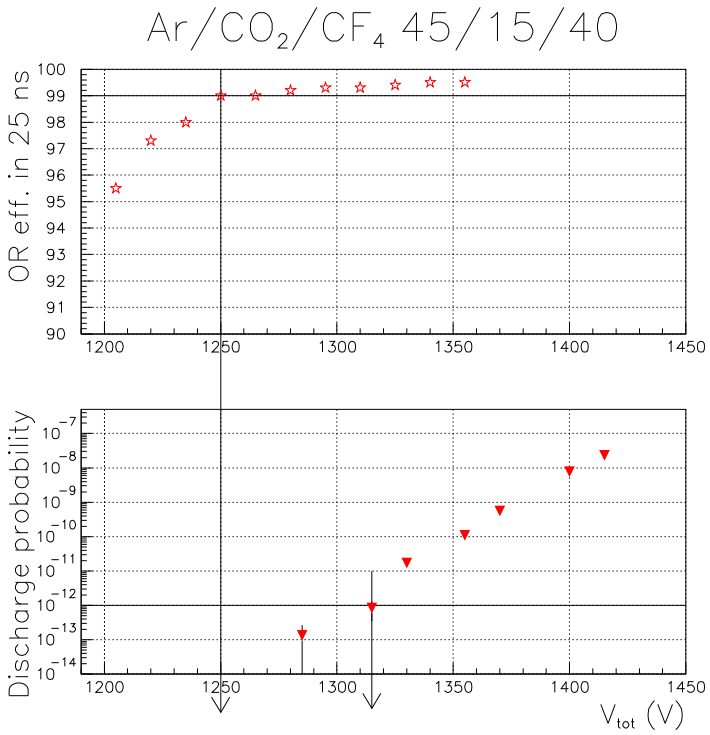

Figure 5.6: Discharge probability per incident particle as a function of V_{tot} for the $Ar/CO_2/CF_4$ (45/15/40) gas mixture.

implies a loss in the "signal" ($b \rightarrow \mu X$ rate) to "noise" (minimum bias rate) ratio of about 2 % with respect to the ideal situation with a pad-cluster size of 1.0.

For a detector filled with the $Ar/CO_2/CF_4$ (45/15/40) mixture the pad-cluster size is less than 1.17 in the whole working region and in particular less than 1.15 up to a $V_{tot} = 1300$ V which corresponds to about the 80 % of the working region.

5.5 Study of the chamber uniformity

In order to study the performance homogeneity as a function of the position inside the large chamber, we measured the total efficiency and the ϵ_{25} for different pads in the chamber.

The results are shown in Fig. 5.9. The pads having number in the range $13 \rightarrow 18$ were placed in correspondence of the edge of the GEM active area.

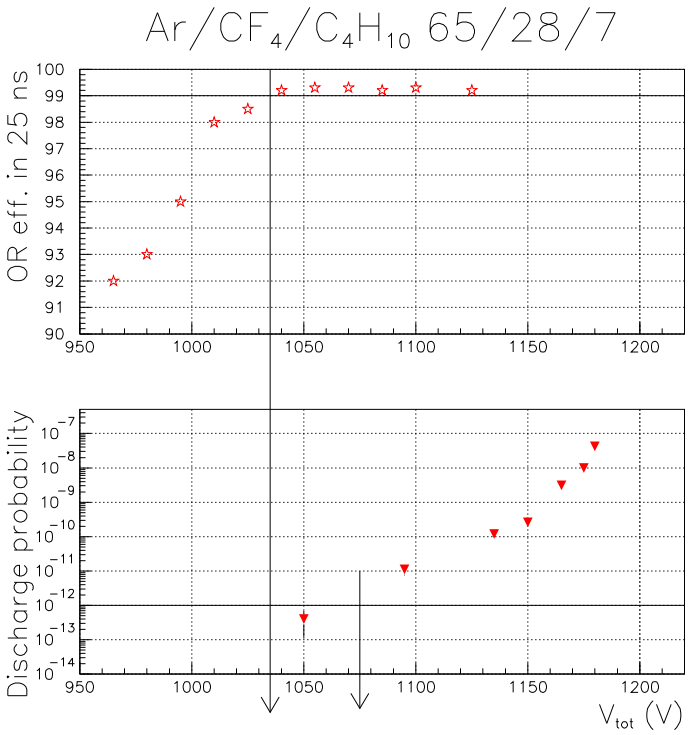

Figure 5.7: Discharge probability per incident particle as a function of V_{tot} for the $Ar/CF_4/C_4H_{10}$ (65/28/7) gas mixture.

The time response in the chamber is constant within the experimental uncertainties and no effects on the pads at the edge of the active area are observed.

5.6 Conclusions

Having anylized the results on the measuremts performed on the large chambers, we may conclude that:

- *$Ar/CO_2/CF_4$ (60/20/20).*
  The detector shows a very good ageing behavior and rate capability, a discharge probability lower than 10^{-12} and a cluster size lower than 1.16 up to gain of the order of $2 \cdot 10^4$. The same gain value is needed to ensure a detector efficiency in a 25 ns window of 99 %.

  We conclude that we cannot use the GEM detector filled with this gas mixture for equipping M1R1 and M1R2.

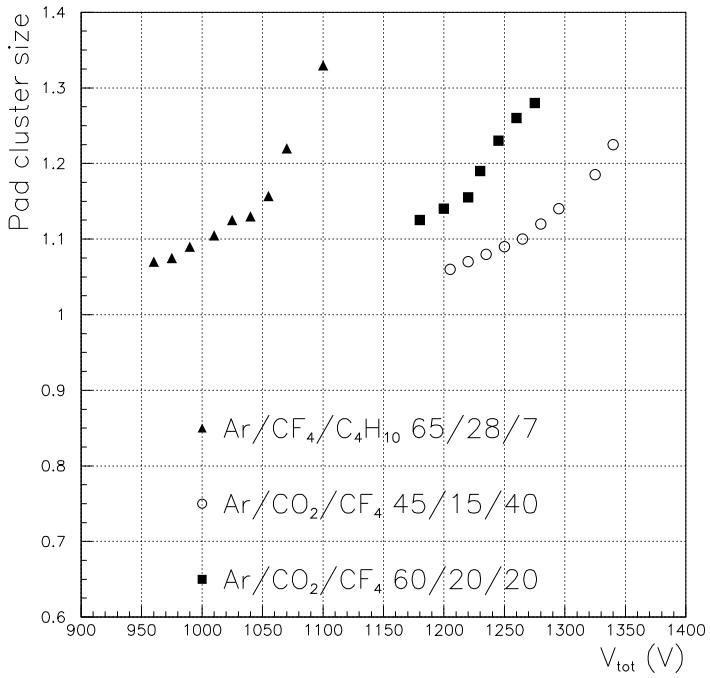

Figure 5.8: Detector pad-cluster size as a function of V_{tot}.

- *$Ar/CF_4/C_4H_{10}$ (65/28/7).*
  This gas mixture provides very interesting results both for the time performance (99.0 % of ϵ_{25} of two OR-ed chambers for a gain of $8 \cdot 10^3$) and for the discharge probability (less than 10^{-12} up to a gain of $2 \cdot 10^4$). Unfortunately, the pad-cluster size results quite high (1.21 at the end of the working region). d This can be due to the high diffusion coefficient of the isobutane. Anyway, the main problem of this kind of gas mixture can be the ageing effect. More detailed studies on this item are now

Gas Mixture	Pad-cluster size
$Ar/CO_2/CF_4$ (60/20/20)	1.16 ± 0.01
$Ar/CO_2/CF_4$ (45/15/40)	1.17 ± 0.01
$Ar/CF_4/C_4H_{10}$ (65/28/7)	1.21 ± 0.01

Table 5.1: Detector pad-cluster size for a V_{tot} giving a discharge probability of 10^{-12}.

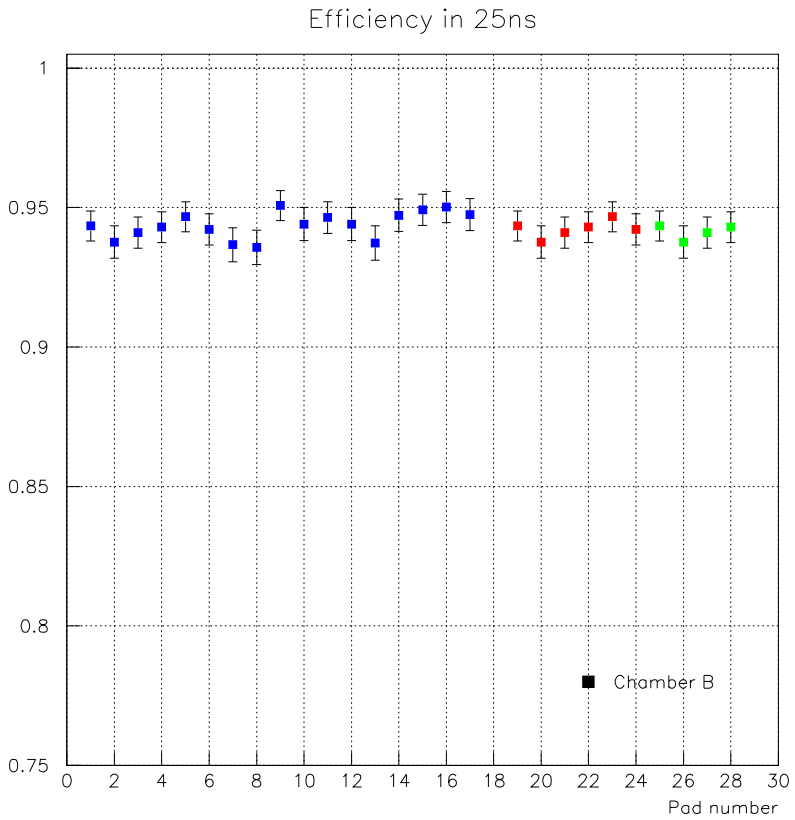

Figure 5.9: Study of the homogeneity of the efficiency in a 25 ns window as a function of the pad position.

under way.

- *$Ar/CO_2/CF_4$ (45/15/40).*
  The efficiency in a 25 ns window of two OR-ed chambers is larger than 99 % for a gain of $3 \cdot 10^3$ and the discharge probability results within the safe limit of 10^{-12} up to a gain of 10^4. For this gain value the pad-cluster size is 1.17 and then below the limit of 1.20. The ageing and rate capability studies perfomed with an $Ar/CO_2/CF_4$ based mixture did not show any deterioration of the detector performance.

Therefore, we can conclude that the triple-GEM based detector, operated with an $Ar/CO_2/CF_4$ (45/15/40) mixture, fulfills all the requirements for equipping the two central regions of the first muon station of LHCb.

Conclusions

During my PhD thesis, I worked on the development of a charged particle detector based on GEM technology proposed for equipping the inner part of the first muon station of the LHCb experiment.

Muons provide very useful information on $pp \rightarrow b\bar{b}$ events. A high transverse-momentum (p_t) muon can indicate the heavy flavour contents of the initial state. Moreover, muons from semileptonic b decays can also be used to tag the initial flavour in the b-hadrons parent.

The muon system will provide a fast measure of the muon p_t which will be used by the level-0 trigger to select interesting events. The effective LHCb level-0 trigger input-rate will be of about 10 MHz and with a latency of 4.0 μs this rate has to be reduced to 1 MHz. 10 %$\div$20 % of the output rate will be allocated to the muon trigger.

Five detector stations will operate in the system: four downstream the calorimeters (M2-M5) and one (M1) upstream. Due to the long lever arm between M1 and M2 and to the high space resolution of M1 not spoiled by the multiple scattering, the information coming from the first muon station will be crucial to provide a resolution of the order of 20 % in the muon p_t measurement. On the other hand, in the central region of M1 the particle rate will be as high as 500 kHz/cm^2.

Therefore, for equipping the inner part of M1 a detector should provide:

- An efficiency in a 25 ns window higher than 95 %, in order to ensure for the station made by two detector-layers logically OR-ed an efficiency higher than 99 % in the bunch crossing identification;
- A pad-cluster size less than 1.2 for 1 $\times$ 2.5 cm^2 pads. This requirement is crucial to achieve good resolution in the p_t measurement;
- A rate capability and a radiation hardness allowing a safe detector operation for ten years;

The Multi-Wire Proportional Chamber technology chosen for the rest of the muon system can hardly provide the rate capability needed for the inner

regions of M1 and they exhibit a poor space resolution. Moreover they would show ageing problems.

During the previous months, special detector prototypes based on the MWPC technology (Asymmetric MWPC and Double Cathode Read-out MWPC) were built and tested. They are designed to operate with a lower gain reducing the rate and ageing problem. They showed a very good rate capability (up to 500 kHz/cm^2), but they have a high pad-cluster size (1.3÷1.4) and it results impossible to perform adequate ageing tests in a reasonable time period.

At the "Università degli Studi di Cagliari", in collaboration with a group of the "Laboratori Nazionali di Frascati", we developed a detector based on GEM-technology. A complete and detailed simulation allowing us to understand the microscopic processes arising inside the detector was carried out. The simulation resulted to be a usefull tool for the study of the gas mixture properties and of the detector electron-transparency. An analytical model describying the GEM behavior was performed. It led, for the first time, after a detailed comparison with experimental data, to an indirect measurement of all the GEM behavior parameters.

The acquired knowledge resulted useful in the work of optimization of the detector.

1. The search for a satisfactory geometry and the study of several different gas mixtures allowed to achieve good time performance: the time distribution RMS was measured to be 4.5 ns, while the chambers ensure an efficiency of 98 % in a 25 ns time window. These result proved to be a remarkable improvement over every other published measurement.

   An RMS values of 4.5 ns represents the best time performance of a triple-GEM chamber used for minimum ionizing particle detection.

2. The intrinsic space resolution of the detector has resulted in a low average number of fired pads per track. The pad-cluster size was measured to be less than 1.2 in a large interval of the explored voltage range for 1×2.5 cm^2 pads.

3. Detailed studies showing the positive effect of the charge spreading due to diffusion in the gas were performed. Optimizing the gap geometry allowed to exploit this effect and to achieve a reduction of the discharge probability by more than one order of magnitude.

4. We studied the chamber rate capability and we found a good stability up to a photon rate of $5 \cdot 10^7$ Hz/cm^2. The ageing effect was also measured as a function of the total integrated charge on the detector

pads; it was found to be less than 5 % up to a total charge of about 20 C/cm^2 while, after ten years of operation, the chambers are expected to integrate 13 C/cm^2.

After 3 years of study and development, we made noteworthy improvements in the triple-GEM detector comprehension and in its performance. Today, it results the only technology fulfilling the experiment requirements, and it is the best candidate to equip M1R1 and M1R2.

Bibliography

[1] J.H. Christenson et al., Phys. Rev. Lett. **13**, 138 (1964).

[2] R. Fleischer, hep-ph/9809216.

[3] A.J. Buras, hep-ph/9905437.

[4] N. Cabibbo, Phys. Rev. Lett. **10**, 531 (1963).

[5] M. Kobayashi and T. Maskawa, Prog. Th. Phys. **49**, 652 (1973).

[6] L. Wolfenstein, Phys. Rev. Lett. **51**, 1945 (1983).

[7] R. Aleksan et al., Phys. Rev. Lett. **73**, 18 (1994).

[8] H. Albrecht *et al.* "Observation of $B^0 - \bar{B}^0$ Mixing," Phys. Lett. B **192** (1987) 245.

[9] Q. Ho-Kim and Xuan-Yem Pham, "Elementary particles and their interactions" Springer Editor.

[10] D. E. Groom *et al.* "Review Of Particle Physics," Eur. Phys. J. C **15** (2000) 1.

[11] For a recent analysis, see for example P. Paganini et al., DELPHI-97-137 and LAL-97-79.

[12] B. Aubert *et al.*, hep-ex/0203077.

[13] K. Abe *et al.*, hep-ex/0207022.

[14] C. A. Blocker "Measurement of sin(2beta) from J/psi K(S) decays,"

[15] For a recent review, see A.J Buras and R. Fleischer, TUM-HEP-275/97 (1997).

[16] R. Fleischer, 7th Int. Symp. on Heavy Flavour Physics, Santa Barbara, CERN-TH-97-241 (1997).

[17] L. Wolfenstein and Y.L. Wu, Phys. Rev. Lett. **73** (1994) 2809.

[18] P. Cho, M. Misiak and D. Wyler, Phys. Rev. **D54** 3329 (1996).

[19] Lhcb collaboration, "A large hadron collider beauty experiment for precision measurements of CP violation and rare decays" CERN/LHCC 004 (1998).

[20] LHCb collaboration, "LHCb velo Technical Design Report" CERN/LHCC 011 (2001)

[21] LHCb collaboration, "LHCb outer tracker Technical Design Report" CERN/LHCC 024 (2001)

[22] LHCb collaboration, "LHCb RICH Technical Design Report" CERN/LHCC 037 (2000)

[23] LHCb collaboration, "LHCb calorimeters Technical Design Report" CERN/LHCC 036 (2000)

[24] LHCb collaboration, "LHCb muon system Technical Design Report" CERN/LHCC 010 (2001)

[25] T. Sjostrand, "High-energy physics event generation with Pythia 5.7 and Jetset 7.4", Comput. Phys. Commun. 82 (1994) 74.

[26] "GEANT Detetctor description ans simulation tool", CERN Program Library Long Writeup W5013 (1994).

[27] C. Zeitnitz and T. A. Gabriel, "The Geant-Calor interface user's guide" (1999).

[28] J.H. Lopes, "Simulation of chamber inefficiency and noise in the LHCb muon system and study of its effect on the L0 muon trigger performance", LHCb 2001–060 Muon.

[29] F. Sauli, Nucl. Instrum. Meth **A409**, 101 (1998).

[30] F. Sauli, Nucl. Instrum. Meth. **A386**, 531 (1997).

[31] Maxwell 3D Field Simulator. User's Reference. Ansoft Corporation.

[32] R. Veenhof, "Garfield, a drift chamber simulation program" Version 7.04, Nucl. Instrum. Meth. **A419**, 726, (1998).

[33] J. Benlloch et al., Nucl. Instrum. Meth. **A419**, 410 (1998).

[34] Spice, MicroSim DesignLab Version 7.1.

[35] S. Biagi, Magboltz, program to simulate electrons and ions drift in gas mixture, Version 2.0, CERN.

[36] I. Smirnov, HEED, program to compute energy loss of fast particle in a gas, Version 1.01, CERN.

[37] S. Biagi, Nucl. Instrum. Meth. **A273**, (1998).

[38] U. Beker et al. Gas R&D Home Page (http://cyclotron.mit.edu/drift).

[39] G. Bencivenni et al., "Experimental characterization of a GEM-based detector" proceeding of the 6^{th} Position Sensitive Detector Conference, Leichester (UK), 2002.

[40] F. Sauli, "Principles of operation of multiwire proportional and drift chamber" CERN 77-09, 1977.

[41] S. Ramo, "Currents induced in electron motion ", Proc. IRE 27, 584 (1939).

[42] G. Bencivenni et al., "A triple GEM detector with pad readout for inner region of the first LHCb muon station", LHCb 2001-051.

[43] S. Bachmann et al., "Performance of GEM detectors in high intensity particle beams," CERN-EP/2000-116, 31 August 2000.

[44] H. Raether,"Electron avalanche and breakdown in gases", Butterworths, Washington, 1964.

[45] T. Zeuner, Nucl. Instrum. Meth. **A446**, 324 (2000)

[46] A. Bressan et al., "Beam tests of the gas electron multiplier," Nucl. Instrum. Meth. **A425**, 262 (1999).

[47] S. Bachmann et al., "Performance of GEM detectors in high intensity particle beams," CERN-EP/2000-151, 11 December 2000.

[48] H. R. Schmidt et al, ALICE note 1999-56.

[49] S. Bachmann et al., Nucl. Instrum. Meth. **A438**, 376 (1999).

[50] C.Richter et al., Nucl. Instrum. Meth. **A461**, 38 (2001).

[51] A. Gandi, Laboratory of Photomechanical Techniques and Printed Circuits, EST-SM-CI Section, CERN, Geneva, Switzerland.

[52] A. Vorobyov et al, LHCb note 2000-003.

[53] G. Deptuch *et al.*, "Design and testing of monolithic active pixel sensors for charged particle tracking," IEEE Trans. Nucl. Sci. **49** (2002) 601.

[54] L. Malter, Phys. Rev. 50, 48 (1936).

[55] W. S. Bawdeker, IEEE Trans. Nucl. Sci. NS-22, 282 (1975)

[56] G. Carboni, FPCP Conference, Philadelphia (2002).